VISION-BASED BUILDING ENERGY DIAGNOSTICS AND RETROFIT ANALYSIS USING 3D THERMOGRAPHY AND BUILDING INFORMATION MODELING

BY

YOUNGJIB HAM

DISSERTATION

Submitted in partial fulfillment of the requirements
for the degree of Doctor of Philosophy in Civil Engineering
in the Graduate College of the
University of Illinois at Urbana-Champaign, 2015

Urbana, Illinois

Doctoral Committee:

Assistant Professor Mani Golparvar-Fard, Chair
Professor Khaled El-Rayes
Associate Professor Liang Y. Liu
Assistant Professor Nora El-Gohary
Professor Lucio Soibelman, University of Southern California

ABSTRACT

The emerging energy crisis in the building sector and the legislative measures on improving energy efficiency are steering the construction industry towards adopting new energy efficient design concepts and construction methods that decrease the overall energy loads. However, the problems of energy efficiency are not only limited to the design and construction of new buildings. Today, a significant amount of input energy in existing buildings is still being wasted during the operational phase. One primary source of the energy waste is attributed to unnecessary heat flows through building envelopes during hot and cold seasons. This inefficiency increases the operational frequency of heating and cooling systems to keep the desired thermal comfort of building occupants, and ultimately results in excessive energy use. Improving thermal performance of building envelopes can reduce the energy consumption required for space conditioning and in turn provide building occupants with an optimal thermal comfort at a lower energy cost. In this sense, energy diagnostics and retrofit analysis for existing building envelopes are key enablers for improving energy efficiency. Since proper retrofit decisions of existing buildings directly translate into energy cost saving in the future, building practitioners are increasingly interested in methods for reliable identification of potential performance problems so that they can take timely corrective actions. However, sensing what and where energy problems are emerging or are likely to emerge and then analyzing how the problems influence the energy consumption are not trivial tasks.

The overarching goal of this dissertation focuses on understanding the gaps in knowledge in methods for building energy diagnostics and retrofit analysis, and filling these gaps by devising a new method for multi-modal visual sensing and analytics using thermography and Building Information Modeling (BIM). First, to address the challenges in scaling and localization issues of 2D thermal image-based inspection, a new computer vision-based method is presented for automated 3D spatio-thermal modeling of building environments from images and localizing the thermal images into the 3D reconstructed scenes, which helps better characterize the as-is condition of existing buildings in 3D. By using these models, auditors can conduct virtual walk-through in buildings and explore the as-is condition of building geometry and the associated thermal conditions in 3D. Second, to address the challenges in qualitative and subjective interpretation of visual data, a new model-based method is presented to convert the 3D thermal profiles of building environments into their associated energy performance metrics. More

specifically, the Energy Performance Augmented Reality (EPAR) models are formed which integrate the actual 3D spatio-thermal models (‘as-is’) with energy performance benchmarks (‘as-designed’) in 3D. In the EPAR models, the presence and location of potential energy problems in building environments are inferred based on performance deviations. The as-is thermal resistances of the building assemblies are also calculated at the level of mesh vertex in 3D. Then, based on the historical weather data reflecting energy load for space conditioning, the amount of heat transfer that can be saved by improving the as-is thermal resistances of the defective areas to the recommended level is calculated, and the equivalent energy cost for this saving is estimated. The outcome provides building practitioners with unique information that can facilitate energy efficient retrofit decision-makings. This is a major departure from offhand calculations that are based on historical cost data of industry best practices. Finally, to improve the reliability of BIM-based energy performance modeling and analysis for existing buildings, a new model-based automated method is presented to map actual thermal resistance measurements at the level of 3D vertexes to the associated BIM elements and update their corresponding thermal properties in the gbXML schema. By reflecting the as-is building condition in the BIM-based energy modeling process, this method bridges over the gap between the architectural information in the as-designed BIM and the as-is building condition for accurate energy performance analysis.

The performance of each method was validated on ten case studies from interiors and exteriors of existing residential and instructional buildings in IL and VA. The extensive experimental results show the promise of the proposed methods in addressing the fundamental challenges of *(1) visual sensing*: scaling 2D visual assessments to real-world building environments and localizing energy problems; *(2) analytics*: subjective and qualitative assessments; and *(3) BIM-based building energy analysis*: a lack of procedures for reflecting the as-is building condition in the energy modeling process. Beyond the technical contributions, the domain expert surveys conducted in this dissertation show that the proposed methods have potential to improve the quality of thermographic inspection processes and complement the current building energy analysis tools.

ACKNOWLEDGEMENT

First of all, I would like to express my special thanks to my wife, Doori, over the past four years. Without her sacrifice and encouragement, I could not have carried out anything during my PhD. Also, thanks my two beautiful princesses, Harin and Hara, for inspiring to me. No words can express my endless gratitude to my family in the U.S. and Korea.

I would like to give special thanks to my advisor, Dr. Mani Golparvar-Fard, as well. I believe I am extremely lucky in that I was able to work with him for my PhD. With his sincere support and confidence in me, I was able to finish my PhD. I hope to follow in his footstep as my role model in academia. Also, I would like to give a big shout-out to my wonderful PhD committees, Dr. Khaled El-Rayes, Dr. Liang Liu, Dr. Nora El-Gohary, and Dr. Lucio Soibelman at the University of Southern California for all their supports. Their insight and constructive feedback were greatly helpful to improve the quality of my work. Also, I would like to give thanks to Virginia Tech for the support in the first phase of my research. I would like to express my thanks to Dr. SangHyun Lee at the University of Michigan as my mentor. His sincere advices on both research and life always inspired me with enthusiasm whenever I met him at any conferences. Also, I would like to give my thanks to Dr. Hyun-Soo Lee and Dr. Moonseo Park at Seoul National University. As my former academic advisors in Korea, I was able to learn a lot about the fundamental of research in my domain. And thanks everyone at Champaign and Blacksburg for the cheerful coffee, beer, and advice along the way. Working and hanging out with these amazing people over the past four years was one of the best time I've ever experienced.

Finally, I would like to thank building energy specialists in the Smart Energy Design Assistance Center (SEDAC) for their participation in user studies, FLIR for their support with providing a thermal camera for initial experiments, and the National Center for Supercomputing Applications (NCSA)’s Institute for Advanced Computing Applications and Technologies Fellows program for their financial supports.

TABLE OF CONTENTS

LIST OF FIGURES

LIST OF TABLES

CHAPTER 1. INTRODUCTION

1.1 Overview

The building sector is an increasingly important area for improving energy efficiency as it accounts for approximately 24% of global energy consumptions and up to 41% in developed countries (U.S. DOE 2010). Currently, about 75% of all electricity and 54% of all natural gas produced in the U.S. are consumed in the building sector (U.S. DOE 2010). According to a forecast on energy consumptions by the U.S. Energy Information Administration (EIA) (EIA 2010), between 2010 and 2030, the increase in the energy consumption of the building sector (2098 billion kWh) is anticipated to be much more than those of the industrial and transportation sectors (1187 and 984 billion kWh respectively). This increase in energy use has potential to have significant destructive impacts on the environment as the majority of the energy is primarily produced from burning fossil fuels (e.g., coal, petroleum, and gas). This in turn makes the building sector the largest emitter of Green House Gases (GHG) and the single primary contributor to anthropogenic climate change (Architecture2030 2011). In order to reduce the excessive energy consumption of the building sector and minimize their environmental impacts, much attentions have been paid to increasing energy efficiency of the building sector. For example, to lower the energy use required for space conditioning, building practitioners are embracing the new concept of energy-efficient building design (e.g., net-zero passive house) in which government agencies are proposing the associated incentive-based guidelines (e.g., 2011 Better Buildings Initiative). In addition, for the construction phase, the use of building materials with higher thermal resistance is recommended for better insulations. Currently, several energy efficiency programs such as LEED and ENERGY STAR are also becoming prevalent in residential and commercial buildings in the U.S. As a result of such mandatory and voluntary programs, larger numbers of new buildings are being rigorously designed and constructed to meet the requirement of current rigorous energy codes and strive to increase their energy efficiency.

Nonetheless, the problem of building energy efficiency is not only limited to how new buildings are designed and constructed energy-efficiently. Looking at building's life-cycle energy consumption, up to 84% of the total energy consumption is associated with the operation phase (U.S. DOE 2010), and more importantly most existing buildings do not meet current rigorous energy standards. For example, heat loss through building envelopes such as ceiling and walls

could be very large if insulation levels are less than the recommended level, which makes building occupants uncomfortable and power use inefficient. When a buildings was built, the builder likely installed the amount of insulation recommended at that time. Given today's energy prices and regulation, the level of insulation is more likely to be inadequate, especially if the building is old. Currently, 87% of overall residential buildings and 74% of total commercial buildings in the U.S. were built before the year 2000 when the current rigorous energy regulations were not established (U.S. DOE 2010). More importantly, as the age of existing buildings is rising, they continuously undergo degradation over the remainder of their service life. According to a report by the U.S. Department of Energy (U.S. DOE 2010), around 35% of the input energy in existing buildings is still being wasted.

Under these conditions, retrofitting existing buildings is imperative to minimize the cost associated with unnecessary energy consumptions in the building sector. To meet new rigorous energy standards, it is anticipated that around 150 billion S.F. − roughly half of the entire building stock in the U.S. − will require retrofit over the next 30 years (Gould and Hosey 2006). Today, the governments in the U.S. and around the world are imposing new requirements for retrofits on the building sector. Their requirements are typically accompanied with technical and financial assistances in form of rebates and incentives. For example, in California, estimated 85% of these programs has targeted energy efficiency retrofit investments in existing buildings (California Energy Commission 2012). Similarly, in Massachusetts, through initiatives sponsored by utility companies, homeowners can be exempt from local property tax for a period of 20 years by improving the energy efficiency of their existing buildings (Mass Saves 2013). The substantial financial benefits of these programs are increasingly encouraging practitioners to improve the energy efficiency of their buildings. As any retrofit decision directly translates into energy cost saving in the future, practitioners are increasingly interested in identifying building performance problems so that they can take timely corrective actions.

Understanding the energy profile of existing buildings is the first step towards identifying areas for improvement. Despite the high energy efficiency of modern HVAC systems, today majority of building energy is still being consumed for space conditioning purposes. Heating and cooling account for 48.8% and 24.8% respectively of the total energy usage in residential and commercial buildings (U.S. DOE 2010). Close examinations by (U.S. DOE 2012) reveal that there is an excessive energy consumption for space conditioning, which is primarily attributed to the

unnecessary heat flow through building enclosures during hot and cold seasons. These thermal performance problems in buildings are likely to increase the operation frequency of heating and cooling systems to keep the desired thermal comfort of building occupants, and ultimately results in excessive energy use. Homeowners are typically unaware of these inefficiencies, and thus to improve their thermal comfort, they typically adjust the set point of heating and cooling systems, which increases the energy consumption for space conditioning. Surprisingly, to save money on utility bills associated with space conditioning, some occupants undesirably set the room temperature lower than the average in winter and higher in summer. While such actions reduce the excessive heat flow through building enclosures, it naturally has adverse impacts on the thermal comfort of the building occupants. Rather than changing the set point of heating and cooling systems undesirably, identifying and minimizing the source of excessive heat flows through building envelopes is a key to improving energy efficiency of existing buildings.

Figure 1.1 Examples of Thermal and Digital Images Captured from Existing Buildings

One of the interesting developments and rather contemporary practices for inspecting the as-is building condition is to leverage an infrared thermography (Balaras and Argiriou 2002; Cerdeira et al. 2011; Fox et al. 2014; Kylili et al. 2014; Martín Ocaña et al. 2004; Molin et al. 2011). The IR thermography – which detects and measures heat variations emitted by building surfaces under inspection and transforms them into 2D imagery where each radiation energy level is represented by a color gradient – is particularly known as a great tool for identifying defects associated with building energy performance in a non-destructive manner.

Figure 1.1 shows examples of digital and thermal images captured from existing buildings. The right column represents the thermal characteristics of the same areas captured in the digital images (left column). The images in each row were captured simultaneously by using a thermal camera which has a built-in digital camera. The spatial resolution and field-of-view of thermal images are considerably lower than their digital counterparts when using a consumer-level thermal camera that is widely used for building diagnostic purposes today (in range of $3-5k). Compared to spot radiometers which measure thermal radiation one spot at a time or thermal line scanners that show radiant temperature values along a line, a thermal camera can capture the wide distribution of surface temperatures at a high level of detail (U.S. DOE 2012). In addition, in contrast to contact thermometers, thermography provides non-contact and continuous measurements. Over the past few years, thermographic inspection has become prevalent as a robust tool in detecting, analyzing, and reporting the as-is energy performance of existing buildings (U.S. DOE 2012). Several studies including (Balaras and Argiriou 2002; Cerdeira et al. 2011; Cho et al. 2015; Fox et al. 2014; Kylili et al. 2014) have demonstrated the benefits of thermography to facilitate the current building energy diagnostic practices and ultimately support improvements in building energy efficiency. Thermal distributions captured from building surfaces are directly influenced by abnormal heat transfer caused by defects such as faulty construction or deteriorations. Thus, infrared thermography as a reality capturing method allows such thermal defects to be detected both from inside and outside of buildings. In particular, analyzing building thermography helps locate (1) heating and cooling losses due to typical structural problems such as missing insulation, degradation of existing insulation, and air leakages; (2) moisture issues in building envelopes; and (3) performance problems of building systems such as degradation of floor heating or HVAC systems. The abnormal temperature variations caused by heat, air flow, and moisture can adversely affect the durability of construction materials and ultimately lead to lower energy

efficiency levels. Considering that a primary source of building energy inefficiency is typically relevant to excess energy consumptions for space heating and cooling purposes that are affected by heat transfer problems (U.S. DOE 2010), sensing and analyzing such abnormal thermal performance have significant potential to improve building energy efficiency.

Currently, another dominant method for understanding building energy performance and assessing different energy efficiency retrofit alternatives is to use building energy performance modeling and simulation software (e.g., EnergyPlus, Ecotect, and eQuest). These tools are typically used to evaluate thermal impacts of different retrofit alternatives on building performance improvements and their associated energy cost savings. Energy modeling using such software is essentially an empirical exercise that relies on good observations to capture the as-is condition of existing buildings. Current analysis tools have two parts: 1) a graphical user interface; and 2) a simulation engine for thermal calculations. The simulation engine requires users to directly input the description of a given building such as geometry (e.g., thermal zone layout and construction), local weather data, HVAC systems, operating schedules, space loads (e.g., lighting, appliances, and occupancy), and utility rates. This information is typically obtained from specifications, drawings, photos, or any other data that might be available. For example, building geometrical information is collected from traditional field surveying techniques such as a tape measurement, Total Stations, terrestrial laser scanning, or from 2D CAD models. Currently, 2D images are sometimes used to manually extract geometrical information from existing buildings (e.g., OpenStudio SketchUp). The input files containing the required modeling parameters are then fed into a simulation engine to calculate building thermal loads and their associated energy consumption. Here, leveraging pre-existing data such as building geometry, construction types, and thermal properties in Building Information Models (BIM) has significant potential to streamline several steps in the traditional energy modeling process. With BIM models, energy modelers can minimize the time and effort needed to construct energy models. Moreover, the results of the energy analyses would be more consistent across different modelers. Such benefits have motivated many owners including U.S. General Services Administration (GSA) to explore the use of BIM in building energy performance modeling practices (U.S. General Services Administration 2012). In this sense, to strengthen the reliability and consistency of building energy performance simulation results, BIM-based energy modeling is gaining the popularity to predict heating and cooling loads, and derive information on energy consumptions, utility costs, indoor

environmental conditions, and daylighting analysis (U.S. General Services Administration 2012).

Despite the effectiveness, anecdotal evidence and controlled studies on analyzing the actual energy performance of existing buildings have raised concerns about the accuracy of the current energy performance modeling and simulation tools. Due to many assumptions and simplifications that are typically made during the modeling process, predictions obtained from the simulation tools typically deviate from the actual measurements (Azar and Menassa 2012; Turner and Frankel 2008; Yudelson 2010). Hence, energy models for existing buildings need to be manually calibrated to represent the actual energy performance, which is likely to delay the retrofit process due to the late delivery of information necessary to guide the associated retrofit decision-making process (AIA 2012; Autodesk 2011). Any deviations between actual measurements and simulated results of building energy performance can be attributed to the following:

(1) The difficulty in modeling occupancy patterns: The challenges associated with modeling dynamic patterns of building occupancy may result in misrepresentation of actual energy consumption during the operational phase of a building. For example, for building operating schedules, current energy simulation tools typically require averaging occupant schedules for a floor rather than assigning an individual schedule for each building space. Several recent studies including (Azar and Menassa 2012) have focused their efforts on modeling the time-variant characteristics of the energy use of building occupants and studied their impact on the results of building energy analysis.

(2) Building performance problems (Kunz et al. 2009; Maile 2010): Difficulty in accurate modeling of actual thermal properties of building assemblies is another key reason behind deviations between actual and expected energy performances. Once buildings are operating, the simulation tools often do not accurately represent the as-is building energy performances. This is due to the difficulty in the selection of accurate modeling inputs and subjective calibrations of energy models (Azar and Menassa 2012; Maile 2010; Tupper 2011; Tupper et al. 2011). This is primarily for two reasons: first, typically the as-is building conditions are not quantitatively documented at the energy analysis stage of existing buildings, hence all material conditions and compositions of building elements are considered to be consistent across their geometrical forms in a qualitative manner during modeling process (e.g., selecting among ‘high’, ‘average’, or ‘low’ performance); and second, the current tools typically are incapable of modeling thermal condition non-uniformity across geometrical forms of building elements. This is mainly because the tools

are based on the static representation of building conditions (e.g., a single thermal property for each building element), which cannot accurately model large areas of building envelopes that contain significant thermal resistance non-uniformity. Thus, the simulation results from current energy analysis tools do not reflect the as-is building condition including small-scale energy problems (caused by construction defects or non-uniform deteriorations) which are typically prevalent in real-world building environments − which is likely to increase the energy usage for space conditioning to recover the unnecessary heat flow through defective building enclosures during hot and cold seasons.

1.2 Problem Statements

During building energy diagnostic processes, thermography is widely used as a great tool to effectively illustrate the as-is building condition to practitioners. In addition, pre-existing BIM models can provide easy and rich access to building information, allowing energy modelers to minimize their time and efforts needed to construct energy models for analyzing the energy performance of existing buildings and study the impact of different retrofit alternatives on energy consumptions. Despite their benefits, according to surveys with domain experts with 2 to 10 years of practical experiences in energy auditing of existing buildings, current practices have the following challenges:

(1) The current practices on thermographic inspection primarily focus on the direct application of raw 2D thermal imagery, which makes the process of data analyses time-consuming and labor-intensive. Comparing to consumer-level digital cameras (>1 megapixel), thermal cameras typically support low spatial resolutions (160×120 or 320×240 pixel) with small field-of-view due to inherent technical limitation of thermal camera lens. Thus, building areas which can be represented in a single thermal image are significantly smaller than their digital counterparts. Consequently, sensing and analyzing thermal performance of building environments requires large amount of visual data to be collected and explored after data collection. Not only large numbers of thermal images need to be analyzed, but also they are typically unordered and not geo-tagged. Hence, it is difficult in the post-processing stage to figure out ‘where specific thermal image associated with energy problems was actually captured from’ or ‘what building elements they are representing’. Nowadays, energy auditors provide the associated building information by using paper-based inspection reports (Figure 1.2). However, preparing and looking at these reports, for

each thermal image, would be time-consuming and labor-intensive.

Figure 1.2 Examples of Standard Reports for Building Thermographic Inspection

A few thermal cameras support the options for integrating a pair of digital and thermal images (i.e., picture-in-picture overlay) or voice recording to collect the location information of building elements that specific thermal images represent. However, given significant amount of visual data, examining large numbers of overlaid 2D images or significant amount of recorded voices during a post-processing stage would be time-consuming. The lack of a method that address scaling and localization issue of 2D image-based inspection is one of the major bottlenecks for rapid analyses on the energy performance problems to support retrofit decision-makings. Some subjects in the surveys noted that "Sometimes it is hard to tell where the thermal image is coming from in the building. Often, our audits last about 2-4 hours. In this time, it is hard to note which image was taken where within the building.", "Audits can take a long time, up to several hours for large residential houses. IR imaging is done piece-wise through a building. It takes detailed documentation to know where each image was taken and what it is supposed to be showing. This can be confusing, and is often detrimental to the client's understanding, even with a good service provider explaining discoveries."

(2) The current practices for analyzing the visual data obtained from thermographic inspections are manual, and energy auditors primarily conduct visual inspections in a qualitative

manner (Fokaides and Kalogirou 2011; Lagüela et al. 2011). All subjects responded that today thermography is primarily used for qualitative documentations in support of leveraging the Home Energy Rating System (HERS) for reporting purposes at a later stage. Most responders used the word *"qualitative"* to describe the current process. To be more specific, auditors primarily interpret the captured thermal images based on surface temperature to visually detect abnormal thermal regions (e.g., hot or cold spots). Without converting temperature data from building surfaces into energy performance metrics that can represent the quantitative impacts on energy consumption, the surface temperatures alone do not explicitly explain energy performance problems. Comparing actual energy performance metrics with the associated benchmark is capable of supporting a reliable identification of potential energy problems, which is an important first step in improving energy efficiency of existing buildings. However, due to a lack of proper benchmarks for the as-is thermal performance and the associated energy performance metrics, current qualitative interpretations of building thermography can be error-prone and often inconsistent, which is directly affected by knowledge and experiences of different energy auditors. Considering a limited number of professional energy auditors, this process would adversely impact the quality of the inspection during building energy audit processes, which restricts the high-quality energy audit to only high-budget projects.

More importantly, to better support retrofit decision-makings – beyond identifying performance problems – there is a need for a method that can provide a reliable analysis of the expected energy cost savings associated with retrofit alternatives. However, the current thermographic inspections for building diagnostics lack a consideration about the associated energy cost analysis. Currently, after visual inspection by using a thermal camera, recommendations are typically made by offhand calculations based on the historical cost data of industry best practices and the potential savings from different upgrade measures. In fact, homeowners are mostly motivated by how much money can be saved if the detected performance problems are retrofitted. Based on qualitative interpretation of thermal defects without analyses in terms of their monetary impacts on building energy consumptions, homeowners may be reluctant to spend their money for retrofits due to the high degree of uncertainty in the value of their investment. Recent surveys aimed at commercial real estate executives (Menassa 2011; Turner Construction 2008) confirmed that a lack of tools for accurate quantification of the monetary benefits from building retrofits is one of the main sources in discouraging homeowners from

considering building energy efficiency retrofits. The hypothesis in this research is that if the monetary benefits from retrofitting thermal performance problems are reliably quantified, homeowners are more likely to do better decision-makings for building retrofits.

(3) The current BIM-based energy performance modeling and analysis leverage the notional thermal properties of building elements stored in industry standard databases available in BIM-authoring tools (e.g., ASHRAE data) for operating energy simulation engines for thermal load calculations. In current simulation engines, it is assumed that each building element has a constant surface-wide thermal property across geometrical forms. This approach would be robust for newly constructed buildings, but not for existing buildings that have been typically degraded during the operational phase. During this stage, building materials are more likely to have irregular characteristics caused by construction defects or partial degradations and deteriorate differently over time and thus cause building elements to exhibit thermal resistances non-uniformity across geometrical forms of building assemblies. Depending on the severity of non-uniform degradation, the actual thermal resistance of building elements is more likely to become lower than the notional values declared in the material specifications or industry standard databases of typical building material properties that are available in the BIM-authoring tools. Hence, purely relying on the as-designed building information derived from BIM models without reflecting the as-is building conditions, BIM-based energy analyses for existing buildings are likely to overestimate their energy performance, deviating from the as-is performance. Thermal conditioning of indoor air is basically related to heat transfer between inside and outside of buildings, which affects the thermal comfort of building occupants and the associated energy consumption for space conditioning. Here, one of significant parameters used in thermal analysis is the overall heat transfer coefficient of building envelopes. Thus, modeling the accurate heat transfer coefficients will both improve the accuracy of thermal analysis and provide meaningful information about overall energy use. The significance of these accuracy and their impact on retrofit decision-making processes have caused GSA to highlight *'accurate modeling of as-built conditions'* as one of the top challenges for BIM-based energy modeling (U.S. General Services Administration 2012). In this sense, the hypothesis in this research is that if actual thermal properties of building elements are reliably measured and associated with the corresponding BIM elements, BIM-based energy modeling and analysis tools will produce more reliable outcomes that describe the as-is building energy performance.

1.3 Dissertation Structure

This dissertation is organized as follows:

- Chapter 1 introduces the overview of building energy analysis using thermography and BIM, and presents the challenges in current practices.
- Chapter 2 reviews the state-of-the-art approaches on sensing and analyzing building energy performance using thermography and BIM, followed by discussions on their limitations.
- Chapter 3 presents the specific objectives and the scope of this dissertation.
- Chapters 4 to 8 propose the underlying methods and algorithms for a new vision-based building energy diagnostics and retrofit analysis using 3D thermography and BIM.
- Chapter 9 presents experimental setup for ten interiors and exteriors of an existing residential building and an instructional facility and discusses the experimental results in detail.
- Chapter 10 wraps up this dissertation with the benefit and future direction of this research.

CHAPTER 2. LITERATURE REVIEW

2.1 Actual 3D Thermal Modeling of Building Environments

The current practices of thermographic inspection for building energy diagnostics are primarily based on analyzing 2D thermal images. To overcome the challenges in small field-of-view and low spatial resolution of 2D thermal imagery, the Field Intelligence Laboratory at MIT (Essess. Inc 2014) is among the first that developed a new imaging system to streamline the process of collecting thermal images from building envelopes. Their method relies on collecting large numbers of overlapping thermal images at night from an array of thermal cameras mounted on a car (Figure 2.1a). Using these images, a high-resolution panoramic thermal image of building façades is generated (Figure 2.1b). The mosaic image is later used to assess the performance of the building envelopes. While this method scales well at the street level, it cannot be used indoors to document thermal performance problems of building envelopes or HVAC systems from inside.

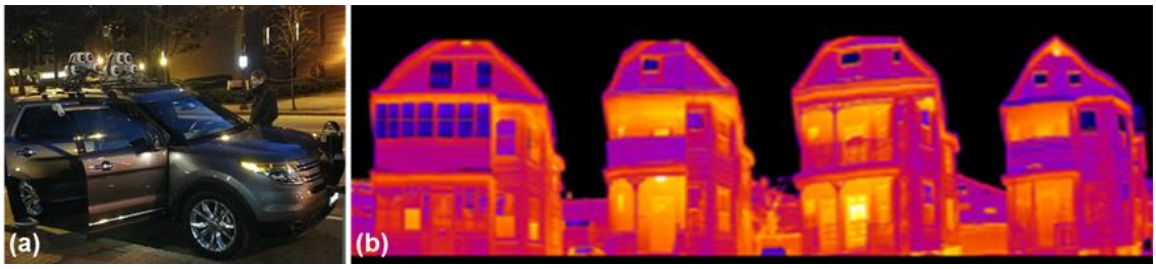

Figure 2.1 (a) Vehicle-mounted Thermal Cameras; (b) an Example of Panoramic Thermal Images for Building Façades

Similarly, the Geo Information Group (TheGeoInformationGroup. 2007) developed a method that identifies the location of heat loss on building roofs using a color-coded thermal-mapping. Infrared Concepts Corporation (InfraredConceptsCorporation 2012) proposed a roof thermal mapping methodology through aerial surveying to gauge repair needs of flat roof structures. Despite their benefits, these methods require manual and sequential texture-mapping of all pairs of thermal and digital images. As a result, their application for building environments would be time-consuming and labor-intensive. Meanwhile, recent thermal cameras provide the picture-in-picture and voice recording functions. Such features enable pairing thermal and digital images captured from the same location, and also manually geo-tagging the images with voice recording. This has created an unprecedented opportunity, and as a result several researchers have

looked into fusing thermal and digital imagery to put thermal images into the building context and obtain more informative scene representations. For example, HomeInspex (HomeInspex 2011) used an overlay image which consists of a pair of thermal and digital images captured from the same scene for reporting building problems. Nonetheless, exploring large numbers of these overlaid 2D images or listening to significant amounts of voice recordings at a later stage can still be time-consuming and labor-intensive. Moreover, in the case of the picture-in-picture function, due to a lack of consideration about radial distortions of thermal imagery and position discrepancies between digital and thermal camera lenses, overlaid 2D images typically show large registration errors (Figure 2.2). The discrepancies between the continuous lines in the digital images and the broken lines in the thermal images highlight false registrations. More importantly, the registration of a pair of 2D digital and thermal images is still not sufficient to provide a whole representation of the as-is condition in a given building space.

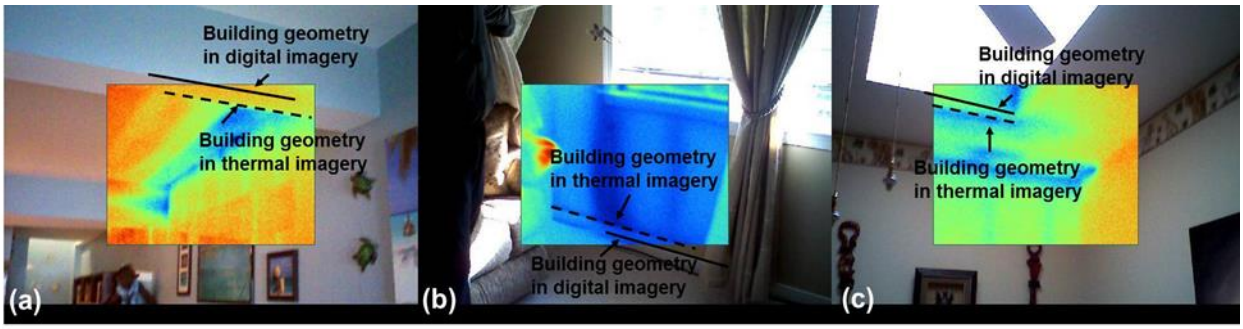

Figure 2.2 Examples of Registration Errors on the Picture-in-Picture Function Available in Recent Thermal Cameras

Over the past few years, several research groups have focused on overcoming the challenges associated with the application of large numbers of unordered and non-geo-registered 2D thermal images. These efforts are primarily focusing on improving the quality of visual sensing by generating 3D thermal models as opposed to conventional 2D image-based representation. 3D building models with the associated thermal values allows practitioners to quickly recognize how temperature values are spatially distributed in a given building space. In the Architecture/Engineering/Construction community, (Wang et al. 2013) have introduced a 3D thermal modeling method for building façades using a Hybrid LIDAR system. They also presented a method for visualizing 3D thermal models of building envelopes on web-based geospatial systems such as Google Earth. The proposed system which consists of a laser scanner and a thermal

camera generates 3D point cloud models for building envelopes with the corresponding temperature values at the point level. The developed method has been extensively tested in both lab settings and façades of a residential building, and promising results are presented. This approach in particular can be useful when a city-level thermal modeling is needed. Similarly, (Lagüela et al. 2011) presented a methodology for registering temperature data with 3D geometrical point clouds generated from a terrestrial laser scanner. This combination was implemented based on control points which were manually selected on both thermography and laser scanning point clouds. (Borrmann et al. 2013) introduced a methodology for 3D thermal modeling of built environments using a robot equipped with a laser scanner and a thermal camera. Their initial experiments were conducted in indoor lab spaces, and no validation results were presented yet on actual confined and complex indoor environments where the movement of a robot can be prohibitively challenged. Although laser scanners can provide useful visual information, it has limited applicability for complex and confined environments, which are typically prevalent in real-world buildings. Moreover, their direct application can suffer from the mixed pixel phenomena for built environments (Golparvar-Fard et al. 2011; Kiziltas et al. 2008). In addition, this in particular requires users to manually remove the associated noise in a post-processing stage. The cost of high precision laser scanners is also still relatively high (~$70-100K). Although their cost is decreasing, it can still limit their application for small-size engineering works such as energy auditing of a single-family housing. Thus, despite the effectiveness of using a laser scanner for large-scale exterior surveys, it may not be easily applicable for interior surveying purposes in real-world buildings (Lagüela et al. 2012).

In the context of jointly utilizing digital and thermal images and addressing these challenges in using a laser scanner, there have been a few studies on an image-based 3D thermal modeling of building environments. (Lagüela et al. 2012) proposed a method based on image fusion and matching to generate 3D thermal profiles of building exteriors. To do that, thermographic mosaics are initially fused with the corresponding digital images. The fused images are then used as input to the Photomodeler Scanner (PhotoModeler 2012) for 3D thermal modeling purposes. Although this works validates the application of image-based 3D thermal modeling, this involves several semi-automatic processes such as image registration and mosaicking steps, which can be time-consuming and labor-intensive. To be more specific, in order to implement the area-based registration algorithm based on cross-correlation techniques, users need to manually choose

common regions between consecutive thermal image pairs. Moreover, manual verifications are required to eliminate mismatches during feature matching steps. Considering large numbers of unordered thermal images that need to be analyzed, such semi-automated processes will impede the application for building diagnostic purposes. (Stockton 2010) presented a 3D thermal monitoring system to sense, analyze, and manage power and cooling operations in a data center. This implementation involves manually creating image mosaics and performing texture-mappings. Similarly, for 3D thermal modeling of building façades for assessing the as-is condition, (González-Aguilera et al. 2013) leveraged the Photogrammetry Workbench software for image-based 3D modeling. By using the software and thermal camera calibration information, the proposed method produced 3D thermal models and ortho-thermographs for building façades. In the computer vision community, several researches have also addressed the need for 3D thermal modeling (Aksenov et al. 2003; Barker et al. 1995; Gonzalez-Aguilera et al. 2010; Pelagottia et al. 2009; Pelletier and Maldague 1997; Prakash et al. 2007). Although 3D thermal models resulted from the prior works in the computer vision domain are generally accurate and dense, these works are primarily focusing on confined and isolated objects (e.g., small cylindrical shape specimen). Also, these methods do not directly work with typical thermal cameras used in the current building auditing practices. Rather, they have proposed hybrid systems which consist of multiple thermal cameras (e.g., a combination of one digital and two thermal cameras or a thermal camera stereo system) to build 3D thermal models.

2.2 Expected Building Energy Performance Simulation

2.2.1 Current practices using building energy analysis software

Due to assumptions and simplifications typically made during an energy modeling stage, once buildings are operating, the actual energy performance deviates from baseline models. For example, during each modeling set-up, all surface areas in a building element are assumed to have consistent thermal conditions. Due to this assumption, current energy analysis tools may not provide an accurate representation of the as-is building conditions. If the baseline model accurately represents the as-is building performance, the model is more likely to provide reliable energy performance informatics required for analyzing diverse retrofit alternatives. To form accurate baseline models, modelers need to manually calibrate model parameters to minimize the deviations between baseline and actual energy performances. The outcome of this process is the actual building energy

performance model within an acceptable tolerance in accuracy. This is currently a widely accepted energy performance modeling process for existing buildings (Ahmad and Culp 2006; Heo et al. 2012; Reddy 2006). Despite their benefits, there are still several challenges related to their application for building retrofit decision-makings. First, the application of current energy analysis tools often requires several weeks to a few months to manually build a 3D energy model, and therefore it is typically restricted to only high-profile and high budget projects (AIA 2012; Autodesk 2011). Modelers have to spend the significant time and effort for manual building geometry modeling and the performance calibrations as opposed to other valuable tasks such as analyzing energy problems for better decision-makings on the best retrofit alternatives. Second, the results of current energy analysis tools typically do not reflect a real picture of the actual building energy performance (Maile 2010; Tupper 2011; Tupper et al. 2011). According to a recent report by the National Institute of Standards and Technology (NIST) (NIST 2010), one of the top challenges for achieving energy-efficient building is to measure material aging (i.e., the effect of aging on building elements) and implement the associated retrofit actions. Current energy analysis tools are not capable of understanding the spatial distribution of abnormal thermal performance (e.g., building assemblies that contain significant thermal resistance non-uniformity due to construction defects or non-uniform degradation), which is typically prevalent in real-world building environments. Finally, identifying a particular combination of model parameters which results in a good fit between the baseline models and the actual energy performance does not always guarantee that the model accurately represent the actual energy performance because there would be other combinations of model parameters to yield the similar results. During the manual model calibration process, modelers iteratively create new models with different parameter values to find the most proper combination until the deviation is minimal. Consequently, the quality of models relies heavily on the subjective judgment of modelers. Even if the same modeling tools and building characterization data are used, different modelers may not produce the consistent energy modeling results (Azar and Menassa 2012; Tupper 2011; Tupper et al. 2011). According to a survey from a wide range of energy modeling stakeholders (Tupper 2011), one of the major bottlenecks in the current practice was identified as the difficulty in translating the as-is building geometrical and thermal information into right inputs for energy modeling. Since the modeling process requires the selection and adjustment of large numbers of modeling parameters, this process will be vulnerable to modelers' judgement, which is likely to produce inconsistent

outcomes. Overall, although current building energy analysis tools are typically used for comparing different design alternatives, they may not be a proper tool to directly model and analyze the actual energy performance of existing buildings (Maile 2010; Trčka and Hensen 2010).

2.2.2 Building energy performance simulation using the numerical analysis

Today, computational fluid dynamics (CFD) is the most sophisticated type of airflow modeling and simulation used in the building sector. CFD analysis can predict the detailed spatial distributions of temperature and velocity by solving partial differential governing equations for mass, momentum, and energy conservation within each zone of buildings (Somarathne et al. 2005; Zhai and Chen 2003). CFD has been effectively applied to many indoor building environment analyses, and the results are typically more accurate compared to other building performance simulation methods. In contrast to other methods which model space-averaged indoor environmental conditions, the results of CFD analysis provide the more detailed information on building energy performance. For example, to address discomfort problems during winter and identify optimized ventilation opening geometry, (Carrilho da Graça et al.) utilized CFD analysis to simulate indoor airflows. To find optimized configurations, several experiments were conducted on different building envelope permeability levels. (Walker et al. 2011) simulated indoor airflow distributions using CFD analysis to understand buoyancy-driven natural ventilation. They compared the outcomes with the actual data measured by thermocouples in a reduced-scale building model to determine the temperature variations. Based on the CFD analysis, (Li et al. 2009) analyzed the indoor thermal environment of a train station building depending on different types of air-condition systems. They also compared their expected results with the actual measurement data sensed by thermocouples. (van Hooff et al. 2011) used the wind tunnel experiments and CFD analysis to compare and explore the air flow conditions in a venturi-shaped roof for natural ventilation of buildings. All of these studies demonstrate the effectiveness of the CFD analysis for indoor building performance modeling and the comparison with actual measurements for the purpose of validating simulation results. Nonetheless, there is still a need for more systematic comparisons between actual and simulated energy performance in a given space. This is particularly important because in almost all of these cases, a few individual measurements from a few designated locations were used for the purpose of performance comparison. Meanwhile, (Malkawi and Srinivasan 2005) and (Lakaemper and Malkawi 2009) presented a CFD-based

augmented reality environment for immersive visualization of the expected indoor energy performance. Despite the benefits of visualizing building energy performance, the proposed AR environments do not contain the actual energy performance data. Rather, they only show the simulated energy performance overlaid on the surrounding physical environment. If the simulated energy performance can be visually overlaid on the actual energy performance of the associated real-world in 3D, the detailed comparison of the two performances will be facilitated to detect significant performance gaps.

2.3 Quantifying the Actual Thermal Resistance (R-Value) and Detecting Condensation Issues

R-value is an indicator of the ability of building materials to resist heat flows (Desogus et al. 2011). Higher R-value building materials indicate better insulations and have a greater potential for building energy savings. The ability of building materials to resist heat flows typically decreases during the operational phase of a building. As a result, the actual R-value for building elements is most likely to become lower than the notional values declared by their manufactures or those estimated during the design phase (Desogus et al. 2011). Therefore, for energy efficient buildings, there is a need for not only selecting and using high R-value building materials during the design and construction phase, but also looking at how the as-is thermal property of building elements is degraded during the operational phase.

There are two common practices for quantifying thermal resistance of building materials: 1) *destructive method*: aggregating the R-values associated with various layers in a building assembly (ISO 6946); and 2) *non-destructive method*: measuring the heat-flux between the inside and outside of a building. Despite the high accuracy of the destructive method (ISO 6946), it is difficult to disassemble building structures in occupied existing buildings. The destructive methods are even less practical when one considers implementing periodic inspection and maintenance programs to increase the service life of existing buildings. The current non-destructive method regulated by the international standard (ISO 9869) is to position temperature sensors and heat flux meters (HFM) on the representative areas of building elements and directly measure the heat flux.

Recently, few researchers have focused on non-destructive measurement of the actual heat transfer conditions of building assemblies using thermal images. (Madding 2008) is one of the first studies that propose a method for analyzing thermal images to estimate the actual heat transfer conditions through building envelopes. Based on the environmental assumption of a steady-state

condition of heat transfer for building environments, this work measured the R-value of drywall assemblies using the indoor surface temperature data obtained from thermal images. The measurements were conducted in controlled lab environments, and the results were compared with the R-values obtained from manufacturer's specifications. Likewise, by using thermal images and based on similar environmental assumptions, (Fokaides and Kalogirou 2011) proposed a method that measures the overall heat transfer coefficient (i.e., U-value: the reciprocal of R-value) for building envelopes. For validation, the U-values were calculated for a few standard wall assemblies, and the calculated values were compared with 1) the measurement using a thermo-hygrometer, 2) the measurement using HFMs, and 3) the notional values declared in European standards. (Dall'O' et al. 2013) and (Albatici and Tonelli 2010) also used building thermography to measure the U-value of opaque walls on residential buildings in Italy. The thermography-based measurement of thermal property for building assemblies was experimentally verified by comparing the obtained U-values with the theoretical expected values and the method proposed in ISO 9869 (i.e., using HFMs). In these all studies, the difference between the measured values using thermal images and the notional values remained in the range of ~10% (Madding 2008), 10-20% (Fokaides and Kalogirou 2011), and around 15% for cavity walls (Dall'O' et al. 2013). As discussed above, the current standards of non-destructive measurement methods still recommend to use temperature sensors and HFMs placed on representative areas of building elements and directly measure the heat flux. However, considering thermal resistance non-uniformity over surface areas, it is difficult to ensure that thermal resistance measurement by only using a few temperature sensors and HFMs will be representative of the entirety of the building elements (Albatici and Tonelli 2010; Dall'O' et al. 2013). Interestingly, recent studies such as (Albatici and Tonelli 2010) and (Dall'O' et al. 2013) reported 40-80% and 40-175% errors between the measured U-value using HFMs and the notional values. Although this observation is primarily based on limited experiments, yet when one considers the significance of these errors, the applicability of thermography for quantifying the actual heat transfer condition of building assemblies becomes more attractive.

In building environments, water vapor condensation happens wherever exposed building surfaces are at lower temperature than the dew point. Typically, it is not trivial to detect small amounts of condensed water on building surfaces with the naked eye. Failure in detecting the onset of such condensation issues causes the condensed moisture to be accumulated over time. Then, molds and dust mites may build up, which has potential for causing allergic reactions among

building occupants later. In addition, the resulting wet surface may cause flaking paints and peeling wallpapers. This is when most building occupants are more likely to detect the problems with their naked eyes. In building environments, windowsills or thermal bridges around corners of exterior walls typically have low temperatures. Thus, for these areas, energy auditors need to proactively analyze if the dew point has reached to the examined surface temperatures.

Several studies have focused on analyzing the condensation phenomenon on building façades and the associated risk. (Bellia and Minichiello 2003) analyzed the thermal and moisture performance of building assemblies. Their study particularly looked into surface condensation issues on building façades and interstitial condensations within multi-layer walls. (Aelenei and Henriques 2008) investigated external environmental conditions that cause condensation problems in building environments. They concluded that the thermal convection effect and the amount of moisture in air are the most influential factors in forming condensation problems on building façades. These prior works primarily examined the sources of condensation problems and identified ways that can reduce the associated risk. Nonetheless, devising auditing methods that can easily detect condensation problems in building environments is still an open research area. Today, by comparing the surface and dew point temperature, thermal cameras enable 2D detection of those building areas that suffer from condensation issues (Hoff 2011), which is typically conducted on a single image displayed on the screen of a thermal camera.

2.4 Assessing the Value of Investment for Energy Efficiency Building Retrofits

Deciding on recommended retrofit alternatives is not a trivial task for homeowners. This is mainly attributed to the high uncertainty in the financial benefits from retrofit investments. Over the past few years, several research efforts have presented quantitative methods to assess the value of investment for building retrofits (Entrop et al. 2010; Juan et al. 2010; Menassa 2011; Papadopoulos et al. 2002). Papadopoulos et al. (2002) proposed a probabilistic method using Net Present Value (NPV) analysis for assessing financial feasibility of building energy retrofits based on fluctuating energy prices and affordable payback periods. Juan et al. (2010) proposed a retrofit decision support system taking into account the trade-offs between the cost for retrofit, improved building quality through retrofits, and the resulting environmental impacts. Entrop et al. (2010) evaluated the monetary impacts of energy-saving systems installed in residential buildings. Their model consider several financial uncertainties such as interest and inflation rates, and changes in natural

gas and electricity prices. To complement the NPV method, Menassa (2011) proposed a quantitative method for assessing the value of building retrofit investments. The proposed method – based on principles from modern option pricing theory – supports different scenarios for retrofit investment (e.g., single or multi stage investments) and accounts for financial uncertainties. By considering a range of uncertainties for reliable prediction of the associated cash flow, these advanced cost analysis methods for building retrofits have potential to provide building practitioners with managerial flexibility to prioritize and evaluate retrofit alternatives. Meanwhile, current building energy performance modeling and simulation software such as EnergyPlus and Ecotect also have been used to assess the energy cost savings from building retrofit alternatives. For example, (Chidiac et al. 2011) used EnergyPlus to predict the expected energy cost savings on various energy retrofit measures in Canadian office buildings. Similarly, (Poel et al. 2007) used EPA-ED (Energy Performance Assessment for Existing Dwellings) software supported by European standards for calculating the energy cost savings associated with retrofitting existing residential buildings.

2.5 Associating Actual Thermal Property Measurements to BIM Elements

The problems of data interoperability between BIM models and building energy analysis tools have received tremendous interest in the information modeling community. Extensible Markup Language (XML) is a set of rules for designing text format specification, which can give a standard way to define information in BIM models. To support building data transaction, significant success has been reported with the development of XML-based schemas including Green Building XML (gbXML), ifcXML, and Architecture-Engineering-Construction XML (aecXML) (U.S. General Services Administration 2012). Among them, the most common data format for the exchange of building information between BIM models and energy simulation tools is known as the gbXML schema (Sokolov and Crosby 2011; U.S. General Services Administration 2012). Today, many BIM-authoring tools and vendors such as Autodesk and Bentley support the gbXML schema to enable better exchange of building information between BIM models and various engineering applications (gbXML 2013). By importing geometric information from BIM into energy analysis tools and not having to re-create the building geometry within the simulation interface, significant time savings can be realized. In today's practice, the thermal properties of building elements such as thermal resistance or specific heat are typically derived from material specifications or industry

standard databases available in BIM-authoring tools and directly transferred to the energy simulation engine. For reliable modeling and analysis of the energy performance of existing buildings, there is a need for reflecting the as-is building condition in the associated BIM element. In this sense, associating actual thermal properties of building elements to generic construction types in BIM models have recently received attention. (Lagüela et al. 2013) proposed a method for creating 3D textured thermal models by registering thermal images into laser scanning point clouds, and representing their in-situ measurements in gbXML schema manually. A more recent work (Lagüela et al. 2014) proposed a manual method to update thermal property information in BIM models. This work measured actual heat transfer conditions based on a single temperature measurement of a building element using a thermal image. Then, to change the material property in BIM models, they manually matched the corresponding BIM elements with the measurement through visual inspection and finally updated their corresponding entries in gbXML schema.

2.6 Gaps-In-Knowledge

(1) To address the challenges in scaling and localization issues in 2D thermography-based inspection, prior works using a laser scanner with a thermal camera would be useful for a large-scale 3D thermal modeling (e.g., city-level), yet they have several technical and practical challenges that make their application difficult to easily adopt for complex and confined environments which are prevalent in real-world building environments. Rather, 3D thermal modeling methods need to be more scalable so that they can be widely applied to both indoor and outdoor environments. In this sense, for the purpose of 3D thermal modeling, more research needs to be done to directly utilize a consumer-level thermal camera alone without adding any burden to energy auditors. Prior works on image-based 3D thermal modeling of building environments still involve several manual processes. Considering large amount of unordered visual data that need to be analyzed, there is a need for an automated method for 3D thermal performance modeling. This can allow energy auditors in the process of identifying potential performance problems to spend less time on browsing large amounts of visual data; rather spend more time on looking at the as-is building condition in a holistic manner to facilitate the associated energy efficient retrofit decision-makings.

(2) Analyzing the deviations between actual energy performance metrics and the associated benchmark can support to identify potential energy problems in building environments. Prior

works on comparing actual and expected building performance to detect the deviations primarily focused on 'manual' and 'a limited number of sampling points' based comparison, which can be time-consuming for large building areas and inconsistent if the assembly contains thermal property non-uniformity and has irregular characteristics such as construction defects or partial degradations. Thus, for applying to the identification of potential energy problems in building environments, there is a need for a systematic method that can assist with detection and measurement of performance deviations by automatically comparing the actual and expected building energy performance in a holistic manner. To do that, actual 3D spatio-thermal models need to be superimposed with expected performance models (i.e., benchmark based on 'as-designed' building information) for analyzing performance deviations at the level of point in 3D.

(3) Prior works on measuring the actual R-value presented promising results and showed the applicability of thermography for reliable quantification of the as-is heat transfer condition of building assemblies. Nonetheless, the direct application of 2D thermography as used in the prior works for as-is building condition assessment purposes is challenging. To measure the as-is thermal resistance using building thermography, prior works extract a single or at most a few temperature data from the designated building areas captured in 2D thermography (i.e., a few sampling data points for each building assembly under inspection), and then a single measurement of the actual heat transfer condition was conducted for each building assembly. Hence, prior works assumed that the single thermal resistance measurement is representative of the all spots on the designated building elements. If the building assembly is relatively uniform, then the thermal resistance of the assembly can be characterized by taking temperature readings at a few location. However, if the assembly is highly variable or has irregular characteristics such as construction defects or partial degradations, then multiple readings are needed to accurately characterize the assembly's actual heat transfer conditions across geometrical forms. In this sense, the prior 2D sampling point-based methods may not accurately represent the dynamic variation of the as-is thermal resistances in real-world building environments. Thus, there is a need for a method that can better characterize the as-is building condition at small scale as opposed to a single measurement for each building element conducted in prior works. In particular, if such dynamic variations can be interactively visualized in the context of the associated building geometrical characteristics in 3D, building practitioners will be more likely to better understand the as-is building conditions. Regarding building condition assessments for diagnosing condensation issues,

a few recent thermal cameras support the option that can detect building areas suffering from condensation issues by comparing surface temperatures with the dew points. Despite the benefit, the detections are conducted in a single image displayed on the camera screen, which is not geo-tagged in building environments. Thus, it is often not trivial to figure out at a later stage 'which building areas associate with the detected condensation problems'. Moreover, prior works do not provide any information about the surface area associated with the detected condensation problems. Hence, it is difficult to quantitatively estimate the impact of the detected condensation issues.

(4) Prior works on quantitative methods to assess the value of investment for building retrofits do not account for the inherent uncertainty in techniques for quantifying the expected energy cost savings from energy efficiency retrofits. Instead, based on historical data or expert opinions, it is assumed that the energy cost savings from building retrofits is known as *a priori*. It is hypothesized that the prior works on assessing the value of retrofit investment under uncertainty – together with the proposed thermography-based method that can reliably quantify the energy cost savings from building retrofits – would yield more reliable predictions on cash flow for energy cost savings. In the case of using current building energy performance analysis software for estimating energy cost saving from retrofits, it is assumed that the entirety of each building component (e.g., windows) will be replaced with new ones, and thus do not account for non-uniform defects across the geometrical form of building elements. Hence, these tools cannot accurately model and analyze the as-is building conditions influenced by small-scale energy problems which are typically prevalent in real-world building environments (e.g., injecting loose-fill insulation in the cavities of a part of existing building's façades). To provide practitioners with a better standing point for energy efficient retrofit decision-makings after thermographic inspection, there is a need for a systematic method that can reliably quantify the expected energy cost saving from retrofitting thermal defects.

(5) Regarding associating actual thermal properties to corresponding BIM elements for reflecting as-is building condition in BIM-based energy modeling process, prior works still have several challenging issues. First, manually identifying the relevant BIM elements for each measurement and updating their thermal properties in the gbXML entry would be time-consuming and prone to errors. This problem is exuberated when large numbers of thermal images and BIM elements are considered for updating in real-world building environments. In addition, for calculating the as-is thermal properties of building assemblies that need to be updated, a prior work

(Lagüela et al. 2014) used the point-based sampling method described in (3), which is difficult to accurately characterize the as-is building condition non-uniformity in real-world building environments. To improve BIM-based energy modeling and analysis by addressing limitations listed in (U.S. General Services Administration 2012), there is a need for an automated method for matching actual thermal property measurements to associated BIM elements and updating the attribute of the BIM elements.

CHAPTER 3. RESEARCH OBJECTIVES

Objective 1: Given a collection of unordered yet paired digital and thermal images captured from a thermal camera, the first goal is to propose a new computer vision-based method for automated 3D spatio-thermal modeling of building environments from images and localizing the thermal images into the 3D reconstructed scenes.

Research Questions: How can we automatically generate 3D spatio-thermal models by using a consumer-level thermal camera alone? How can we automatically geo-register unordered thermal and digital images in 3D virtual building environments?

Significance: This will address the challenges in scaling and localization issues of 2D image-based inspection, which help better characterize the as-is building condition in 3D. To be more specific, the proposed method has potential to reduce the time and efforts required for analyzing large numbers of raw 2D thermal images which have a low spatial resolution and small field-of-view to inspect the as-is building condition. Compared to the other 3D thermal modeling approaches such as the application of a laser scanner, the proposed method can automatically generate 3D spatio-thermal models in both interior and exterior building environments without any space limitations (e.g., complex and confined indoor environments) by using a consumer-level thermal camera alone (i.e., without adding any burden to energy auditors). The automatically 3D-registered thermal profiles can further minimize auditors' time and effort to find 'where certain thermal images representing energy defects were captured from' or 'what building components they are representing' during the post-examination stage. As a powerful communication tool to effectively illustrate the as-is building condition to practitioners, the integrated visualization of 3D building geometrical and thermal models, in addition to 3D-registered images, will enable energy auditors to virtually walk-through in buildings and explore the as-is conditions of building geometry and the associated thermal conditions in 3D. This will increase the auditors' inspection time in 3D virtual environments, as opposed to on-site inspection in real-world buildings.

Objective 2: Given actual 3D spatio-thermal models and expected performance models (i.e., energy performance benchmark) based on 'as-designed' building information, the second goal is to 1) create a new Energy Performance Augmented Reality (EPAR) environment which jointly models actual and expected building thermal performances in a common 3D environment; 2)

automatically calculate performance deviations; and 3) visualize potential energy problems with the associated digital and thermal images in 3D.

Research Questions: How can we overcome the challenges in the current thermographic inspection based on auditors' knowledge and experiences? How can we generate and use a benchmark model to compare with the as-is building condition in 3D? How can we automatically compare two models at the level of 3D point across geometrical forms of building elements and infer potential performance problems in 3D building environments?

Significance: Leveraging energy performance benchmark allows auditors to objectively interpret the as-is building condition. Through a systematic comparison of actual and expected surface thermal profiles in 3D, performance gaps above the pre-defined threshold can better inform practitioners about feedback on 'what areas require additional detailed diagnostics'. The 3D approach makes better use of continuous 3D thermal profiles converted from 2D thermography for performance comparison. Here, the image-based 3D thermal point clouds would be incomplete or noisy including several points physically deviated from the associated building geometry. Thus, manual selections of the closest point pairs between the actual and expected 3D thermal models for performance comparison are often not trivial and prone to errors. The automated approach for performance comparison can facilitate the process of calculating performance deviations from benchmark values and further help identify potential performance problems. Ultimately, by being able to focus on energy problem candidates in need for detailed diagnostics, auditors can spend less time on browsing large amounts of visual data; rather spend more time on looking at the performance problems to facilitate the associated energy efficient retrofit decision-makings.

Objective 3: Given 3D thermal models in EPAR environments, the third goal is to create and validate a new non-destructive method for quantitative assessment of the as-is building conditions that 1) calculate the as-is thermal resistance of building assemblies at the level of 3D point; 2) detect condensation problems; and 3) visualize the outcomes in an intuitive 3D form to effectively communicate with building practitioners.

Research Questions: How can we convert 3D surface temperature distributions obtained from 2D thermography into the associated energy performance metrics such as R-value and condensation issues at the level of 3D point and effectively visualize them?

Significance: By converting 3D surface temperature distribution into energy performance

metrics such as thermal resistances and condensation issues, the proposed method reduces the need for subjective and qualitative interpretation of building thermography, which has potential to improve the quality of thermographic interpretations. Here, if the building assembly is relatively uniform, then the heat transfer conditions of the assembly can be characterized by taking temperature readings at a few location. However, if the assembly is highly variable or has irregular characteristics such as construction defects or partial degradations (i.e., various regions across geometrical forms of building elements may suffer from different levels of degradations and as such their conditions would change differently over time), then multiple readings are needed to accurately characterize the assembly's actual heat transfer conditions across geometrical forms. Without physically collecting temperature readings from large numbers of uniformly spaced locations on the building envelope, characterizing façade's thermal properties with a few heat flux sensors or 2D thermography may be inaccurate. The proposed 3D thermography-based vertex-level measurement will better characterize the as-is building condition at small scale because each vertex in 3D thermal models represents the absolute temperature value of building surface, and it is converted into the as-is thermal resistance value and condensation issues, which represent the dynamic variation in the as-is conditions of real-world building environments. This will complement the heat-flux-sensor measurements to determine heat transfer values for large areas of building envelope that contain significant thermal resistance non-uniformity. In addition, the proposed method localizes building areas associated with performance problems such as decreasing thermal resistances or condensation problems into 3D reconstructed scenes and also calculates the size of the associated building areas in 3D mesh models, which help auditors to quantitatively analyze the impact of the detected problems.

Objective 4: Given the as-is thermal resistance measurements at the level of 3D point and building areas associated with potential performance problems detected in EPAR models, the fourth goal is to create and validate a new model-based method that 1) calculate the amount of heat transfer that can be saved by improving the as-is thermal resistances of defective areas to the recommended level; and 2) convert it into the equivalent energy loss cost.

Research Questions: How can we overcome the challenges in the current thermographic inspection for qualitative purposes only? How can we reliably quantify 'how much money can be saved if the problems observed in EPAR models are retrofitted' and further help homeowners to

do better decision makings for building retrofits?

Significance: When diagnosing small-scale energy problems which are typically prevalent in real-world building environments, the proposed method will complement current building energy performance analysis tools. If practitioners want to replace old building elements (e.g., windows) with new one and estimate the expected energy cost saving, they can use the current energy analysis tools. However, because the current tools assume that each building assembly has a constant surface-wide thermal property, they cannot model small-scale and non-uniform energy problems. To address this issue, the proposed method leverages 1) the automated identification of potential performance problems and the as-is thermal resistance measurement for the defective areas at the level of vertex in EPAR models; 2) the R-value recommendations as energy performance benchmarks; 3) unit energy price such as electricity or natural gas depending on the source of energy used for heating and cooling system in the buildings under inspection; and 4) 'degree days' statistics reflecting historical weather data. By using these parameters, the proposed method calculates the amount of heat transfer that can be saved by improving the as-is thermal resistances of the defective areas to the recommended level. Although few uncertainties still exist, compared to the current practices on offhand calculations based on the historical cost data of the industry best practices, the proposed method can offer reasonable guidance for quantifying expected energy cost savings from retrofitting thermal defects, which provide building practitioners with a better standing point for retrofit decision makings.

Objective 5: Given 3D thermal models in EPAR environments and the as-designed BIM models, the fifth goal is to create and validate a new automated method for 1) mapping actual thermal resistance measurements at the level of 3D point to the associated BIM elements; and 2) updating their corresponding thermal properties in gbXML schema.

Research Questions: How can we use building thermography to reduce the existing energy performance modeling gap between the architectural information in the as-designed BIM and the as-is building conditions? How can we accurately model energy performance of existing buildings and better predict the associated energy consumption through BIM-based energy analysis?

Significance: Without considering diminishing thermal properties of building assemblies in BIM models, BIM-based energy analysis for existing buildings is more likely to overestimate their energy performance. The proposed method enables an energy simulation engine for thermal

load calculation to use the as-is thermal properties of BIM elements reflecting the as-is building conditions, rather than using the notional properties typically declared in the material specifications or industry standard databases (e.g. ASHRAE data) available in current BIM-authoring tools. This allows the BIM-based energy analysis to be conducted with greater granularity of input parameters relevant to thermal properties, which has potential for improving the reliability of the BIM-based energy modeling and simulation for existing buildings.

By using the proposed method, gbXML-based BIM models do not need to be manually updated, which reduce the time and efforts required for model calibration. The proposed method has potential to be used for newly constructed building environments as well. In contrary to occupied buildings, such buildings are typically empty from furniture and other installments. As an intensive quality assurance process during building commissioning, the proposed method can be used to check if the new building is operating as the owner initially intended without any faulty constructions such as improper installations. When a building is initially commissioned, the proposed method can also estimate the as-is thermal property of unique building materials or customized construction types. For example, in the case of historic building façades that are typically not uniform in their construction and use materials that are not standard in today's material database, the proposed method can help define the associated thermal property information as opposed to using substitutions in existing literatures, which further enables auditors to conduct more reliable energy analysis. Finally, by using updated databases of actual thermal properties of BIM elements, the time series trend of thermal characteristics of building elements and their impact on the energy load estimation can be further analyzed.

CHAPTER 4. 3D SPATIO-THERMAL MODELING OF BUILDING ENVIRONMENTS

Given a collection of digital and thermal images captured from a thermal camera which has a built-in digital camera, the first goal is to propose a new computer vision-based method for automated 3D spatio-thermal modeling of building environments from images and localizing the thermal images into the 3D reconstructed scenes. In this research, digital images are capturing the actual geometrical information of existing buildings, and thermal images are capturing the instantaneous thermal profiles of the buildings under inspection. The data and process for 3D spatio-thermal modeling are illustrated in Figure 4.1.

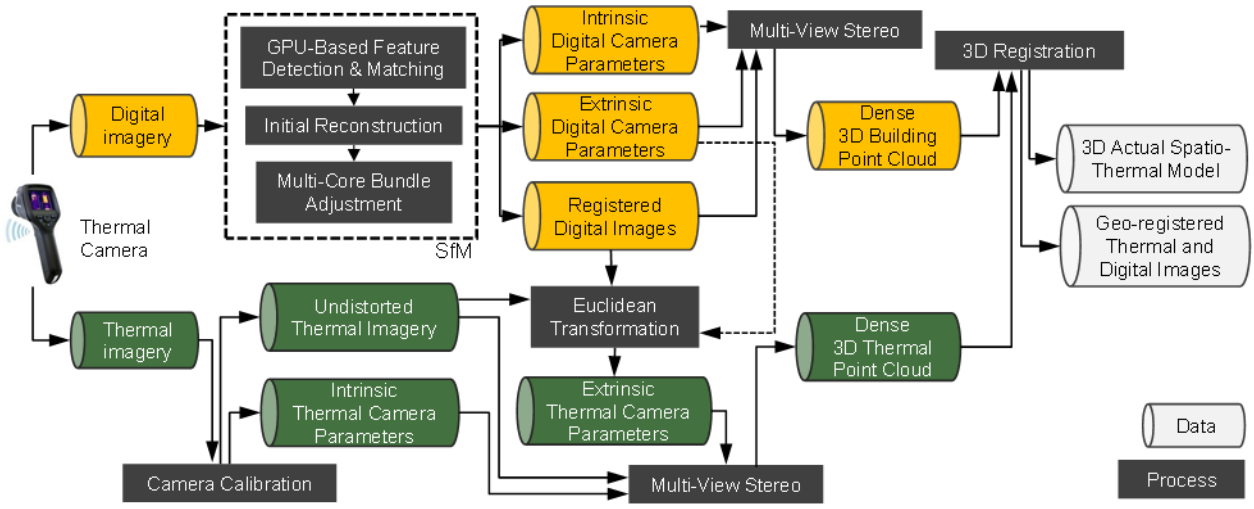

Figure 4.1 Overview of the Data and Process for 3D Spatio-Thermal Modeling of Building Environments

As observed in Figure 4.1, once thermal and digital images are captured simultaneously, the following steps are conducted: (1) the digital images are placed into an image-based 3D reconstruction pipeline which consists of a new Graphic Processing Unit (GPU)-based Structure-from-Motion (SfM) and Multi-View Stereo (MVS) algorithms to automatically generate dense 3D point clouds of building environments; (2) the thermal camera is internally calibrated, and as a result the focal length and radial distortion parameters of the thermal camera are calculated. Then, by forming the Epipolar geometry between digital and thermal camera lenses, the relative pose of the thermal camera lens with respect to the digital camera lens are calculated, and the extrinsic parameters of the thermal camera are derived. Based on the intrinsic and extrinsic parameters of

the thermal camera, the camera projection matrices for all thermal images are formed. Using the MVS algorithm, dense 3D thermal point clouds are then generated; (3) to form the 3D spatio-thermal models, the 3D building geometrical and thermal point clouds are automatically superimposed along with the 3D-registered digital and thermal images. The outcome is a 3D virtual environment in which 3D spatio-thermal models along with the associated digital and thermal images are integrated and jointly visualized. The following sections describe each step in detail (Ham and Golparvar-Fard 2013).

4.1 Image-based 3D Reconstruction of Building Geometry

A camera maps the contents in the 3D world into 2D imagery. Such transformation is represented by a 3×4 camera perspective projection matrix (M_T) which maps from homogeneous coordinates of a world point in 3D to homogeneous coordinates of the images point on a 2D image plane. M_T consists of camera intrinsic and extrinsic parameters (Hartley and Zisserman 2004). Camera intrinsic parameters (K) include the focal length, skew factors, lens distortion, and the position of an image's center point. Camera extrinsic parameters include the pose and location of the camera which indicate translation (T) and rotation (R). This represents the transformation from the origin of the scene's 3D coordinate system to the origin of each camera's local 3D coordinate system. Assuming a pinhole camera model, M_T is formulated as:

$$x = K_{3\times3}[R_{3\times3}|T_{3\times1}]X = M_{T\ 3\times4}X \quad (1)$$

Where X is a 3D point in a world coordinate frame (in form of a homogeneous 4-vector $[x, y, z, 1]^T$), x is a 2D point in a camera coordinate frame (in form of a homogeneous 3-vector $[x, y, 1]^T$). The resulting M_T is used to reconstruct the as-is 3D building geometrical model.

4.1.1 GPU-based Structure-from-Motion (SfM)

First, using an image-based 3D reconstruction method known as Structure-from-Motion (SfM) (Snavely et al. 2008), intrinsic and extrinsic camera parameters are computed from a given set of digital images. To reduce the computational cost, a new GPU-based Structure-from-Motion (SfM) algorithm is used: (1) distinct visual features are automatically detected and matched across all

digital image pairs. Here, the GPU-based implementation (Wu 2007) of the Scale-invariant feature transform (SIFT) keypoint detection (Lowe 2004) is conducted. This implementation rapidly finds distinctive feature points which are invariant to changes in rotation, scale, and scene illumination; (2) once these features are detected independently in each image, their descriptors are matched across each image pair using a nearest neighborhood matching algorithm to further expedite the matching process. Then, the Epipolar geometry between each digital image pair are formed by estimating the Fundamental matrix (F) within a RANdom SAmple Consensus (RANSAC) algorithm (Fischler and Bolles 1981). Fitting F in the RANSAC loop helps remove false matches as it enforces the corresponding features to have consistent transformation:

$$p^T F p' = 0 \tag{2}$$

Where p and p' are the homogeneous coordinates of the corresponding feature points in each image pair. Considering that many building elements are likely to have similar visual features in the context of building environments (e.g., repetitive patterns), this process can eliminate the associated mismatches that are not consistent by the general transformation from one camera location to another. If more than one features in image *i* match the same feature in image *j*, both of such matches are removed as one is a false match (Hartley and Zisserman 2004); (3) Once the feature matches are formed, an initial pair of matching features is selected for initializing the 3D reconstruction process. For selecting the initial pair, the selection heuristics proposed in (Snavely et al. 2008) are used in which the pair with 1) maximum percentage of matching features inliers after fitting *F* within the RANSAC loop and 2) minimum percentage of matching features inliers after fitting a Homography matrix within the RANSAC loop are selected. Starting from an initial 3D reconstruction, additional camera poses and locations of the 3D points are incrementally computed. Each time a new camera is added, and the new camera's parameters are also estimated using DLT within the RANSAC loop. Once each camera is added, the bundle adjustment algorithm (Triggs et al. 1999) automatically optimizes the camera parameters and the locations of the 3D points. Here, the GPU-based bundle adjustment library (Wu et al. 2011) is used, which significantly cuts the computation time. This process is repeated for all cameras until no cameras which observe any reconstructed 3D point remain. The outcome of this process is a sparse 3D point cloud along with intrinsic and extrinsic parameters of the digital cameras, which will be fed

into the next step.

4.1.2 Dense 3D reconstruction

Generating dense 3D building point cloud models is primarily inspired by the Multi-View Stereo (MVS) algorithm (Furukawa and Ponce 2008). The following two data structures are used to generate dense 3D building geometrical point clouds: 1) A set of camera projection matrices derived from the SfM algorithm (Section 4.1.1); and 2) undistorted digital images for which the radial distortion are minimized. There are three main components to this algorithm: *matching*, *expanding*, and *filtering* procedures. First, features detected by Harris and Difference-of-Gaussians operators are primary matched for all images, yielding a sparse set of 2D patches (possibly containing some false positives) during an initial feature matching step. Then, the expansion and the filtering steps are iterated to make patches dense and remove false matches by using visibility constraints. The size of the patch and the number of target images control the density of 3D reconstruction. Since this algorithm intends to reconstruct at least one patch in every square region in all the registered images, the increase of the patch size results in sparser 3D reconstructions. On the other hand, since the underlying reconstruction process generates 3D point clouds until image projections of these points cover all the registered images, the increase of the number of target images results in denser 3D reconstructions. The final outcome is dense 3D building point clouds which represent the geometrical conditions of building environments, along with the digital images that are 3D-registered with respect to the underlying 3D reconstructed scene.

4.2 Automated 3D Thermal Modeling of Building Environments

To generate 3D spatio-thermal models, digital and thermal images need to be co-registered in a common 3D environment to map the thermal values into the reconstructed building elements. To that end, the initial approach for 3D thermal modeling was to directly use the SfM algorithm (Section 4.1.1) by forming the Epipolar geometry (Hartley and Zisserman 2004) between 1) every pair of digital and thermal images or 2) every two thermal images, and computing the F within the RANSAC loop. For this purpose, several experiments on the state-of-the-art invariant feature detection and matching algorithms were conducted to initiate the SfM process for unordered thermal images. These methods included SIFT, Affine-SIFT (ASIFT), and Speeded Up Robust Feature (SURF). In all of the experiments, these feature detection and matching algorithms worked

very poorly or did not work at all. In most cases, the number of matching feature points before fitting *F* in the RANSAC loop were less than 10 features with a strong probability of significant mismatches among these paired feature points. Figure 4.2 (a) and (c) illustrate an example of the thermal and digital image simultaneously captured from the same camera location; (b) and (d) highlight the detected SIFT feature points (236 and 14,946 SIFT keypoints detected in (a) and (c)), and (e) displays only 8 keypoints that were automatically matched between the pair of the digital and thermal image). As observed, not only the number of matching points is minimal (<10 features), but also most of these feature points are incorrectly matching. Figure 4.2 (g) and (i) further illustrate 159 and 236 SIFT keypoints detected in (f) and (h) while (j) shows only 20 keypoints that were automatically matched, which shows the limitation of the feature detection and matching algorithms between a pair of thermal images from the same scene.

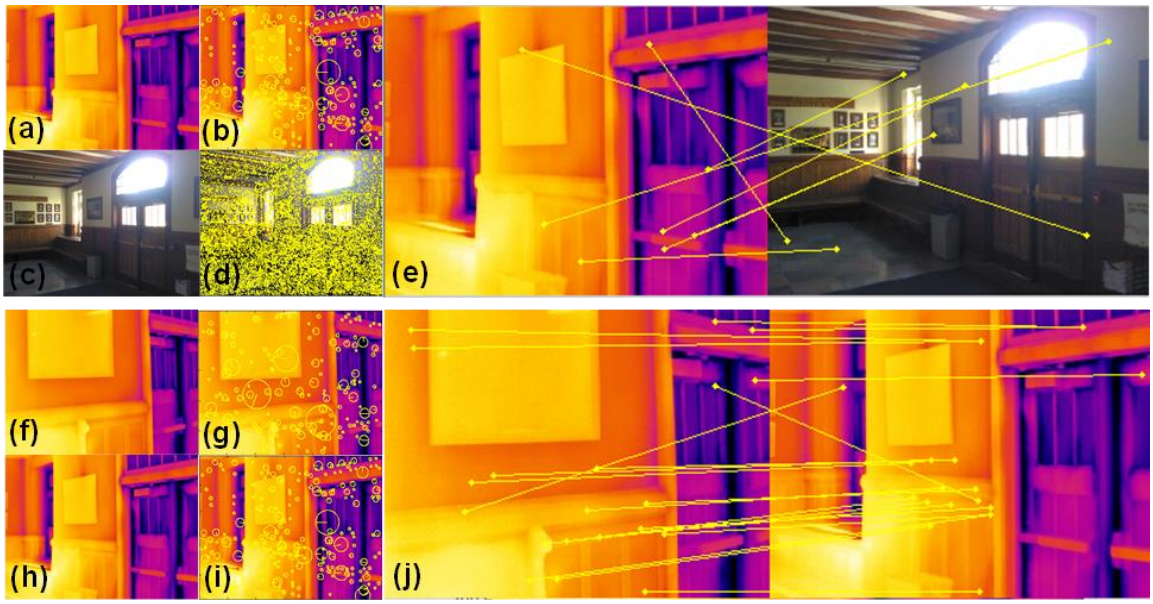

Figure 4.2 Examples on the Limitation of the State-of-the-Art Feature Detecting and Matching Algorithms between 1) Digital and Thermal Imagery and 2) Thermal images

Such poor performance is primarily caused by the inherent characteristics of thermal imagery: (1) Thermal images capture the subtle variations of the surface temperatures and represent them using color gradients. This typically smoothens sharp changes of intensity in the captured images (Figure 4.3). These characteristics impede direct application of feature detecting and matching methods on unordered collection of thermal images which are the key components of the SfM procedure; and (2) Another technical challenge is that the variations of the building

surface temperature in thermal images do not usually correspond to real-world textures or patterns depicted in the corresponding digital images (Figure 4.3). This issue is exuberated when thermal images are captured from building interiors. Thus, the computer vision feature detection algorithms that search for pixels with higher intensity compared to their surroundings in the initially convolved images do not return consistent feature points across a set of thermal and digital images from the same viewpoint.

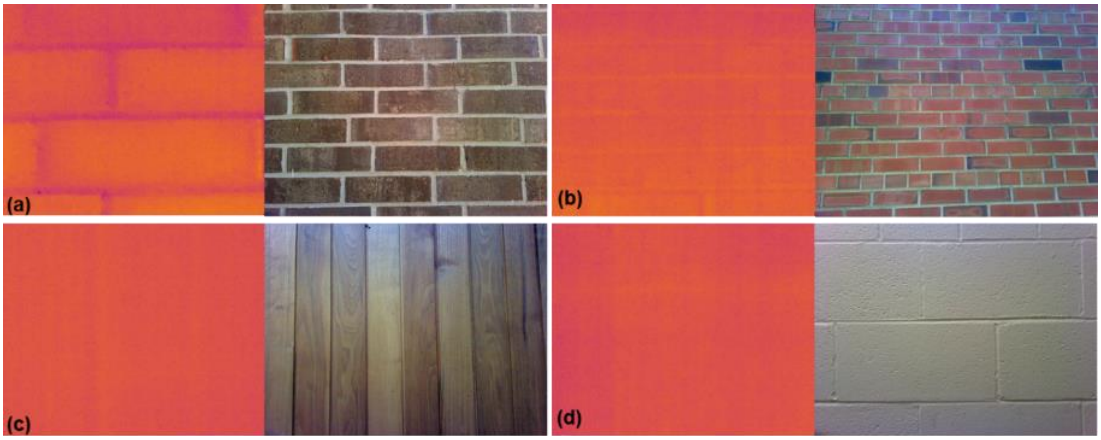

Figure 4.3 Examples of Thermal and Digital Images Captured from Different Building Surfaces: (a) exterior brick wall; (b) brick wall; (c) interior wooden wall; (d) interior concrete masonry wall

Hence, there is a limitation to directly use SfM algorithms on unordered thermal images and generate 3D thermal point cloud models. To overcome this challenge, a new 3D thermal modeling method is proposed which includes the following steps (Ham and Golparvar-Fard 2012).

4.2.1 Internal calibration of a thermal camera using a thermal calibration field

Prior to calibration, varying ranges of temperatures in each thermal image are normalized to a fixed color spectrum so that a RGB color value of each point corresponds to an absolute temperature value. Then, the intrinsic parameters of the thermal camera (i.e., the focal length and radial distortion parameter) are computed through an internal calibration process. To calibrate general digital cameras, a calibration checkerboard is typically used (Bouguet 2010). However, because thermal cameras are only capable of detecting thermal variations emitted by objects in a scene, it is not easy to clearly distinguish intersecting corners and lines of the conventional calibration field. In this sense, a thermal calibration field ($550\times700mm$) based on emissivity differences by using small LED lights located on the intersections of the conventional

checkerboard (δ=10cm) is designed to calibrate the thermal camera (Figure 4.4). Once the LED lights are on, they generate enough heat so that they easily distinct themselves from the surrounding environment.

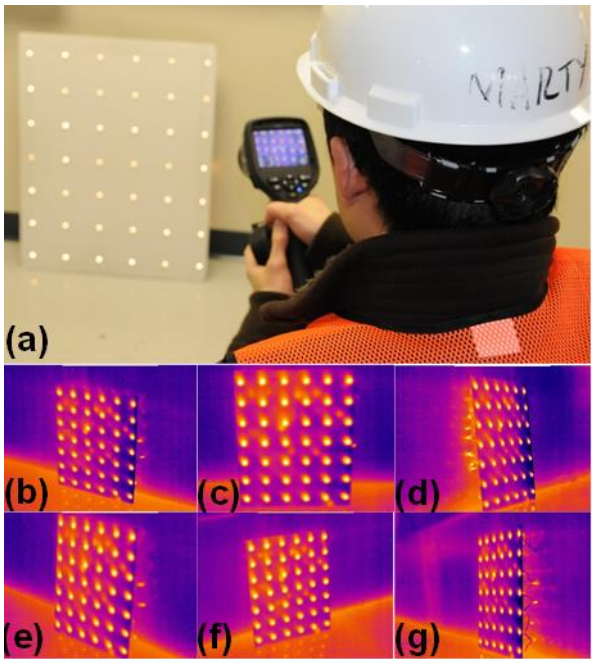

Figure 4.4 One-time Internal Calibration of a Thermal Camera Using a Thermal Calibration Field

The camera calibration tool box (Bouguet 2010) is used to internally calibrate the thermal images (i.e., the focal length (f^T) and radial distortion parameters (k_T^1 and k_T^2) of the thermal camera are calculated). In the formulation of the pinhole camera projection, it is assumed that 2D images have no radial distortion. Nonetheless, in practice, thermal camera lenses create significant radial distortions and require proper corrections. Thus, assuming a pinhole camera model, the radial distortion of thermal images is removed. The thermal images with pixels denoted as $p = [u, v, 1]^T$ are undistorted by using the following equation:

$$p^{undistorted} = f^T \times r\left(p^{distorted}\right) \times p^{distorted} \quad (3)$$

In this equation, $r(p)$ is a function that computes a scaling radial factor to undo the distortion:

$$r(p) = 1.0 + k_T^1 \times \|p\|^2 + k_T^2 \times \|p\|^4 \quad (4)$$

Since most thermal cameras for building energy diagnostics use a fixed thermal lens, this process only needs to be conducted once per camera and does not need to be repeated per data collection process. Hence, it does not add any burden to auditors as this information can be precompiled in the implementation of the proposed method.

4.2.2 Calculating relative pose of a thermal camera with respect to a digital camera

The next step is to calculate the extrinsic parameters of the thermal camera (i.e., location and orientation). For this purpose, the extrinsic parameters of the digital camera are first extracted from the outcome of the GPU-based SfM algorithm (Section 4.1.1). To calculate the extrinsic parameters of the thermal camera, the relative pose of the thermal camera lens with respect to the digital camera lens is derived by forming the Epipolar geometry between matching features of a pair of thermal and digital images. These feature points are selected in a supervised manner. To find the relative pose between two cameras, the Essential matrix is computed based on calculating coefficients of a tenth degree polynomial and extracting the roots using Nistér's five point algorithm (Nister 2004). The Essential Matrix encapsulates the Epipolar geometry between the two cameras (Figure 4.5).

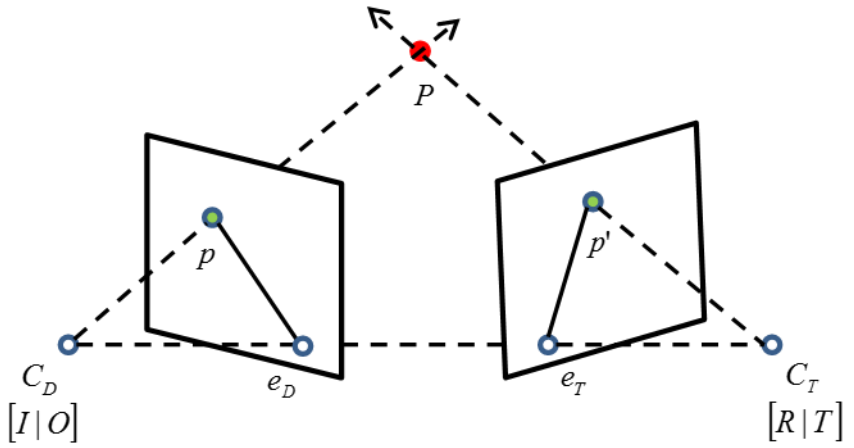

Figure 4.5 Epipolar Geometry for a Pair of Thermal and Digital Images (C_D and C_T are the Digital and Thermal Camera Centers, and e_D and e_T are the Epipoles respectively)

Here, it is assumed that the digital camera located at the origin of the coordinate system

has an identity rotation and zero translation (i.e., the digital camera's extrinsic matrix = $[I|O]$). The relative rotation and translation of the thermal camera is determined through the Singular Value Decomposition (SVD) of the Essential Matrix. The outcomes of this step are four possible solutions for the relative pose of the thermal camera with respect to the digital camera. Among them, only one set corresponds to the true configuration. The other sets correspond to twisted pairs obtained by rotating the views by 180° around the baseline, and the remaining two parameters correspond to reflections of the true and the twisted configurations. To determine which extrinsic parameter corresponds to the true configuration, the Cheirality constraint (Hartley and Zisserman 2004) is imposed. Only one pair of matching feature points among the five candidates is enough to check for the constraint and resolve the ambiguity. First, the selected matching points are triangulated using the DLT algorithm assuming [I | 0] for the digital camera and using the four candidates for the R_{rel} and T_{rel}. For each of the four candidates, this process yields a 3D point Q. This point is tested using the Cheirality constraint:

$$\text{If } C_1 \equiv Q_3 Q_4 > 0 \text{ and } C_2 \equiv (P_i Q)_3 Q_4 > 0, \text{ then return } P_i \text{ and Q} \tag{5}$$

Where Q_3 and Q_4 are the third and fourth components of the Homogenous coordinates of the point Q, and $P_i = [R_{rel} \mid T_{rel}]$ is the relative pose of the thermal camera with respect to the digital camera. Based on the rotation and translation of the digital camera (R_D and T_D) along with the transformation matrix between the thermal and digital lens [R_{rel} | T_{rel}], the extrinsic parameters of the thermal camera are calculated by Equation (6). Figure 4.6 summarizes the proposed algorithm.

$$[R_T|T_T] = [R_D R_{rel}|R_D T_{rel} + T_D] \tag{6}$$

Input: The extrinsic parameters of the digital camera $[R_D|T_D]$, An image pair of digital and thermal imagery with a minimum of five keypoint correspondences

Output: $[R_T|T_T]$ of thermal camera

```
select a minimum of five correspondences between digital and thermal images
estimate E matrix in RANSAC loop
derive four R_rel and T_rel solutions from the Singular Value Decomposition (SVD) of E
        for each solution
          triangulate a correspondence Q in 3D using DLT algorithm
          if C_1 ≡ Q_3 Q_4 > 0  and C_2 ≡ (P_i Q)_3 Q_4 > 0
            wherein Q=[Q_1 Q_2 Q_3 Q_4], and P_i = [R_rel|T_rel]
            return [R_rel|T_rel]
            Break
          end if
        end for
  [R_T|T_T] = [R_D R_rel|R_D T_rel + T_D]
  return [R_T|T_T]
```

Figure 4.6 Algorithm for Deriving the Extrinsic Parameters of Thermal Cameras by Calculating the Relative Transformation between the Thermal and Digital Camera

4.2.3 Dense 3D thermal modeling

Once the thermal camera intrinsic parameters are derived from the calibration process (Section 4.2.1) and the extrinsic parameters are calculated based on the relative pose estimation (Section 4.2.2), generating 3D thermal point clouds converts into the classical problem of reconstructing 3D scenes using a set of calibrated images. Because thermal images are now fully calibrated, for the purpose of generating dense point cloud models, the derived thermal camera projection metrics and undistorted thermal images are placed into the MVS algorithm presented in Section 4.1.2. The outcome of this process is dense thermal point clouds of building environments in which thermal cameras are geo-spatially registered in 3D.

4.3 Integrated Visualization of 3D Building Geometrical and Thermal Models

The last step for 3D spatio-thermal modeling is to align the reconstructed 3D building geometrical and thermal point clouds in a common 3D environment. Since the 3D thermal model was reconstructed by estimating the relative pose of the thermal camera lens with respect to the digital camera lens, both models are in the same coordinate system. Thus, superimposing these two models simply involves bringing two point cloud models into a 3D environment. This also enables both digital and thermal images to be 3D-registered within the same 3D virtual environment.

CHAPTER 5. ENERGY PERFORMANCE AUGMENTED REALITY (EPAR) MODELING

5.1 Integrated Modeling and Visualization with Benchmark Performance

Given 3D spatio-thermal models and expected performance models (i.e., energy performance benchmark) based on 'as-designed' building information, the second goal is to (1) create a new Energy Performance Augmented Reality (EPAR) environment which jointly model actual and expected building thermal performances in a common 3D environment; (2) automatically calculate performance deviations; and (3) infer and visualize potential energy problems with the associated images in 3D. The data and process for EPAR modeling are illustrated in Figure 5.1.

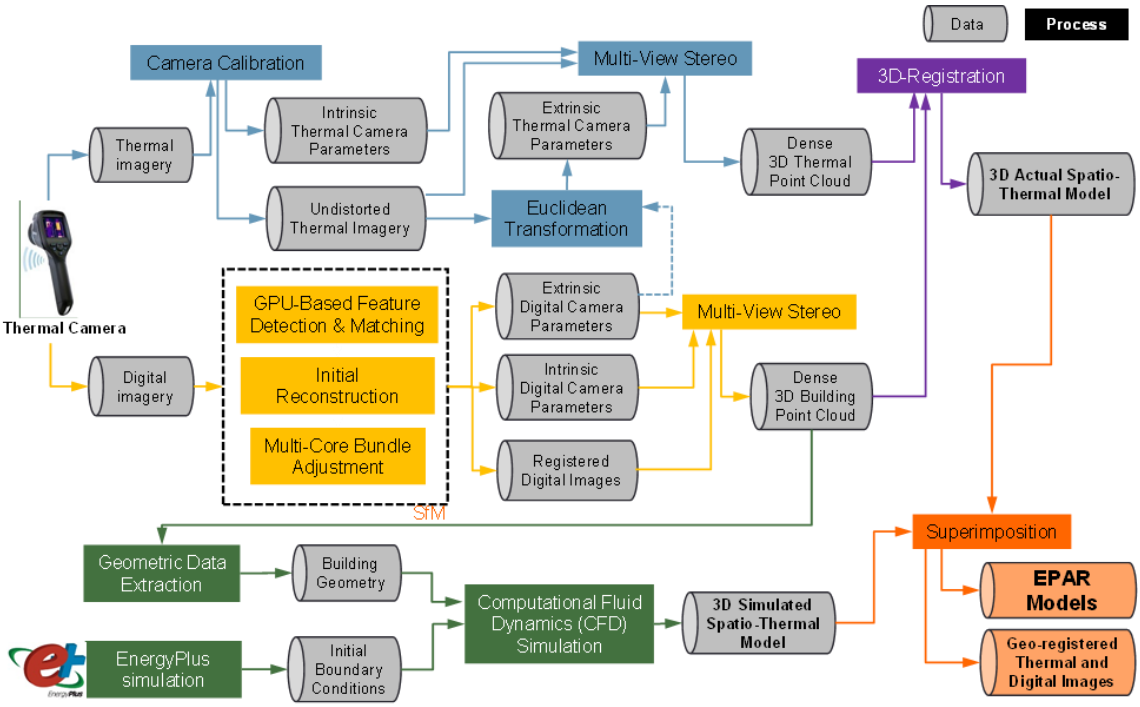

Figure 5.1 Overview of the Data and Process for EPAR Modeling

The approach mainly consists of three parts: (1) first, based on the computer vision-based pipeline for 3D reconstruction presented in Section 4, 3D spatio-thermal models of building environments are generated by using a set of thermal and digital images collected from a thermal camera. Here, a thermal camera with a built-in digital camera is used to simultaneously capture pairs of thermal and digital images. The resulting 3D thermal point clouds are then automatically

superimposed with the 3D reconstructed scenes, generating actual 3D spatio-thermal models which store thermal values at 3D point level; (2) to generate expected 3D spatio-thermal models, building thermal performance is simulated through the numerical analysis based on the as-designed building information. The geometrical information extracted from the 3D building geometrical point clouds and the environmental boundary conditions acquired from EnergyPlus simulation using the local weather data are used for initialization; (3) finally, the actual and expected 3D spatio-thermal models are superimposed within a common 3D environment. The outcomes are EPAR environments which model and jointly visualize 3D actual and expected spatio-thermal models along with 3D-register thermal and digital imagery within the same environment. The following sections describe each step in detail (Ham and Golparvar-Fard 2013).

5.1.1 Extracting 3D geometrical information and initializing environmental conditions

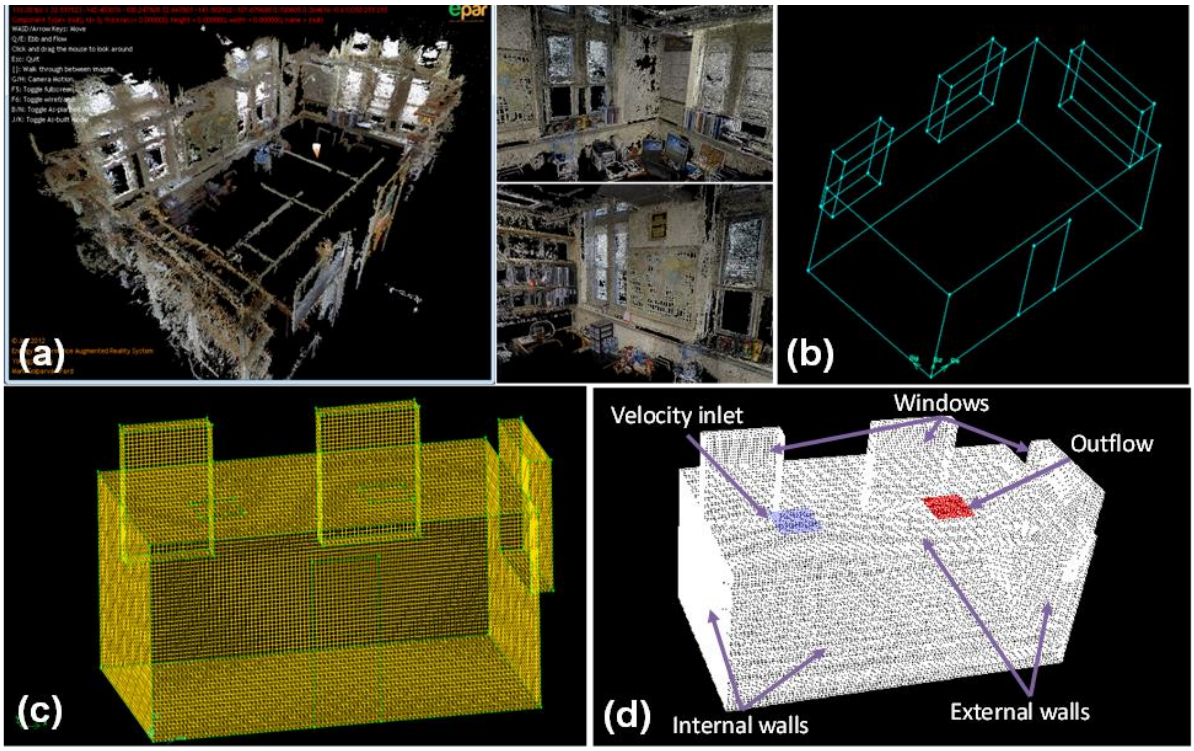

Figure 5.2 (a) Image-based 3D Building Point Clouds; (b) Extracting a 3D Wireframe Model; (c) Generating a Mesh Model; (d) Specifying Boundary Conditions

In order to generate 3D geometrical models of enclosed building spaces for energy simulation, the boundary points are extracted from generated 3D building geometrical point cloud in a supervised manner (Figure 5.2(a)). Using 3D coordinates of the selected boundary points (e.g., corners of

windows), a 3D virtual wireframe model is created (Figure 5.2(b)). The 3D wireframe models extracted from the 3D building geometrical point clouds are not in site coordinate system because the 3D image-based point cloud models are up-to-scale (i.e., their metric scale is unknown). In order to model the real as-built environments, the unit and scale factors of X, Y, and Z coordinates are calibrated based on the site coordinate system. The resulting calibrated domain is divided into a series of small discrete volumes using a mesh (Figure 5.2(c)), and then the energy conservation equations are imposed at each mesh element for iterative simulation process. Subsequently, the boundary types are specified per each building component (Figure 5.2(d)). In this step, the fluid is modeled as an ideal air, and the velocity inlet and outflow boundary types which represent HVAC systems are defined for the solution domain.

The primary environmental boundary conditions for initialization can be acquired from diverse building energy simulation tools. In this research, as a proof of concept, EnergyPlus simulation tool is used. EnergyPlus and CFD simulation provide complementary information required for evaluation of both energy consumption and thermal performances. Integrating these two tools by exchanging the complementary data can eliminate the principal modeling assumptions employed in the separate applications, and thus can provide more accurate predictions on building performance (Zhai et al. 2002). Given the large size of complementary data between EnergyPlus and CFD simulation, there are several possible coupling methods. According to (Zhai and Chen 2003; Zhai and Chen 2005), transferring indoor surface temperatures from simulation tool to CFD and returning indoor air temperature gradient and convective heat transfer coefficient from CFD back to the simulation tool is the most reliable and efficient coupling methods. This reliability and efficiency is in form of the convergence condition, computational time, and the simulation accuracy. Accordingly, the indoor surface temperatures resulted from the EnergyPlus simulation are fed into CFD analysis as initial environmental boundary conditions. To do that, building energy performance is first simulated using EnergyPlus based on the local weather data. Then, the surface temperature data of each building element at the time when digital and thermal images are captured are extracted. For exploring simulation results, ResultsViewer of OpenStudio 0.8.0 is used. This information is fed into the numerical analysis as environmental boundary conditions.

5.1.2 Expected 3D spatio-thermal simulation based on as-designed building information

Once the building geometrical and environmental boundary conditions are set, the expected building energy performance in form of 3D spatio-thermal model is simulated using CFD analysis. The simulation specific parameters (e.g., the numeric convergence error tolerances) are manually set by the user. Gambit 2.2.30 and Fluent 6.2.16 are used to set up the geometrical model and run the CFD analysis respectively. The air flow in a given space is assumed to be 3-dimentional. Although this requires more computational cost for solution convergence compared to 2-dimentional modeling, the results are more accurate since more realistic airflow characteristics such as airflow separation over building sharp edges can be considered (Asfour and Gadi 2007). Airflow in buildings is mainly considered to be turbulent, thus the turbulent model needs to be reasonably selected for solving the energy equations. For the turbulence modeling, the renormalization group (RNG) $k-\varepsilon$ model (Yakhot and Orszag 1986) is used. The RNG $k-\varepsilon$ model was experimentally demonstrated as a robust turbulent model that can provide the reliable results which closely match with the experimental measurements for assessing indoor thermal performance (Chen 1995; Evola and Popov 2006; Rohdin and Moshfegh 2007; Spengler and Chen 2000). Also, the segregated solver is used, which the energy equations are sequentially solved or segregated from each other. Based on the above condition, the thermal distribution of each zone is governed by the conservation laws of energy, mass, and momentum. Finally, by using the finite volume method, the simulation is iterated until the results are converged. Throughout this process, the convergences turbulence parameters (e.g., momentum and continuity of the viscous model) are monitored until the overall convergence conditions are met. In this work, the error tolerances for continuity, momentum, and turbulence dissipation rate are assumed to be 10^{-3}. The error acceptable for turbulent kinetic energy is set to 10^{-6}. After converging to a solution, the numerical analysis provides detailed information on the thermal distribution of the building space under inspection (Ham and Golparvar-Fard 2012).

5.1.3 EPAR modeling for integrated visualization of actual and expected performances

In order to calculate, analyze, and visualize the deviations between actual and expected building energy performances, the simulated performance model needs to be overlaid on the actual performance model. To do that, the graphics window displays of the resulting CFD model is converted to Virtual Reality Modeling Language (VRML) format. The VRML is a graphics

interchange format which enables export of 3D geometrical entities of the simulation results.

The integrated visualization step also involves transforming the 3D spatio-thermal models into the site coordinate system. This is a critical step since the scale of image-based point cloud models may be unknown. To find the absolute transformation, the closed-form solution of absolute orientation using unit quaternions is used (Horn 1987). Here, the transformation has 7 degrees of freedom. Thus, the 3D coordinates of a minimum of three control points are theoretically needed from both the 3D spatio-thermal model and the real-world. These points can either be pre-located before conducting the data collection, or simply be extracted from known dimensions such as dimensions of a given building space (e.g., height and width). Let *n* be the number of the matching points between the 3D spatio-thermal model and the actual site coordinate system. The two sets of points are denoted by r^i_{Model} and r^i_{Site} respectively, where *i* is a corresponding point ($i \in [1, n]$) and *Model* and *Site* represent the 3D spatio-thermal model and site coordinates respectively. The transformation between each corresponding pair is formulated as:

$$r^i_{Site} = sR\left(r^i_{Model}\right) + T \tag{7}$$

Where S is the uniform scaling factor, T is the translational offset, and $R\left(r^i_{Model}\right)$ is the rotation of the 3D spatio-thermal model. To minimize user selection errors for finding correspondence between 3D spatio-thermal models and the real-world coordinate system, the estimation of the accurate registration of point coordinates from one system into another is approximated with the minimization of the sum of squared residual errors between these *n* corresponding pairs. This further helps minimize the errors caused by user selection or poor measurements of the actual scene. Hence, the minimization of the errors can be formulated using Equation (8). This formulation results in the 3D spatio-thermal model to be transformed into the site coordinates and also measures the registration accuracy.

$$\sum_{1}^{n} \left\| e^i \right\|^2 = \sum_{1}^{n} \left\| r^i_{Site} - sR\left(r^i_{Model}\right) - T \right\|^2 \tag{8}$$

Aligning the actual and expected performance models requires geometric transformations

between the two models (e.g., scaling, rotation, and translation) to be known. Since both 3D spatio-thermal models and the 3D building geometry for CFD analysis are calibrated based on the site coordinate system, two models have the same coordinate systems. Consequently, the two models can be automatically superimposed. The digital and thermal images are also automatically 3D-registered in the EPAR models by using the digital camera location and orientation calculated from the SfM and the relative pose of the thermal camera lens with respect to the digital camera lens respectively. The final outcomes are EPAR models which jointly visualize actual and expected 3D spatio-thermal models, along with the 3D geo-registered thermal and digital images. For the integrated visualization, a new visualization tool is created and prototyped. To do that, the following data structure is used:

- $(P_D^1, P_D^2, \ldots, P_D^n)$: a set of 3D points where $P_D^i = \langle X_D^i, RGB_D^i \rangle$ encapsulates the 3D location (X_D^i) and the color (RGB_D^i) of each point averaged from the colors of all digital cameras that observe it
- $(M_D^1, M_D^2, \ldots, M_D^n)$: a set of digital cameras where $M_D^i = K_D^i \left[R_D^i | T_D^i\right]$ represents the digital camera projection matrix for camera *i*
- $(P_T^1, P_T^2, \ldots, P_T^n)$: a set of 3D thermal points where $P_T^i = \langle X_T^i, RGB_T^i \rangle$ encapsulating the 3D location (X_T^i) and the color (RGB_T^i) of each 3D thermal point. Here, the color is corresponding to the normalized color spectrum
- $(M_T^1, M_T^2, \ldots, M_T^n)$: a set of digital cameras where $M_T^i = K_T^i \left[R_T^i | T_T^i\right]$ represents the thermal camera projection matrix for camera *i*
- A mapping relationship between the points and the cameras that observe each points
- The *x* and *y* coordinates of the points in local coordinate system of each image
- The number of feature points and cameras which observe the points

In the EPAR visualization interface, the digital and thermal cameras are rendered in form of pyramid-shape camera frusta. Once a camera is visited in the 3D reconstructed scene, it is automatically texture-mapped with the corresponding digital and thermal images. Here, the user can either select to view the digital or thermal images captured from the particular camera location. The user location can also be preserved, while the viewpoint is changing to jointly visualize and

study the 3D point cloud models along with the registered images. Ultimately, the user can navigate the actual and expected 3D thermal profiles in a given building space and further analyze performance deviations at the level of 3D point.

5.2 Identification and Visualization of Potential Performance Problems based on Performance Deviations

Given generated EPAR models, the next goal is to create and validate a new model-based method that (1) can automatically calculate performance deviations and (2) infer and visualize potential energy problems with the associated digital and thermal images in 3D. Figure 5.3 shows an overview of the proposed method.

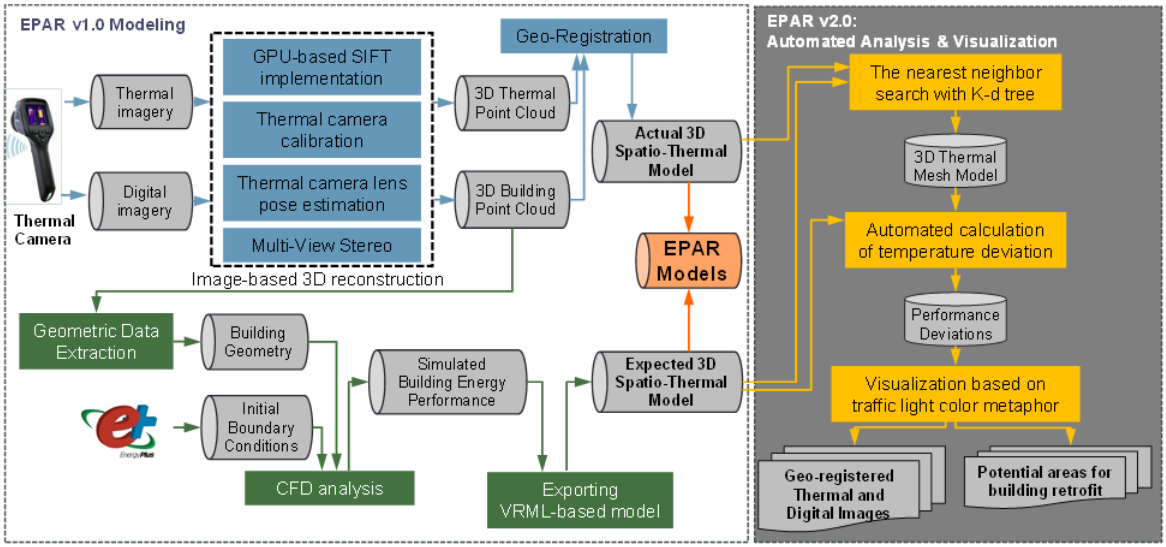

Figure 5.3 Overview of the Data and Process in the Performance Deviation Analysis Method

The proposed method for EPARv2.0 builds on the EPAR modeling method (Section 5.1) and leverages two new algorithms:

- EPAR (Section 5.1): using an unordered collection of thermal and digital images captured from the buildings under inspection, 3D building geometrical and thermal point cloud models are automatically generated and integrated to form an actual 3D spatio-thermal model. Then, the building energy performance is simulated through the numerical analysis based on as-designed building information, generating expected 3D spatio-thermal models.

Finally, the two models are superimposed in a common 3D environment, forming EPAR models along with 3D-registered images;

- EPARv2.0: Two new algorithms for 3D thermal mesh modeling based on *k-d* tree structures and the nearest neighbor searching method are developed for automated calculation of performance deviations. Based on the temperature deviations and a threshold, potential building performance problems are inferred and visualized based on a metaphor of traffic light colors in EPAR models. The following sections describe each step in detail (Golparvar-Fard and Ham 2014).

5.2.1 3D mesh modeling of building thermal profiles

In order to calculate deviations between actual and expected thermal performance in EPAR models, the measured and simulated indoor surface temperatures are compared at the level of 3D point. To that end, the following data sets are defined:

- $(P_A^1, P_A^2, \ldots, P_A^j)$ denote a set of actual 3D thermal points. These points are the outcomes of the image-based 3D thermal modeling method. $P_A^i =< X_A^i, RGB_A^i >$ encapsulates the 3D location (X_A^i) and color value (RGB_A^i) of each 3D point, and j is the number of points in the actual 3D thermal point cloud model. Each RGB color value corresponds to a normalized temperature scale, and in turn represents an absolute thermal value.
- $(P_S^1, P_S^2, \ldots, P_S^K)$ denote a set of simulated 3D thermal points resulted from the numerical analysis. $P_S^i =< X_S^i, RGB_S^i >$ encapsulates 3D location (X_S^i) and color values (RGB_S^i) of each 3D point, and k is the number of vertex in the VRML-based CFD model. Here, each RGB color value corresponds to an absolute thermal value.

In EPAR models in form of point clouds, the user need to manually find the closest pairs between the actual and expected 3D thermal points for performance comparison. Through experimental observations, it was found that the manual extraction and comparison between the two 3D point cloud models is not trivial and prone to error. In particular, the actual 3D thermal point cloud resulted from the image-based 3D reconstruction typically includes large numbers of points that do not belong to the building geometry, which further makes the comparison challenging. To overcome the challenge in direct application of point cloud-based EPAR models

for performance comparison, a new method for generating 3D mesh models of the actual thermal performance is proposed to improve the model completeness by leveraging the VRML-based CFD models as a geometrical baseline. The proposed approach for 3D mesh modeling of the actual thermal performance is to first find the closest point P_A^i for each P_S^i according to the distance between two points, and then convert the RGB color values of P_S^i (RGB_S^i) into the RGB color values of the corresponding P_A^i (RGB_A^i). Ultimately, a new 3D point data set $<P_M^1, P_M^2, \ldots, P_M^k>$ is generated which will be used for 3D thermal mesh modeling. Here, *k* is the number of points in the simulated 3D thermal model, and $P_M^i =< X_M^i, RGB_M^i >$ encapsulates the 3D location (X_M^i) and color value (RGB_M^i) of each 3D point. These points are subsequently used to generate the polygons that are required for the mesh modeling process. Figure 5.4 summarizes the proposed 3D thermal mesh modeling algorithm.

Input: Actual 3D thermal points

$$Q_A = \{P_A^i | \forall i \in (1,2, \ldots j), P_A^i =< X_A^i, RGB_A^i >\}$$

Simulated 3D thermal points

$$Q_S = \{P_S^i | \forall i \in (1,2, \ldots k), P_S^i =< X_S^i, RGB_S^i >\}$$

Output: $Q_M = \{P_M^i | \forall i \in (1,2, \ldots k), P_M^i =< X_M^i, RGB_M^i >\}$ for mesh modeling

```
1   for i=1:k
2     for n=1:j
3       calculate D = sqrt((X_A^n − X_S^i)^2)
4         if D is minimum
5           return RGB_A^n
6         end if
7       RGB_M^i → RGB_A^n
8       X_M^i → X_S^i
9     end for
10  end for
11  return Q_M = {P_M^i | ∀i ∈ (1,2, ... k), P_M^i =< X_M^i, RGB_M^i >}
```

Figure 5.4 Algorithm for 3D Mesh Modeling of Actual Thermal Performance

To find the closest points for pairing, the brute-force method was first used to calculate the distance from the query point to every other point in the corresponding dataset. Next, all the distances are sorted in an ascending order, and the pair which yields the shortest distance among all neighboring points is selected. Given a significant number of points in the generated point cloud, such naïve method requires high computational cost since it calculates the distance for every

possible configuration. Instead, to minimize computational time required for finding the nearest neighbor to each query point P_S^i, the simulated thermal points P_S^i are mapped into a *k-d* tree structure. The *k-d* tree algorithm is a computational approach for space-partitioning of data structure to organize points in a k-dimensional space (de Berg et al. 2008). The binary trees are used to store spatial data in a multi-dimensional space. The *k-d* trees recursively divide the set of points into subsets with half of the points of the parent node by a line perpendicular to one of the dimensions. The resulting point sets are partitioned into equal halves using the hyperplane of a different dimension. Partitioning process stops once each point locates its own leaf cell. Ultimately, the *k-d* trees hierarchically decompose overall space into a series of cells so that no cell contains too many points. The nearest neighbor search with the *k-d* tree algorithm can be done efficiently by using the decomposing properties of the tree. This eliminates a large portion of the overall search space, allowing significant improvement in the computational time. First, each tree including the root node and the sub-domains are examined. A multi-dimensional query is composed of several 1-dimensional sub-queries. Starting from the root node, the query algorithm is recursively performed to the entire branch. Once the query algorithm reaches a leaf node, the distance to the node point is stored as the current best nearest distance. Then, the query algorithm looks into each parent node, identifying the possibility of other domain including a closer point than the current best. To do that, the query algorithm identifies whether the splitting hyperplane intersects with a hypersphere around the search point. As the hyperplanes are axis-aligned, the distance between the splitting coordinate of the search point and the current node is compared with the distance from the search point to the current best. If the hyperplane intersects the hypersphere, the query algorithm is implemented to find the closer points in the other branch of the tree, following the same recursive process. If the hypersphere does not cross the splitting plane, the entire branch is eliminated. All these processes are repeatedly done until all domains are either searched or discarded. Once the algorithm fails to find a closer point P_A^i given a query point P_S^i, the searching process is terminated and yields the nearest neighbor P_A^i. Lastly, the RGB color value of the resulting nearest neighbor P_A^i is fed into the proposed mesh modeling algorithm.

5.2.2 Calculating actual and simulated temperature values and visualizing performance deviations

The actual and simulated temperature values (T_A^i and T_S^i respectively) are calculated from the RGB

color values of each vertex in EPAR models. First, the normalized temperature scales of both thermal images and CFD models (TS and CS respectively) are converted into a fixed range of RGB color values (RGB_{TS} and RGB_{CS} respectively). As long as a consistent color spectrum is used for visualization, this process does not need to be repeated for different data collections. Then, given RGB_A^i and RGB_S^i, the matching RGB color values in RGB_{TS} and RGB_{CS} are searched, and then T_A^i and T_S^i for point i are calculated by using Equations 9 and 10 respectively:

$$T_A^i = TS_{min} + (RGB_{TS}^i - 1) \times \frac{TS_{max} - TS_{min}}{Level_{TS} - 1} \quad (9)$$

$$T_S^i = CS_{min} + (RGB_{CS}^i - 1) \times \frac{CS_{max} - CS_{min}}{Level_{CS} - 1} \quad (10)$$

Here, TS_{max} and TS_{min} are the maximum and minimum values of temperature scale used in building thermography, and similarly CS_{max} and CS_{min} are the maximum and minimum values of temperature scale used in the VRML-based CFD model. $Level_{TS}$ and $Level_{CS}$ indicate the range of each RGB color value chart converted from temperature scales used for building thermography and VRML-based CFD model respectively.

The final step is to compute the deviations of two models and visualize them in EPAR models using a metaphor based on traffic light colors. Since the geometry of VRML-based CFD models was used for 3D mesh modeling of actual thermal performances as a geometrical baseline, 3D actual and expected thermal mesh models share the same coordinate system. Thus, by computing the difference between T_A^i and T_S^i for each 3D vertex in EPAR models, indoor surface thermal performance deviations can be simply calculated. Small deviations between actual measurements and simulation results are typically related to the inherent uncertainty in measurement accuracy of a thermal camera and the numerical analysis, and thus can be expected. Thus, the user needs to set a threshold for inferring the presence of potential performance problems in building environments. Based on the threshold, the areas with or without potential performance problems are color-coded with red and green colors respectively in EPAR models.

CHAPTER 6. MEASURING ACTUAL THERMAL RESISTANCE AND DETECTING CONDENSATION PROBLEMS

Given a collection of digital and thermal image pairs captured using a thermal camera from building environments under inspection, this chapter aims to create and validate a new non-destructive method for quantitative assessment of the as-is building condition. The hypothesis is that the quality of building condition assessment process can be improved with the method that can utilize building thermography to 1) explore the actual heat transfer conditions of building assemblies at the level of 3D point; 2) detect condensation problems, and 3) visualize the outcomes in an intuitive 3D form for better communication with building practitioners. The overall workflow is illustrated in Figure 6.1.

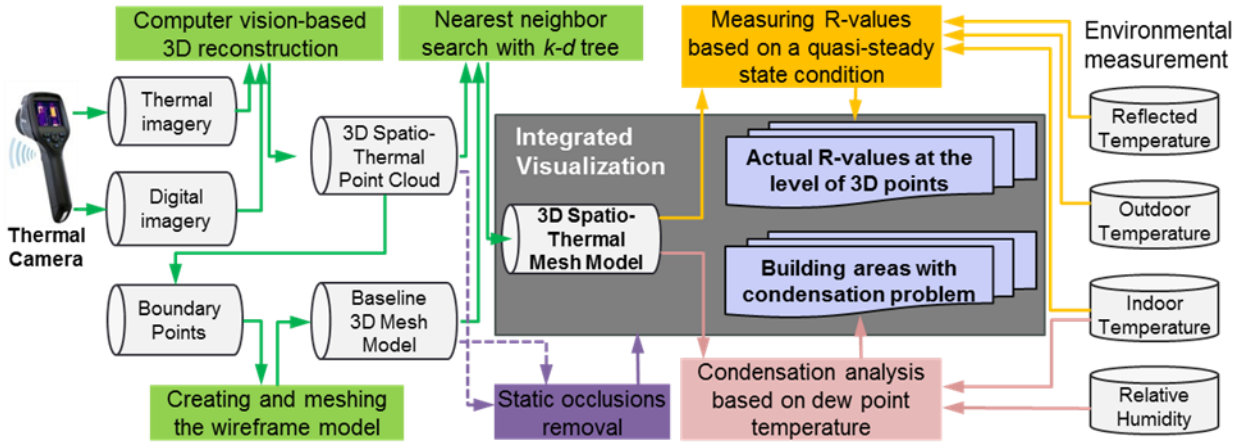

Figure 6.1 Overview of the Data and Process in the 3D Visualization Method for Thermography-based Building Condition Assessment

The proposed method consists of two parts: (1) 3D spatio-thermal mesh modeling of building environments (Section 5): By using digital and thermal images collected from the building under inspection, both 3D building geometrical and thermal point clouds are generated using an image-based 3D reconstruction algorithm. The resulting 3D thermal point clouds are then superimposed with the 3D reconstructed scenes, forming 3D spatio-thermal point cloud models. Next, for the best representation of thermal performance, the model completeness is improved through mesh modeling based on a geometrical baseline model. The outcomes are 3D spatio-thermal mesh models which contain surface temperature readings at the level of vertex in 3D mesh

models.

(2) Building condition assessment based on 3D thermal profiles of building surfaces and integrated 3D visualization with the associated building geometrical characteristics: Based on 3D thermal profiles in 3D spatio-thermal mesh models and measuring the reflected apparent temperature from a crumpled aluminum foil placed on a building surface under inspection, the actual thermal resistances are calculated at the level of point in 3D. In addition, by calculating the dew point temperature, building surface areas that suffer from condensation problems are detected. Finally, the distribution of the actual thermal resistances, the detected building areas with condensation problems, and the corresponding geometrical characteristics are jointly visualized in a common 3D environment. The following sections describe the environmental assumptions and underlying methods in detail (Ham and Golparvar-Fard 2014).

6.1. Environmental Assumptions

The proposed method is based on the following environmental assumptions:

1) the indoor building environment is assumed to have a quasi-steady-state condition of heat transfer during the thermographic inspection process. This is consistent with all recent works on non-destructive measurement of actual heat transfer condition of building assemblies using thermography (Albatici and Tonelli 2010; Dall'O' et al. 2013; Fokaides and Kalogirou 2011; Madding 2008). For achieving a quasi-steady-state condition of heat transfer, building envelopes under inspection were not exposed to direct solar radiations and wind loadings as the inspections were conducted before sunrise on a cloudy and non-windy day (i.e., around 6-7am). This minimizes the influence of the convective heat loss and the surface temperature rise on building envelopes. By doing so, the possible increase in building surface temperatures which can be caused by the release of the absorbed solar energy throughout a day can be minimized as well.

2) it is further assumed that the heat transfer between the surfaces under inspection and the thermal camera lens is due to thermal convection and radiation which is also consistent with prior works (Fokaides and Kalogirou 2011; Madding 2008). In addition, building interior spaces under inspection are heated for few hours prior to thermographic inspections, which allows energy auditors to clearly capture the as-is heat transfer conditions through building façades during a winter season.

6.2 Building Condition Assessment based on 3D Spatio-Thermal Models

6.2.1 Reconstructing 3D thermal profiles of building environments using 2D thermography

The first step to assess building conditions at the level of 3D point is to model the actual thermal profiles of building environments under inspection in 3D. The proposed method for generating 3D spatio-thermal models of building environments builds upon the methods in (Ham and Golparvar-Fard 2013) and (Golparvar-Fard and Ham 2014), which introduced in Section 4 and 5. First, both thermal and digital images of the building under inspection are collected by practitioners using a consumer-level IR camera. Then, the 3D geometrical point cloud of the building is automatically generated by using the collected digital images. Here, an image-based 3D reconstruction method is used, which consists of Graphic Processing Unit (GPU)-based Structure-from-Motion (SfM) and Multi-View Stereo (MVS) algorithms. The next step is 3D thermal modeling using the collected thermal images. Unlike digital images, thermal images are typically featureless in computer vision terms and have low spatial resolutions. The lack of distinct visual features impede the direct application of the same image-based 3D modeling algorithm used on digital images for 3D building geometrical modeling purposes. Instead, through a one-time process, the thermal camera is calibrated, and the relative pose of the thermal camera lens with respect to the built-in digital camera lens is estimated. Based on the intrinsic thermal camera parameters, the extrinsic digital camera parameters, and the estimated relative pose, a dense 3D thermal point cloud model is generated using the dense reconstruction algorithm. The resulting 3D thermal and geometrical point cloud models are superimposed, forming 3D spatio-thermal point cloud models.

The resulting point cloud models would be incomplete and include artifacts that are not relevant to the building geometry. The point cloud models are converted into 3D thermal mesh models by using *k-d* tree structure and the nearest neighborhood searching algorithm. In this process, a geometrical baseline mesh model is used as the basis for the transformation. Here, to form the baseline model, the boundary points were extracted from the building geometrical point cloud in a supervised manner. This process improves the completeness of 3D thermal models by extrapolating thermal performance for those building areas that are sparsely reconstructed. For building areas that are densely reconstructed, this process will sub-sample 3D thermal points, which reduce the computational cost for calculating thermal resistance at the later stage. The outcome of this process is the 3D spatio-thermal mesh model in which each vertex is associated with a temperature reading averaged from all thermal images that have observed the vertex during

thermographic inspection.

Here, to better deal with static occlusions in building environments, a geometrical threshold is used to identify those thermal points that have a certain distance from the geometrical baseline mesh. If the nearest thermal point is too far from the vertices in the baseline mesh (i.e., above the threshold), it is most likely that the thermal points belong to objects around the wall but not the building geometry itself. This threshold is set based on the point cloud-to-mesh registration error.

6.2.2 Measuring actual R-values at the level of point in 3D

The R-value given in the SI unit (m^2K/W) describes the thermal resistance of building assemblies (i.e., the reciprocal of the amount of heat energy transmission per 1 second through a surface of $1m^2$ in a steady-state condition, if indoor and outdoor temperatures differ by 1 K). Thus, thermal resistance (R) with the overall heat transfer rate (dQ/dt) through a building surface with the area of (A) and a temperature difference of ΔT between inside and outside of the building can be described by using the following equation:

$$\mathrm{R} = \frac{A \times \Delta T}{dQ/dt} \tag{11}$$

According to the environmental assumptions presented in Section 6.1, the overall heat transfer of building environments (Q) can be described by the combination of thermal convection and radiation. This research focuses on measuring actual thermal resistance of building envelopes while taking into account possible building occlusions. First, the amount of heat transfer caused by thermal convection between the interior surface of building environments and the indoor air is calculated by using the following equation:

$$\mathrm{Q_{Convective}} = \alpha_{\mathrm{convective}} \times \mathrm{A} \times \left|\mathrm{T_{inside,air}} - \mathrm{T_{inside,wall}}\right| \tag{12}$$

Where $\alpha_{convective}$ is the convective heat transfer coefficient which is a function of the airflow (e.g., laminar or turbulent) and the temperature deviations between building surface and indoor air. Typical convective heat transfer coefficients of indoor building environments are within

the range of 2-8 W/m^2K). In this research, the convective heat transfer coefficients are adopted based on the approach presented in (Dall'O' et al. 2013). As part of data collection, the inside and outside air temperatures, $T_{inside,air}$ and $T_{outside,air}$, are also measured by using a thermometer.

Then, the heat transfer between the interior surface of building environment and the surroundings caused by thermal radiation is calculated by using the following equation:

$$Q_{Radiation} = \varepsilon \times \sigma \times A \times \left| T^4_{inside,wall} - T^4_{inside,reflected} \right| \quad (13)$$

Where ε is thermal emissivity and σ is Stefan-Boltzmann constant (5.67×10^{-8} $^{W}/_{m^2K^4}$). The thermal emissivity for plaster is adopted from the emissivity measurement in (Mikron Instrument Company 2012; Singham 1962). It is noted that depending on the temperature at the time of measurement, thermal emissivity of building materials can vary. In experiments, the surface temperature measurement was within the range reported in (Mikron Instrument Company 2012; Singham 1962), and thus the choices for these values are acceptable. To calculate the heat transfer due to thermal radiation, the reflected temperature, $T_{inside,reflected}$ needs to be measured as well. This temperature represents the condition of the indoor building environment which is considered as large thermal reservoirs without temperature variations. To do so, a small crumpled aluminum foil is placed on the inspection areas prior to the thermographic inspection (Figure 6.2). Since the crumpled aluminum foil has low emissivity and high reflectivity, the reflected apparent temperature can be robustly measured from the crumpled foil (FLIR system 2010). Previous studies (Fokaides and Kalogirou 2011; Madding 2008) experimentally demonstrated that the most sensitive factor on accurate the R-value measurement using building thermography is the difference between surface and reflected apparent temperatures. Especially, in the case of well-insulated building assemblies, this difference can be very small. Thus, measuring the accurate reflected apparent temperature is critical for reliable R-value measurement. Instead of extracting a single temperature from the crumpled foil or averaging temperatures of a few target points used in (Fokaides and Kalogirou 2011; Madding 2008), the average temperature of the crumpled foil is calculated from all pixels that represents the foil surface. To do so, the RGB color values of these pixels from the thermal image (Figure 6.2) were converted into the corresponding absolute temperature values based on a normalized temperature spectrum and then

were averaged for the associated pixels.

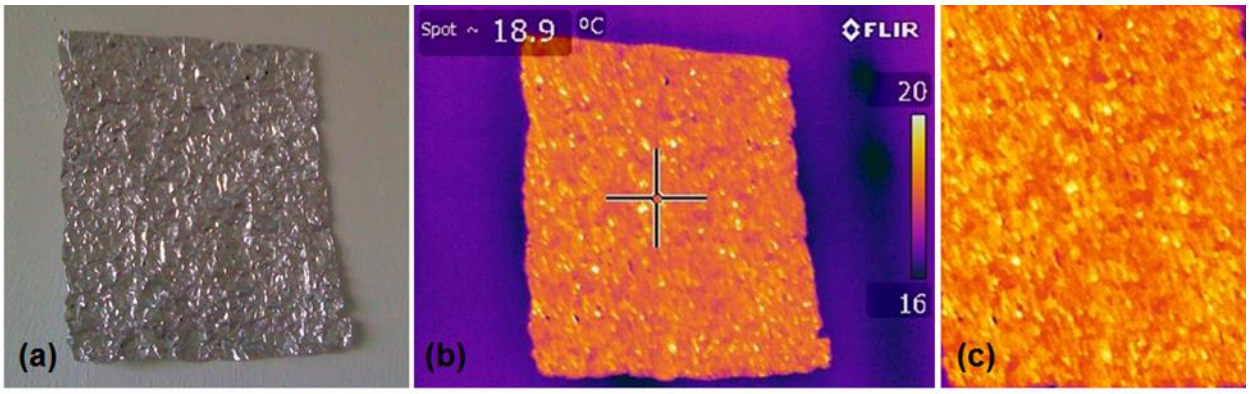

Figure 6.2 Measuring Reflected Temperature: (a) Crumpled Aluminum Foil Located on the Inspection Surface; (b) Thermal Image Simultaneously Captured from the Same Viewpoint; (c) Temperature Readings on the Crumpled Aluminum Foil Surface

It is assumed that all interior surfaces of the building environment under inspection have the same reflective temperatures, which is experimentally validated in (Fokaides and Kalogirou 2011). Finally, by combining the Equation (11), (12), and (13), the thermal resistance can be described by using the following equation:

$$R = \frac{\left|T_{inside,air} - T_{outside,air}\right|}{\alpha_{con} \times \left|T_{inside,air} - T_{inside,wall}\right| + \varepsilon \times \sigma \times \left|T^4_{inside,wall} - T^4_{inside,reflected}\right|} \quad (14)$$

Within the resulting 3D spatio-thermal mesh models, $T_{inside,wall}$ can be queried from each 3D vertex in 3D mesh models. It is noted that the thermal points may belong to objects on or around building assemblies and not the associated building element. Thus, when searching for the nearest thermal points with respect to each vertex in the geometrical baseline mesh, a geometrical threshold is used, which is obtained from the registration error between the point cloud and the mesh models. Thus, those thermal points belonging to non-relevant objects are not considered for calculating the thermal resistances of building assemblies. Once the actual relevant-to-building-geometry thermal points ($T_{inside,wall}$) are queried from 3D spatio-thermal mesh models, the actual thermal resistances of the building assemblies under inspection can be calculated using Equation (14) at the level of point in 3D while taking into account building occlusions.

6.2.3 Detecting building condensation problems in 3D

Building condensation is due to the fact that the air at a given temperature can only accommodate a certain amount of water. This is typically characterized by the relative humidity and the maximum absolute humidity. The absolute humidity is a measure of the amount of the water content in the air, which itself is a function of the air temperature. The relative humidity is a measure of the percentage of the actual water content in the air with respect to the maximum absolute humidity (i.e., the amount of maximum possible water content at a given air temperature). When the air contains more water content than the maximum possible amount at a given air temperature, the amount of the extra water vapor will condense on the surrounding surfaces. Hence, the dew point temperature (T_D) is a function of the relative humidity (f) and indoor temperature ($T_{inside,air}$) and thus can be represented with the following equation (Wanielista et al. 1997):

$$\mathrm{T_D} = \left(\frac{\mathrm{f}}{100}\right)^{1/8}\left(112 + 0.9\mathrm{T_{inside,air}}\right) + 0.1\mathrm{T_{inside,air}} - 112 \quad (15)$$

The indoor temperature and the relative humidity are measured with the use of a thermo-hygrometer as part of the thermographic inspection. In this research, the building surface temperature ($T_{inside,wall}$) can be directly queried at the level of 3D vertex from the generated 3D spatio-thermal mesh models. Thus, the building surface areas that are likely to suffer from condensation problems are also detected by comparing $T_{inside,wall}$ and T_D at the level of point and localized in 3D.

6.2.4 Visualizing the as-is building condition in 3D while taking into account building occlusions

In order to segment non-relevant objects from the 3D reconstructed scene for minimizing the impact of building occlusions, the idea is that if a 3D thermal point in 3D spatio-thermal model is physically far from the geometrical baseline mesh, it is most likely that the point belongs to objects around walls but not the building geometry. Here, the geometrical threshold is based on the point cloud-to-mesh registration error. To do that, the registration accuracy of the 3D spatio-thermal point cloud with the geometrical baseline mesh in the site coordinate system is examined. Mapping

thermal point clouds to a geometrical baseline mesh involves transforming the 3D spatio-thermal model into the site coordinate system. To determine this transformation, the closed-form solution using unit quaternions is used (Horn 1987). The transformation from the 3D spatio-thermal model into the real-world has 7 degrees of freedom (i.e., 1 for scaling + 3 for translation + 3 for rotation), and thus requires a minimum of three matching control points between the 3D spatio-thermal model and the real-world coordinate system (Ham and Golparvar-Fard 2013). These control points, $P^i_{Thermal}$ and P^i_{Site}, can be extracted from the known dimensions in the building environments. This is solved by minimizing the sum of squared residual errors of the Euclidean transformation for *n* control points by using the following equation:

$$\sum_{1}^{n} \left\| e^i \right\|^2 = \sum_{1}^{n} \left\| P^i_{Site} - sR\left(P^i_{Thermal}\right) - T \right\|^2 \tag{16}$$

Where, s, T, and R($P^i_{Thermal}$) indicate the scaling factor, translational offset, and rotation of 3D spatio-thermal models respectively. The resulting registration error (*e*) is then used as a geometrical distance threshold for detecting thermal points that are likely to represent static occlusions in building environments. Ultimately, among $T_{inside,wall}$ that can be queried from each 3D vertex in 3D spatio-thermal mesh models, those thermal points belonging to non-relevant objects (i.e., above the threshold (e)) are not used for calculating the thermal resistances of building assemblies and detecting condensation problems. Once the relevant-to-building-geometry thermal points are queried from 3D spatio-thermal mesh models, the actual R-values of the building assemblies under inspection are calculated by using Equation (14), and the building areas associated with condensation issues are detected by using Equation (15).

Then, for integrated 3D visualization, the measured R-values and the comparison of $T_{inside,wall}$ and T_D at the level of 3D point are converted into the corresponding RGB color value. The proposed visualization platform provides several navigation modes such as a 3D free-flight navigation to efficiently visualize performance metrics and potential issues with the related building views. Similar to most engineering 3D viewers, when a camera is visited in the 3D reconstructed scene, users can pan, tilt, and zoom-in & out for exploring the particular building areas in form of mesh. For integrated visualization of the distribution of the actual R-value, the

detected building areas with condensation issues, and the related geometrical and thermal characteristics, the proposed visualization platform leverages the following data structures:

(1) $(P_1^e, P_2^e, \dots, P_n^e)$: a set of relevant-to-building geometry 3D vertices in a mesh where $P_i^e = \langle X_i^e, Y_i^e, Z_i^e, RGB_i^{R-value}, RGB_i^{Condensation}, RGB_i^{SurfaceTemperature} \rangle$ encapsulates the 3D location (X_i^e, Y_i^e, Z_i^e), the color value $(RGB_i^{R-value})$ of each vertex which corresponds to the measured thermal resistances according to the given color spectrum, the color value $(RGB_i^{Condensation})$ of each vertex which is a metaphor based on traffic light colors to represent problematic (i.e., with condensation issues) and non-problematic areas using red and green colors respectively, and finally the color value $(RGB_i^{SurfaceTemperature})$ of each vertex associated with a temperature reading averaged from all thermal images that have observed the vertex

(2) $(P_1^g, P_2^g, \dots, P_m^g)$: a set of 3D points where $P_i^g = \langle X_i^g, Y_i^g, Z_i^g, RGB_i^{Geometry} \rangle$ encapsulates the 3D location (X_i^g, Y_i^g, Z_i^g) and the color $(RGB_i^{Geometry})$ of each point in 3D building geometrical point cloud, which is the average from the colors in all digital images that have observed the point

(3) $(C_1^T, C_2^T, \dots, C_l^T)$: a set of thermal cameras representing the thermal camera projection matrix based on the relative pose of the thermal camera with respect to the built-in digital camera

(4) $(C_1^D, C_2^D, \dots, C_l^D)$: a set of built-in digital cameras representing the digital camera projection matrix for each camera registered in the 3D reconstructed scene

(5) A set of vertices that form each mesh face

(6) The number of vertices and faces in a mesh

(7) The number of feature points and cameras that observe the points

(8) Mapping relationship between points and cameras that observe the points

CHAPTER 7. 3D THERMOGRAPHY-BASED METHOD FOR COST ANALYSIS OF ENERGY EFFICIENCY BUILDING ENVELOPE RETROFITS

In this chapter, a new 3D thermography-based method for cost analysis of building insulation retrofits is presented. The method leverages the as-is thermal resistance measurements at the level of 3D point and building areas associated with potential performance problems detected in EPAR models. Figure 7.1 shows the proposed workflow.

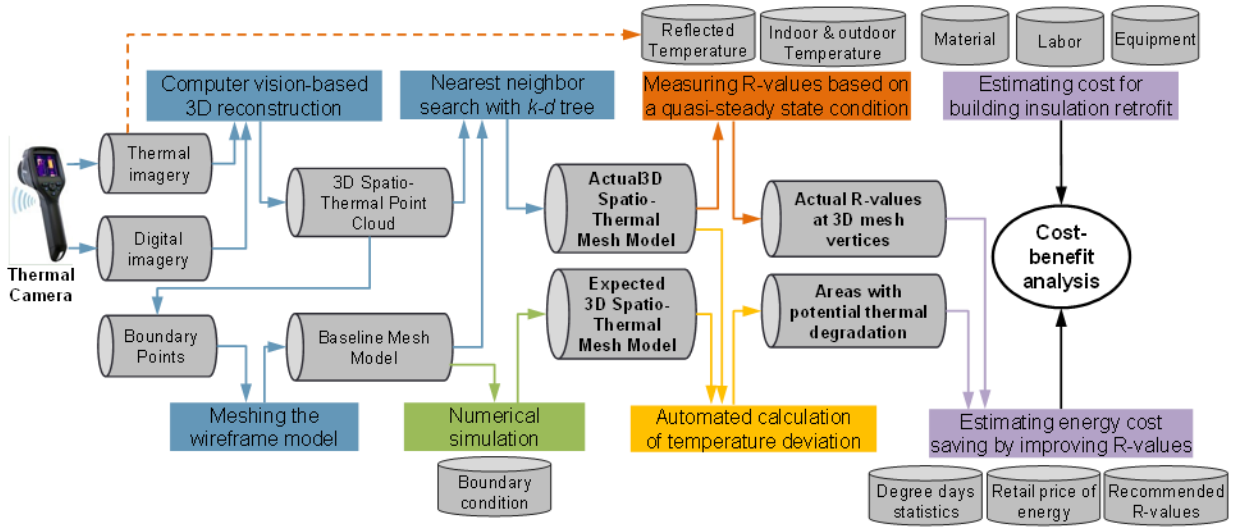

Figure 7.1 Overview of the Data and Process in the Thermography-based Method for Cost Analysis of Building Insulation Retrofit

It is hypothesized that if the sources of energy loss are reliably retrofitted, either at small scale by adding insulations or at large by replacing the degraded ones, homeowners can save energy costs associated with unnecessary heat transfers through their existing building envelopes. It is further hypothesized that insulation retrofits will result in their expected energy performance improvements. Based on these hypotheses, the proposed method has the following workflow: (1) Through thermographic inspection, practitioners collect digital and thermal images from building surfaces under inspection. With these images, EPAR models are developed; (2) The proposed method identifies the potential sources of energy loss based on performance deviations in the EPAR models and calculates the as-is heat transfer condition of the associated building assemblies; (3) The amount of heat transfer that can be saved by improving the as-is thermal resistances of the defective areas to the recommended level is estimated, and the equivalent energy cost is

calculated based on the retail energy price of electricity or natural gas; and finally (4) The proposed method estimates the cost of retrofitting potential thermal defects and balances it against the expected monetary benefits. The following describes the underlying algorithms in detail (Ham and Golparvar-Fard 2013; Ham and Golparvar-Fard 2014).

To convert building thermography into the energy cost associated with thermal performance problems, it is first assumed that the building environment has a quasi-steady state heat transfer condition during the thermographic inspection process, similar to (Fokaides and Kalogirou 2011; Madding 2008). In a steady state condition, the unit R-value ($1m^2K/W$) indicates the reciprocal of the amount of heat transfer through a surface of $1m^2$ per 1 second when the air-to-air temperature difference across the envelope is 1K. Hence, with a temperature difference (ΔT), the overall heat transfer rate (dQ/dt) for a building surface (A) with thermal resistance (R) is described as:

$$\frac{dQ}{dt} = \frac{1}{R} \times A \times \Delta T \tag{17}$$

Thus, the amount of unnecessary heat transfer through building areas associated potential thermal defects ($Q_{Loss\ or\ Gain}$) can be calculated using Equation (18):

$$Q_{Loss\ or\ Gain} = \frac{1}{R_{Actual}} \times A_P \times \left|T_{inside} - T_{outside}\right| \times t \tag{18}$$

where A_P: building areas associated with potential thermal defects; R_{Actual}: actual thermal resistances of the associated building assemblies, and $\left|T_{inside} - T_{outside}\right| \times t$: temperature difference between inside and outside of the building over a given time period. In the following sections, how each of these parameters can be calculated in EPAR models is described.

7.1 Calculating Building Areas Associated with Potential Thermal Performance Problems

For quantifying the unnecessary heat transfer through building envelopes, the sources of energy loss first need to be localized, and their associated building areas (A_P) are then calculated.

7.1.1 Identifying potential performance problems in building environments

For identifying potential thermal performance problems attributed to unnecessary heat transfer, the EPAR-based method (Ham and Golparvar-Fard 2013) leverages two sources of information: 1) unordered collections of digital and thermal images: these images are collected using a hand-held thermal camera which has a built-in digital camera. Through an image-based 3D reconstruction, the actual thermal profiles of building surfaces under inspection are modeled in form of 3D spatio-thermal point cloud ; and 2) Virtual Reality Modeling Language (VRML) based-CFD models: the results of the numerical analysis of building environments provide the expected thermal profiles of buildings under the as-designed building information. The actual and expected thermal performance models are integrated in a common 3D environment, generating EPAR models in the form of point cloud. Here, by using *k-d* tree structure and the nearest neighbor searching algorithm (de Berg et al. 2008), the 3D thermal point cloud is mapped into the baseline mesh geometry of VRML-based CFD models, which generate 3D thermal mesh models of building environments under inspection. By comparing the measured and simulated surface temperature data in the EPAR environments, performance deviations are calculated at the level of 3D vertex. Here, a threshold is used to infer the presence of potential performance problems. Then, potential thermal performance problems where thermal performance deviations are above the predefined threshold are identified and visualized in EPAR models using a metaphor based on traffic light colors.

7.1.2 Calculating building areas associated with potential thermal performance problems

The surface areas associated with potential thermal performance problems are calculated from the EPAR models in form of triangle-mesh faces. For each face, the 3D coordinates of the associated three vertices are queried, and then the associated area is calculated by using the cross product of two corresponding vectors that form the face. Figure 7.2 summarizes the overall algorithm for identifying potential thermal performance problems and calculating the associated building surface areas (A_P).

Inputs: Measurement $Q_A = \{P_A^i | \forall i \in (1,2,\dots j), P_A^i =< X_A^i, Y_A^i, Z_A^i, RGB_A^i >\}$
Simulation $Q_S = \{P_S^i | \forall i \in (1,2,\dots k), P_S^i =< X_S^i, Y_S^i, Z_S^i, RGB_S^i >\}$
Output: Building areas associated with potential thermal degradations (A_P)

for m=1:k
  $i \leftarrow \arg\min_n \left\| \overrightarrow{P_A^n} - \overrightarrow{P_S^m} \right\|, n \in (1,2,\dots j)$
  $T_A^m \leftarrow TS_{min} + (RGB_A^i - 1) \times \frac{TS_{max} - TS_{min}}{Level_{TS} - 1}$
  $T_S^m \leftarrow CS_{min} + (RGB_S^i - 1) \times \frac{CS_{max} - CS_{min}}{Level_{CS} - 1}$
  return $Q_m =< X_S^m, Y_S^m, Z_S^m, T_A^m, T_S^m >$
end for
$Q_{EPAR} = \{P_i^j | \forall i \in (1,2,\dots k), \forall j \in (1,2,3), P_i^j =< X_i^j, Y_i^j, Z_i^j, T_A^{ij}, T_S^{ij} >, P_i^j \subseteq Q_m\}$
for $i \in (1,2,\dots k)$ & $j \in (1,2,3)$
  if $|T_A^{ij} - T_S^{ij}| >$ *threshold*
    $A_P^i \leftarrow \frac{\left\| \overrightarrow{Q_1Q_2} \times \overrightarrow{Q_1Q_3} \right\|}{2}$
  end if
end for
return $\sum A_P^i$

Figure 7.2 Algorithm for Identifying and Calculating Building Areas Associated with Potential Thermal Degradations in EPAR Models

In the pseudo code (Figure 7.2), j and k indicate the number of points in the 3D thermal point cloud and the number of triangle mesh faces in the VRML-based CFD model respectively. $P^i =< X^i, Y^i, Z^i, RGB^i >$ encapsulates the 3D location (X^i, Y^i, Z^i) and color value (RGB^i) of each 3D point. T_A and T_S indicate the actual and simulated surface temperature of building environments. TS_{max}, TS_{min}, $Level_{TS}$, CS_{max}, CS_{min}, and $Level_{CS}$ represent the maximum and minimum values of the normalized temperature scale and the range of RGB color value charts used for building thermography and VRML-based CFD modeling respectively. Finally, Q_1, Q_2, and Q_3 are the 3D coordinates of the three vertices of the triangle mesh associated with potential performance problems.

7.2 Calculating the Amount of Unnecessary Heat Transfer and Quantifying the Equivalent Energy Cost

The actual heat transfer conditions (R_{Actual}) for the building assemblies associated with potential thermal performance problems are calculated by using the method presented in Section 6.2.2. The

next step for leveraging Equation (18) is to calculate the air-to-air temperature difference across the building envelope over a given time period: $\left|T_{inside} - T_{outside}\right| \times t$. In this research, the 'degree days' statistics is used, which is a numerical index reflecting energy load that is required for space heating or cooling purposes. This index consists of time (t) and temperature difference between inside and outside of buildings. In the 'degree days' statistics, T_{inside} is a predefined baseline, and $T_{outside}$ is the daily average outdoor temperature which is measured from about two hundred contiguous weather stations in the area where the building under inspection is located (The National Oceanic and Atmospheric Administration (NOAA) 2013). Given 1) the building areas associated with potential thermal performance problems detected in EPAR models (A_P); 2) actual thermal resistance measurements of the associated building assemblies at the level of 3D vertex (R_{Actual}); and 3) the 'degree days' statistics ($\left|T_{inside} - T_{outside}\right| \times t$) of the region where the buildings are located, the amount of heat transfer through the defective building can be estimated using Equation (18). The calculated heat transfer can be converted into the equivalent energy cost. Depending on the source of energy used for heating and cooling system in the building under inspection, the corresponding energy cost for space conditioning can be quantified based on the retail price of electricity or natural gas.

Once estimated, building practitioners can propose retrofit alternatives for lowering energy bill and maximizing energy efficiency. For existing buildings, homeowners ideally want specific areas on building envelopes associated with potential thermal degradations to be detected and localized so that their thermal resistances could be improved by adding additional insulations or replacing the old ones. Equation (19) calculates the expected energy savings when the as-is thermal resistances of the defective areas are increased to their recommended value. As an energy performance benchmark, the recommended R-value ($R_{Recommend}$) varies based on the type of building component (e.g., wall, floor, and ceiling) and the geographical location of the buildings under inspection (ENERGY STAR 2013).

$$Q_{Saving} = \left(\frac{1}{R_{Actual}} - \frac{1}{R_{Recommend}}\right) \times A_P \times \left|T_{inside} - T_{outside}\right| \times t \qquad (19)$$

7.3 Estimating the Cost for Building Insulation Retrofits

In presence of temperature difference between inside and outside of buildings, heat flow through

building envelopes is theoretically incontrollable. Nonetheless, homeowners can reduce the unnecessary heat transfers by installing proper insulations or replacing the old ones. In response to the increasing interests in improving thermal resistance of existing buildings, the U.S. Department of Energy and the International Energy Conservation Code (IECC) have established the recommended level of building insulations to facilitate insulation retrofits (ENERGY STAR 2013). Homeowners are provided with general guidance on the most economic insulation level for different climates depending on the locations of the buildings under inspection.

Adding or replacing insulations for finished walls during the operation phase of a building – especially when it is compared to the installation of insulations for unfinished walls during the construction phase – is not a trivial task. According to (U.S. DOE 2012), there are several options including: 1) Blown-in loose-fill insulation: By cutting holes through the façade of existing buildings, loose-fill insulation materials (e.g., fiberglass, cellulose, and mineral wool) can be installed in the cavities of exterior walls. After blowing loose-fill insulations into the cavities of the walls, the holes are plugged and replaced with the finishing materials; 2) Sprayed foam and foamed-in-place insulation: Liquid foam insulation materials such as cementitious and polyurethane can be sprayed (foamed-in-place) to the exterior or interior of the buildings to improve the thermal resistances. This method is effective for the building areas around the obstructions or irregularly shaped; and finally 3) Installation of new sidings to the façade: For improving thermal resistance of building assemblies, homeowners can install rigid insulation boards or add insulation to new sidings. The cost required for these retrofit alternatives can be estimated based on the cost of: 1) the insulation materials and delivery to the jobsite; 2) the delivery of equipment to the jobsite; 3) the required labor and their expected productivity; 4) the restoration of existing finishes and structural components; and finally 5) the cleanup and debris removal for completion. For cost-benefit analysis, the estimated retrofit costs are balanced against the energy cost equivalent to the amount of heat transfer that can be saved by improving the as-is thermal resistances of defective areas to the recommended level.

CHAPTER 8. MAPPING ACTUAL THERMAL PROPERTY MEASUREMENTS TO BIM ELEMENTS FOR RELIABLE ENERGY PERFORMANCE MODELING

In this chapter, given 3D thermal profiles in EPAR models and the as-designed BIM models, the proposed system as outlined in Figure 8.1 focuses on 1) mapping actual thermal resistance measurements at the level of 3D point to the associated BIM elements; and 2) updating their corresponding thermal properties in gbXML schema.

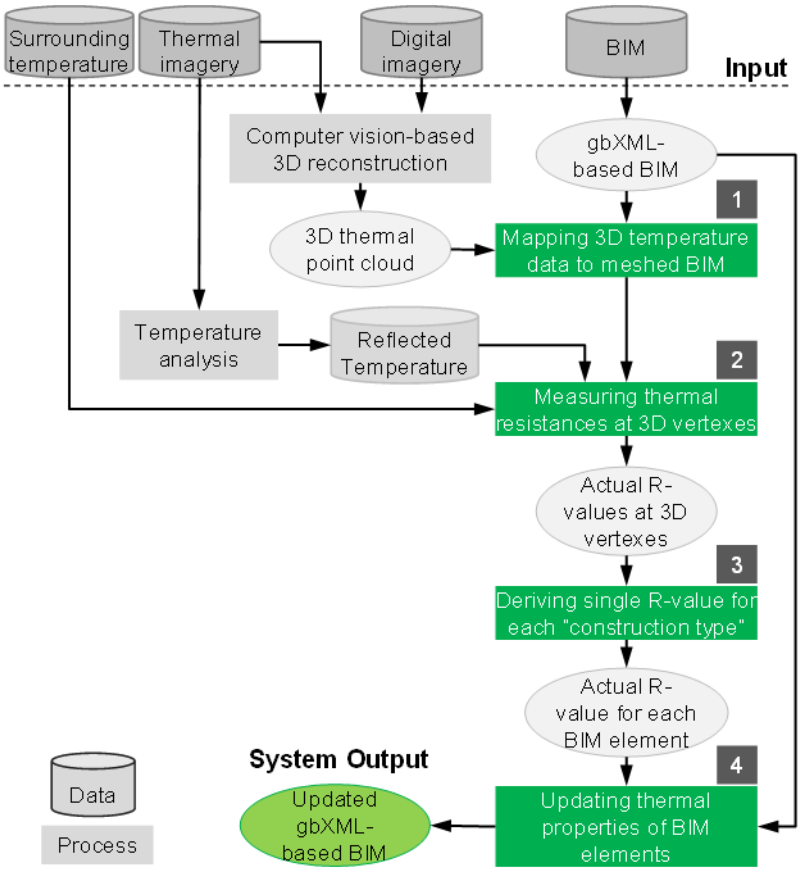

Figure 8.1 Overview of the Data and Process in the Proposed Method for Mapping Actual Thermal Properties to Building Elements in gbXML-based BIM

The system produces an updated gbXML-based BIM, which allows practitioners to accurately model energy performance of existing buildings through BIM-based energy analysis. The following sections describe the underlying algorithms in detail (Ham and Golparvar-Fard 2014; Ham and Golparvar-Fard 2015)

It is assumed that BIM is already developed by modelers. Here, the BIM could be manually

produced, or alternatively the 3D spatio-thermal models produced from the thermal and digital images can be used as a reference for modeling the geometry of the building environment under inspection. Here, the method for producing the 3D spatio-thermal models builds on the computer vision-based pipeline proposed in (Ham and Golparvar-Fard 2013). Using a set of unordered pairwise 2D thermal and digital images (e.g., ~300 to 400 thermal images for around $4\times5m^2$ room) captured from a thermal camera that is already calibrated, the first step is to generate a 3D spatio-thermal model. Using a Structure-from-Motion (SfM) technique, the digital images are localized in a 3D sparse point cloud model that represents the underlying geometry of the building environment under inspection. By deriving the relative pose for the thermal and digital image pairs using their underlying Epipolar geometry, the thermal images are also localized with respect to the same underlying point cloud model. Because thermal images have low spatial resolutions and lack distinct visual features, their direct application to SfM is challenging. The proposed method for solving the relative pose of a thermal camera with respect to a built-in digital camera facilitates the process by allowing the calibrated thermal images to be directly used for dense 3D reconstruction. The Multi-View Stereo (MVS) algorithm is used to generate a dense 3D thermal point cloud model, which denote as $\langle P_A^1, P_A^2, \ldots, P_A^j \rangle$. Here, j is the number of points in the resulting 3D thermal point cloud model. This pipeline of computer vision algorithms automatically generates 3D spatio-thermal point clouds in which actual surface temperatures of the building environment are modeled in 3D.

Using a BIM-authoring tool (e.g., Autodesk Revit or ArchiCAD), detailed descriptions of the buildings under inspection are presented in form of the gbXML schema. In the gbXML-based BIM, thermal properties of each building element are typically based on the notional values obtained from industry standard databases of typical building material properties available in the BIM-authoring tools. The first step to update these values, as shown with "1" in Figure 8.1, maps the as-is thermal profiles from 3D spatio-thermal models to their corresponding BIM elements. This is done by discretizing the building elements in gbXML-based BIM into a mesh. "2": With environmental measurements, the as-is thermal resistance of building assemblies are calculated at the level of vertex in meshed BIM. "3": For all exterior building elements with the same "construction type" in the underlying BIM, a single R-value is derived from the 3D vertex-level thermal resistance measurements. "4": The corresponding entries for the single R-value in the underlying gbXML schema is automatically updated, allowing energy auditors to exploit the

resulting updated gbXML file for BIM-based energy analysis. Here, 'meshed BIM' indicates '3D mesh model based on the boundary points representing gbXML-based BIM elements surfaces'. Here, the manual processes are (1) producing the BIM – either directly from site measurements or using the underlying 3D spatio-thermal models as the basis – and exporting baseline gbXML file from pre-existing BIM files using current BIM authoring tools such as Autodesk Revit; and (2) registering the 3D spatio-thermal model into the BIM coordinate system. Given the input data, the proposed system produces the updated gbXML-based BIM, which reflects the as-is condition of the existing building under inspection. The following sections describe each step of the underlying method for mapping the thermal property measurements to BIM elements and updating their corresponding entries in gbXML-based BIM.

8.1 Mapping 3D Thermal Profiles of Building Environments to Meshed BIM

The proposed system leverages a 3D spatio-thermal model from the collection of thermal and digital images. Using a registration process, a few 3D points are selected from the 3D spatio-thermal model ($P^i_{Thermal}$) and their corresponding BIM coordinates from gbXML-element 'CartesianPoint' (P^i_{BIM}). Given a minimum of three corresponding points, the point cloud is transformed into the BIM coordinate system by solving for the transformation in a least square form (i.e., scaling factor (s); rotation (R($P^i_{Thermal}$)); and translational offset (T)) by minimizing the sum of squared residual errors of the Euclidean transformation for *n* matching control points (Horn 1987) as follows:

$$\sum_{1}^{n} \left\| e^i \right\|^2 = \sum_{1}^{n} \left\| P^i_{BIM} - sR\left(P^i_{Thermal}\right) - T \right\|^2 \tag{20}$$

Once the collected images are processed, the resulting 3D point cloud models may be incomplete or noisy. For examples, the flat surface on drywall and plaster may not produce enough visual features for computer vision-based 3D reconstruction. Also, 3D point cloud models would include several points that do not belong to the building geometry itself. To address these issues and toward consistent representation of actual thermal performance, building boundary points representing surfaces of building elements are extracted from the gbXML-based BIM, and then a uniform mesh for the geometrical baseline is created by discretizing the surfaces into square mesh

faces of similar size. Then, the temperature values from the 3D thermal point cloud are mapped to the vertices that are uniformly distributed on geometrical baseline mesh. There are about 400 elements and attributes in the latest gbXML schema (Sokolov and Crosby 2011). Figure 8.2 highlight the parts of the gbXML schema that will be used for the proposed method to update thermal properties of BIM elements, which represent the geometrical information of BIM elements.

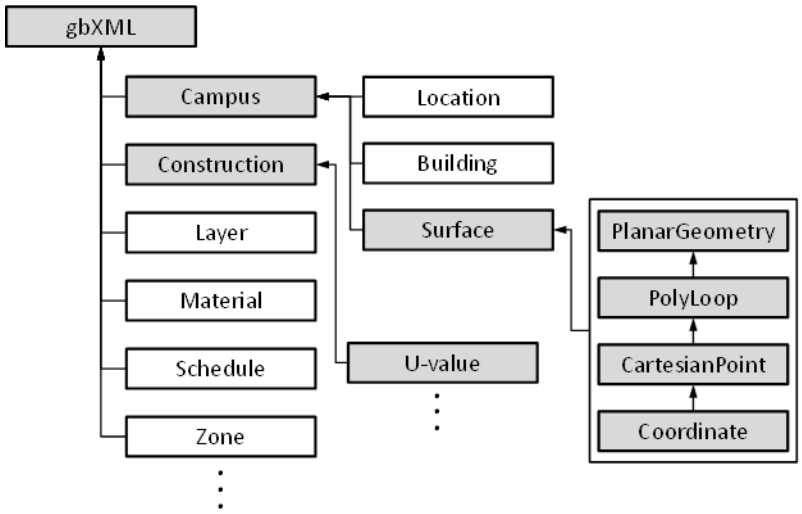

Figure 8.2 Logical Structure of the Elements in gbXML Schema

Within the gbXML-based BIM, the exterior building elements are first located by finding gbXML-elements 'Surface' that are characterized by "ExteriorWall" for the attribute "surfaceType". Each gbXML-element 'Surface' has the sub-element 'PlanarGeometry' which defines the plane on which the 3D surface polygon lies. The gbXML-element 'PlanarGeometry' has another sub-element 'PolyLoop'. This element describes the polygon shape of the surface. Similarly, the gbXML-element 'PolyLoop' also has several sub-elements 'CartesianPoint' which contain the 3D coordinates of the vertices that shape the rectangular face.

For meshing the rectangular face of each building element, the 3D coordinates of the face boundary points are derived. This is done by querying the content of the sub-element 'Coordinate' of the queried gbXML-element 'CartesianPoint'. Once the four boundary points are determined, the uniform mesh is formed. Here, if there exist the sub-elements 'Opening' in the gbXML-elements 'Surface', the areas formed by the gbXML-element 'CartesianPoint' of the gbXML-element 'Opening' are not considered as wall assemblies. To create the uniform mesh, new vertices

are added on the BIM element surface. In the proposed method, these vertices are generated by dividing the plane surface into a set of identical areas. Next, in the resulting meshed BIM, the 3D coordinates of the centroid points $\langle P_C^1, P_C^2, \ldots, P_C^i \rangle$ of each mesh face for the building element are calculated as the basis of the transformation. Here, i is the number of mesh faces in each BIM element. Then, the surface temperature data in the 3D spatio-thermal point cloud $\langle P_A^1, P_A^2, \ldots, P_A^j \rangle$ is mapped to the centroid of each mesh faces $\langle P_C^1, P_C^2, \ldots, P_C^i \rangle$. To do that, a *k-d* tree structure is created for a set of points, and the nearest neighborhood searching algorithm is used to find the closest point P_A^i for each P_C^i. Finally, the RGB color values of P_A^i (RGB_A^i) are assigned to P_C^i, which represents the surface thermal profiles. This temperature reading is averaged from all thermal images that observed the vertex during the thermographic inspection.

8.2 Measuring Actual Thermal Resistance at the Level of 3D Vertex in Meshed BIM

Here, $T_{inside,wall}$ can be extracted from the gbXML-based 3D thermal mesh model at the level of 3D point. It is hypothesized that if the nearest thermal points are physically far from vertices in the meshed BIM, those thermal points are most likely associated with non-relevant objects that their presence is blocking the line of sight of the camera. Thus, those thermal points need to be disregarded for calculating the thermal resistances of the building assemblies. To identify such noise – i.e., 3D thermal points which have a certain distance from the gbXML-based BIM, a geometrical distance threshold is set based on point cloud-to-BIM registration error. Once all parameters are determined, the actual thermal resistances for each building assembly under inspection can be calculated at the level of vertex in meshed BIM by using Equation (14).

8.3 Deriving a Single R-value for Building Elements

Considering the as-is condition non-uniformity of building assemblies across regions that may have been degraded differently over time, the proposed vertex-level measurement by leveraging surface temperature data queried from the meshed BIM at the level of point – in contrast to a single measurement for each building element – will better characterize the as-is building condition. Nonetheless, to run a simulation engine for calculating energy loads, current energy analysis software typically require a single thermal property to be input for each building element.

To derive a single R-value from vertex-level measurements for building elements, the heat transfer through each mesh face is first calculated, and then the measurements for all faces that

belong to a given element is averaged (i.e., weighted average based on the contribution of each measurement to the associated surface area). In the meshed BIM, the amount of heat transfer through the entirety of the building element is identical to the sum of the amount of heat transfer through each mesh face of that building element. Based on Equation (17), this relationship can be described by using the following equation:

$$\frac{1}{R_{total}} \times A_{total} \times (\Delta T \times t) = \left(\frac{1}{R_1} + \frac{1}{R_2} + \cdots + \frac{1}{R_k}\right) \times (\frac{1}{k} \times A_{total}) \times (\Delta T \times t) \quad (21)$$

Here, k is the number of mesh faces for each building element in the meshed BIM. Based on Equation (21), the single R-value for each building element is derived by using the following equation:

$$R_{total} = \frac{k}{\sum_{n=1}^{k} \frac{1}{R_n}} \quad (22)$$

Since the geometry of building assemblies in gbXML schema is based on the centerline of the building assemblies, the actual building area under inspection is slightly different from the area of the corresponding building surfaces in the gbXML-based BIM (A_{total}). This deviation is attributed to the thickness of the building assemblies. However, since the area parameter (A_{total}) is disregarded when converting Equation (21) to (22), this geometrical error does not affect the as-is thermal resistance. The association of the derived single R-value to the corresponding gbXML-element for updating is explained in the next section.

8.4 Updating Thermal Properties of BIM Elements in gbXML Schema

Figure 8.3 summarizes the overall algorithm for 1) mapping the thermography-based measurements to BIM elements; and 2) updating their corresponding entries in gbXML schema.

Inputs: Measurement $Q_A = \{P_A^i | \forall i \in (1,2,...j), P_A^i =< X_A^i, Y_A^i, Z_A^i, RGB_A^i >\}$ and BIM

Output: gbXML-based BIM with updated thermal properties

Convert BIM into gbXML schema
forall exterior building elements (m) with a "construction type"
  Extract the coordinates of all boundary points
  Create a uniform rectangular mesh
  Calculate the centroid (P_C) of all mesh faces in 3D
  foreach mesh face (i) in the element
    Choose a nearest point P_A^k in Q_A w.r.t. the centriod P_C^i such that

$$\underset{k}{\operatorname{argmin}} \left\| \overrightarrow{P_A^k} - \overrightarrow{P_C^i} \right\| ; k \in (1,2,...j)$$

    Derive RGB value (RGB_A^k) for P_A^k and find corresponding temperature value (T_m^i)
    Calculate R_m^i using Eq (4) together with $T_{\text{inside ,wall}}$ derived from T_m^i
  end
end
Derive a single R-value for exterior building elements with a "construction type"
'U-value' for each "construction type" in the gbXML-based BIM $\leftarrow 1/R_m$
return updated gbXML-based BIM

Figure 8.3 Pseudo code for Updating Thermal Properties of Building Elements Adjacent to Exteriors in gbXML-based BIM

Here, j is the number of point in the 3D thermal point cloud model of building environments, and m is the number of building elements adjacent to the exterior for each "construction type". T_m^i and R_m^i indicate the surface temperature and the as-is thermal resistances of the building assemblies at the level of 3D vertex in meshed BIM. R_m is a single thermal resistance derived for each building element.

Once the single R-values for the building elements are determined, the thermal property of the BIM elements is updated in their corresponding gbXML entries. To do that, the system needs to locate and access the gbXML-element associated with the thermal properties of the building elements which need to be updated. The updating process is based on the navigation of the tree structure represented by the gbXML schema (Figure 8.2) and the relationships between the nodes. To do that, the XML Document Object Model (DOM) is leveraged, which is a platform and language-neutral interface to enable dynamic access and update of the contents of XML document (W3C 2013). This presents XML documents as a tree-structure and defines the 'objects' and 'properties' of all XML elements, and the associated interface to access and manipulate them. For example, 'getElementsByTagName()' method is used to search for all elements in the sub-tree that

have a certain entry such as the gbXML-element ‘Construction’ (or ‘WindowType’) based on the attribute “constructionIdRef” (or ‘windowTypeIdRef’) of the gbXML-element ‘Surface’. Here, for implementation, the system takes advantage of Java environment that runs with MATLAB platform. In the gbXML schema, for wall and door components, the geometrical information and the thermal properties are located in "Surface" and "Construction" elements respectively. In the case of window components, the geometrical information and the thermal properties are located in "Surface" and "WindowType" elements. To find the gbXML-element ‘Construction’ (or ‘WindowType’) that is associated with the exterior building elements, the system first extracts the attribute “constructionIdRef” (or ‘windowTypeIdRef’) of the gbXML-element ‘Surface’ that is characterized by “ExteriorWall” for the attribute “surfaceType” (or “OperableWindow” for the attribute “openingType”). Next, the system finds the gbXML-element ‘Construction’ (or ‘WindowType’) that its attribute “id” is identical to the attribute “constructionIdRef” (or ‘windowTypeIdRef’) of the gbXML-element ‘Surface’. Finally, in the queried gbXML-element ‘Construction’ (or ‘WindowType’), the content of the sub-element ‘U-value’ is changed to the reciprocal of the actual R-value that is derived in Section 8.3. Ultimately, by using the updated BIM as an input for the BIM-based energy analysis tools, energy performance of existing buildings can be more accurately modeled and analyzed for better sustainable retrofit decision-makings.

CHAPTER 9. EXPERIMENTAL RESULTS AND DISCUSSION

9.1 Data Collection and Experimental Setup

To validate the proposed methods, a series of experiments were conducted. The image datasets for the experiments were collected from total ten interior and exterior locations in both existing residential building and instructional facilities. For the instructional facility, a façade (IF#1), an office room (IF#2), a main hall (IF#3), a corridor (IF#4), another office room (IF#5), and the lobby area (IF#6) were considered for experiments. For a residential building, a façade (RB#1), a kitchen room (RB#2), a bedroom in summer (RB#3), and the bedroom in winter (RB#4) were selected. For all experiments, digital and thermal images were simultaneously captured using an FLIR E60 thermal camera which has a built-in digital camera. Table 9.1 shows the technical specifications of the thermal camera.

Table 9.1 Camera Technical Specification

Camera Technical Items	Values
Built-in digital camera resolution	3.1M pixel (2048 × 1536 pixels)
Thermal camera resolution	320 × 240 pixels
Digital camera Field of View (FOV)	53° × 41°
Thermal camera Field of View (FOV)	25° × 19°
Thermal sensitivity	< 0.05°C
Thermal measurement accuracy	±2°C or ±2% of reading
Measurement object temperature range	-20°C to +120°C
Operating temperature range	-15°C to +50°C

For EPAR modeling, the office room in the instructional facility (IF#2) was modeled as follows: the walls were modeled as concrete; the floor and ceiling were modeled as concrete masonry units and gypsum boards respectively. Then, the bedroom in the residential building (RB#3) was modeled as follows: the floor was modeled as concrete; and the ceiling and walls were modeled as wood. Finally, another office room in the same instructional facility (IF#5) was modeled as follows: the floor and ceiling were modeled as concrete; and the walls were modeled as concrete and gypsum board. All windows and doors in the building spaces are modeled as closed conditions in the all experiments. For benchmark performance based on the as-designed building information, the material properties are assumed to be consistent shown in Table 9.2.

Table 9.2 Material Properties Used in Case Studies

Materials	Thermal conductivity (*W/m-k*)	Density (*kg/m3*)	Specific heat (*J/kg-k*)
Concrete	0.7	2370	750
Glass	0.96	2580	840
Gypsum board	0.17	10.2	1090
Wood	0.13	10.4	2500
Air	0.024	1.225	1006

Since the numerical analysis for building environments is typically implemented in a steady state, the airflow from HVAC systems is assumed to be uniformly distributed on all supply openings with a constant temperature and velocity. The detailed experimental setup for simulation are summarized in Table 9.3.

Table 9.3 Experimental Conditions for Simulation

Technical Items	IF#2	RB#3	IF#5
Turbulence model	RNG $k-\varepsilon$ model	RNG $k-\varepsilon$ model	RNG $k-\varepsilon$ model
Number of vertices in mesh	2,778,117	2,830,660	4,621,160
Time of the experiment	Winter (December)	Summer (July)	Winter (December)
Fluid (air) motion type	Stationary	Stationary	Stationary
Flow rate weighting for each outflow	1.0	1.0	1.0
Operating pressure of air flow	101,325 N/m^2	101,325 N/m^2	101,325 N/m^2
Temperature of inlet air	32°C (Heating)	19°C (Cooling)	35°C (Heating)
Velocity of inlet air	0.7 m/s	0.6 m/s	0.3 m/s
Wall motion type	Stationary	Stationary	Stationary
Wall shear condition	No slip	No slip	No slip
Wall surface temperature, window	11°C	28.3°C	18°C
Wall surface temperature, ceiling	13°C	23.5°C	22°C
Wall surface temperature, floor	15°C	24°C	22°C
Wall surface temperature, wall 1$^+$	14.2°C	23.5°C	18.5°C
Wall surface temperature, wall 2$^+$	13.5°C	23.5°C	22.5°C
Wall surface temperature, wall 3$^+$	14°C	25.5°C	22.5°C
Wall surface temperature, wall 4$^+$	14.2°C	26.5°C	22.5°C
Wall roughness height	0	0	0
Wall roughness constant	0.5	0.5	0.5

$^+$ These walls are shown in Figures 9.8(a), 9.9(a), and 9.10(a) respectively.

9.2 Performance Evaluation Measures

(1) Regarding 3D spatio-thermal modeling of building environments and further EPAR modeling,

the outcomes of the image-based 3D reconstruction are first evaluated in terms of the model completeness (e.g., the density of the point clouds and the percentage of successfully registered images), the computational time required for both CPU and GPU-based implementations, and the simulation accuracy. In addition, the 3D-registration accuracy of the resulting 3D spatio-thermal model into the site coordinate system is examined by looking at the geo-registration error. This error gives an indication of how precisely 1) the as-is thermal profile of building environments can be characterized in 3D; and 2) the performance comparison can be conducted in EPAR environments.

(2) Regarding identifying potential performance problems based on performance deviation, the outcomes of the proposed EPAR-based method were compared with the results of manual thermographic inspection. First, based on the thermographic inspection guidelines (Eads 2000; FLIR system 2012), thermal images representing energy problems are first identified through manual inspections. The results are then compared with thermal images containing potential performance problems identified by the proposed EPAR-based method. This comparison gives an indication of how accurately energy problems can be detected by leveraging the performance deviation in EPAR models.

(3) Regarding calculating the actual thermal resistances and detecting condensation issues at the level of 3D point, the following metrics are used: 1) Accuracy of measuring thermal resistances using building thermography before leveraging 3D thermal models: To do that, the deviations between the measurements and the notional values are examined. It is noted that wall assembles are not the best choice for such experiments since wall assemblies typically have multiple layers and are likely to suffer from non-uniform and time-variant degradations. Hence, using theoretical expected R-values as the ground truth of the as-is thermal resistances may not be reliable. In contrary to walls, since windows are mostly standardized and their thermal properties are more likely to be consistent over time, their actual thermal resistance is less likely to deviate from the notional values derived from the as-built documents. Thus, for this metric, window components are considered. First, thermal imagery representing window components for case studies is first manually selected, and then the temperature values are obtained from the images by matching the RGB color values at the pixel level with a given color spectrum. Using the measurements as $T_{inside,wall}$ in Equation (14), the thermal resistance is calculated, and the outcome is compared with the notional value; and 2) Accuracy of mapping 3D thermal point clouds to a

geometrical baseline mesh: This evaluates the accuracy of modeling the as-is thermal profile in 3D which is important for both calculating thermal resistances and detecting condensation problems at the level of 3D point. To do that, the registration accuracy of 3D spatio-thermal point cloud with the baseline mesh in the site coordinate system is examined. It is noted that mapping thermal point clouds to a geometrical baseline mesh involves transforming the 3D spatio-thermal model into the real-world site coordinate system. To determine this transformation, the closed-form solution using unit quaternions is used (Horn 1987). The transformation from the 3D spatio-thermal model into the real-world has 7 degrees of freedom, and thus requires a minimum of three matching control points between the 3D spatio-thermal model and the real-world coordinate system (Ham and Golparvar-Fard 2013). These control points, $P^i_{Thermal}$ and P^i_{Site}, can be extracted from the known dimension of the building components. This is solved by minimizing the sum of squared residual errors of the Euclidean transformation for *n* control points.

(4) Regarding 3D thermography-based method for cost analysis of energy efficiency building envelope retrofits, the first case is a bedroom in an existing residential building built in 1970's (RB #4), and the second is an office room in an instructional facility originally built in 1926 as a single-story building, and then upgraded with three additional floors in 1929 (IF #2). The last case is the lobby area of the same instructional facility (IF #6). To study the impact of different environmental conditions such as climate on energy savings associated with insulation retrofits, four additional hypothetical scenarios are created by assuming the buildings under inspection are located in different climatic zones (Florida and Minnesota) in the U.S., and then the expected energy cost savings for each case are analyzed.

(5) Regarding mapping actual thermal property measurements to BIM elements in gbXML schema for reliable building energy performance modeling, the two metrics are considered. The first aspect is how accurately the as-is thermal resistances are calculated. For validation, the deviations between the measurements and the notional values were calculated. The second aspect is how precisely thermal resistance values at the level of 3D point are mapped to each nearest vertex in the meshed BIM. This value is calculated by minimizing the sum of squared residual errors of Euclidian transformation for *n* control points. In this work, the scope of updating gbXML is limited on exterior wall assemblies. The two cases (RB #4 and IF #2) were in the corner of the building layout and thus performed the measurements for two wall assemblies in each building space.

9.3 Experimental Results and Discussions

In this section, the experimental results on the 3D spatio-thermal modeling are first presented, and subsequently the experimental results on EPAR modeling, the identification of potential performance problems, 3D building condition assessment (i.e., calculating the as-is thermal resistances and detecting condensation issues), the associated cost analysis, and finally mapping actual thermal property measurements to the associated BIM element are followed in detail.

9.3.1 3D spatio-thermal modeling of building environments

Figure 9.1 to 9.6 present several snapshots from the outcome of the 3D spatio-thermal modeling on each of experiments. Particularly, Figure 9.1 and 9.2 show results on the façades of the instructional facility and a kitchen of the residential building respectively. The resulting building geometrical and thermal point cloud models are shown for each case. As observed, one example on the location of the camera and rendering of the associated 3D-registered thermal and digital images are shown. Figures 9.3 and 9.4 show the outcomes for the other indoor and outdoor building environments. In the second row for each case, 3D thermal point cloud models as well as the 3D-registration of the thermal and digital images with respect to the thermal point clouds are further visualized. Figures 9.5 and 9.6 show the 3D spatio-thermal models for both outdoor and indoor environments through the automated superimposition of building geometrical and thermal point cloud models. Also, the 3D registration of the thermal and digital images is shown in the 3D spatio-thermal models of each case.

Here, the visualization tool supports several modes for navigation in the 3D spatio-thermal models along with thermal and digital images. These modes include free-flight navigation, finding related building views, area-based navigation, and viewing 3D-registered images. The navigation controls are similar to most engineering 3D viewers. For example, users can move the virtual camera in 3D and pan, tilt, and zoom it. This allows energy auditors to virtually move around the 3D reconstructed scene and provides a simple way to find proper viewpoints, or associated digital and thermal images. At any time, users can also choose a frustum, and the virtual camera will divert into the selected camera. In this case, the frustum will be rendered by full-resolution thermal or digital images along with the 3D reconstructed scenes.

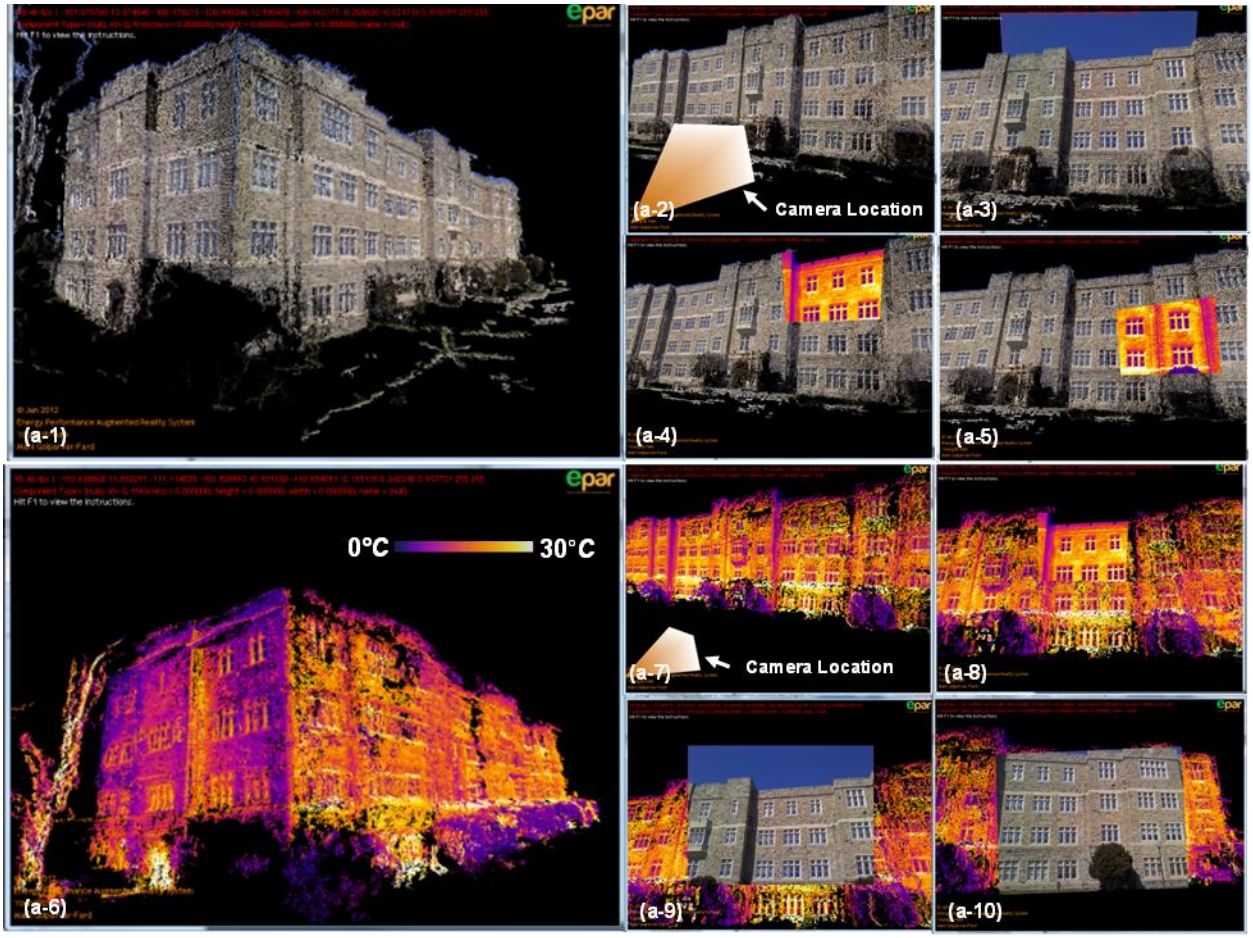

Figure 9.1 3D Building Geometrical and Thermal Point Cloud Models of Façades of an Instructional Facility (IF#1): (a-1) Building Point Cloud Model; (a-2) a Camera Frustum; (a-3) the Same Camera Frustum Rendered with the 3D-registered Digital Image; (a-4,5) the Same Camera Rendered with the 3D-registered Thermal Images; (a-6) Thermal Point Cloud Model; (a-7) a Camera Frustum; (a-8) the Same Camera Frustum Rendered with the 3D-registered Thermal Image; (a-9,10) the Same Camera Rendered with the 3D-registered Digital Images

Figure 9.2 3D Building Geometrical and Thermal Point Cloud Models of a Kitchen Room of a Residential Building (RB#2): (a-1) Building Point Cloud Model; (a-2) a Camera Frustum; (a-3) the Same Camera Frustum Rendered with the 3D-registered Digital Image; (a-4,5) the Same Camera Rendered with the 3D-registered Thermal Images; (a-6) Thermal Point Cloud Model; (a-7) a Camera Frustum; (a-8) the Same Camera Frustum Rendered with the 3D-registered Thermal Image; (a-9,10) the Same Camera Rendered with the 3D-registered Digital Images

Figure 9.3 3D Building Geometrical and Thermal Point Cloud Models: (a) a Façade of the Residential Building (RB#1); (b) an Office Room of the Instructional Facility (IF#2)

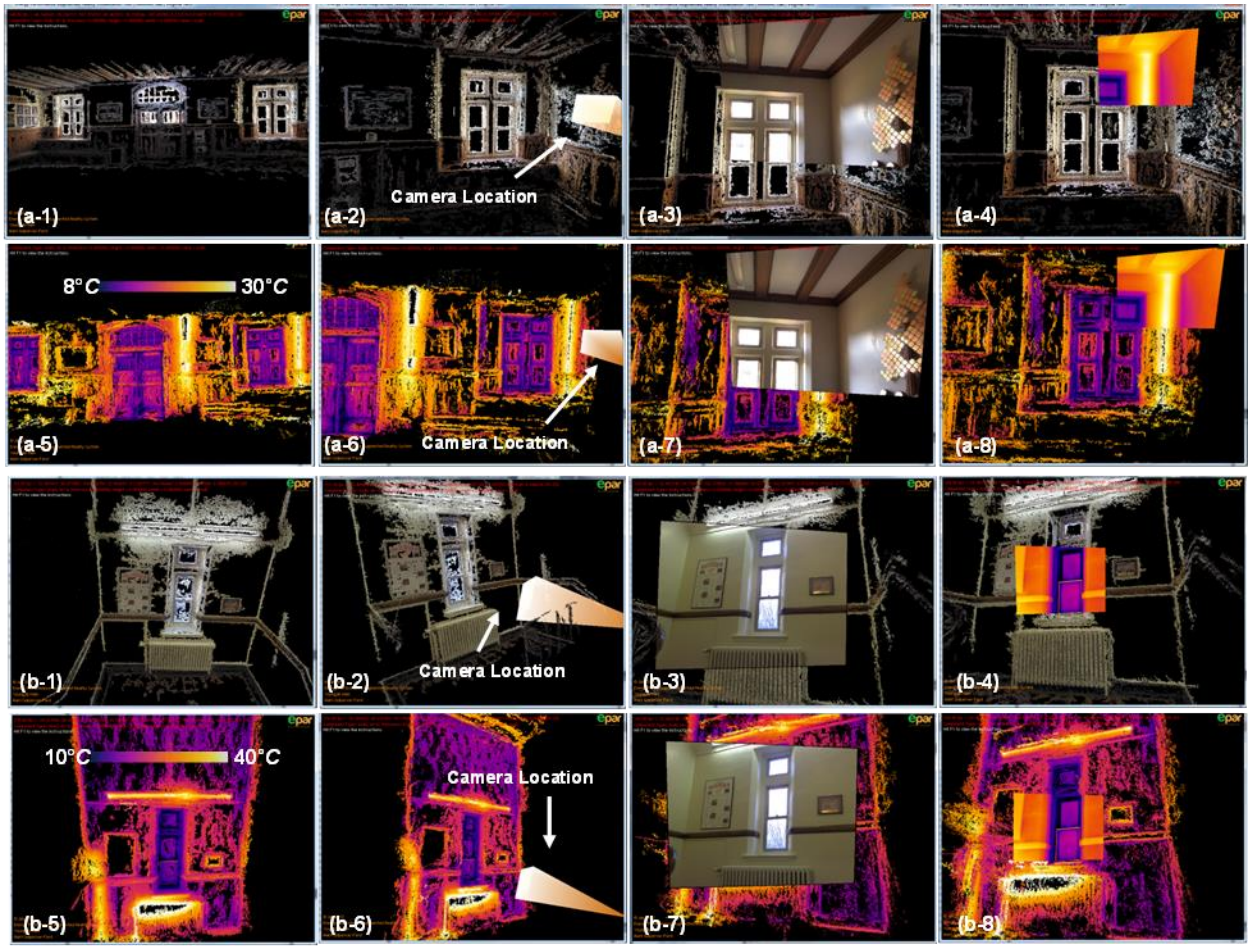

Figure 9.4 3D Building Geometrical and Thermal Point Cloud Models: (a) a Main Hall of the Instructional Facility (IF#3); (b) a Corridor of the Instructional Facility (IF#4)

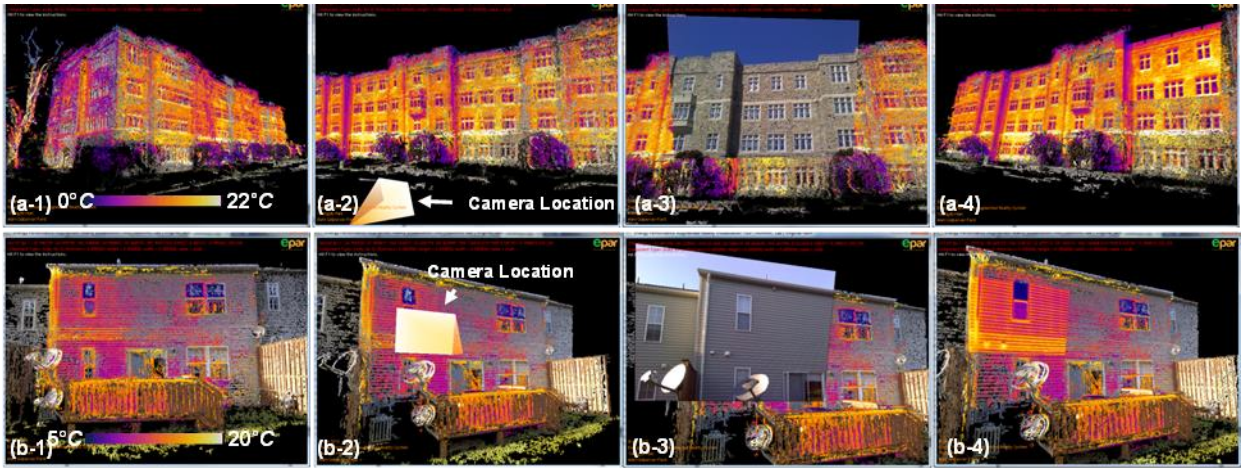

Figure 9.5 3D Spatio-Thermal Models with 3D-registered Digital and Thermal images: (a) the Façade of the Instructional Facility (IF#1); (b) the Façade of the Residential Building (RB#1)

Figure 9.6 3D Spatio-Thermal Models with 3D-registered Digital and Thermal Images: (a, b, and c) an Office Room (IF#2), a Main Hall (IF#3), and a Corridor in the Instructional Facility (IF#4); (d) a Kitchen Room in the Residential Building (RB#2)

Table 9.4 Experimental Results of 3D Reconstruction (IF #1, #2, #3, #4, and #5: Façades, an Office Room, a Main Hall, a Corridor, and another Office Room in the Instructional Facility, RB #1, #2, and #3: Façades, a Kitchen Room, and a Bedroom in the Residential Building)

	IF #1	IF #2	IF #3	IF #4	IF #5	RB #1	RB #2	RB #3
# of digital images	678	440	210	191	209	79	165	452
# of thermal images	678	440	210	191	209	79	165	452
# of digital images registered	672	429	195	167	170	79	93	382
Success ratio on digital image registration	0.99	0.98	0.93	0.87	0.81	1	0.56	0.85
# of building point clouds	28,552,261	8,488,888	2,250,470	1,837,529	3,614,375	1,630,587	2,262,349	3,458,541
# of thermal point clouds	2,489,117	2,838,478	1,369,316	1,417,957	527,715	824,747	220,428	1,977,623
Computation time (CPU-based implementation)$^{+}$	242hr 40min	5hr 55min	2hr 31min	2hr 23min	3hr 1min	1hr 31min	2hr 5min	3hr 29min
Computation time (GPU-based implementation)$^{+}$	10hr 50min	2hr 21min	47min	30min	1hr 12min	22min	26min	1hr 52min

$^{+}$ Benchmarked on Intel(R) Core(TM) i7 960 with 24GBs RAM and NVIDIA GeForce GTX 400

Table 9.4 presents detailed information on the conducted experiments and shows the results for validating each experiment based on the metrics presented in Section 9.2. As observed, for the eight experiments that were conducted, the numbers of digital and thermal images used are presented. For each experiment, the success ratios for registration of the digital images to the underlying 3D reconstructed scene are also shown. In almost all of experiments, as observed, a relatively high number of images were collected and registered for each of case studies. Nonetheless, in RB#2 experiment where a kitchen was being reconstructed in 3D, the wide baseline among digital images and the lack of distinct features in most surfaces resulted in poor 3D reconstruction outcomes. Also, the success ratio of 0.85 and 0.81 in RB#3 and IF#5 respectively show that several images did not have enough overlap with other images in the data set. Table 9.4 further presents the density of the reconstructed point cloud models. As observed, the density of the thermal models is considerably smaller than that of the building geometrical point cloud models. This is due to the low spatial resolution and small field-of-view of thermal images with a lack of distinct feature points. The computational time required for 3D modeling process are also presented. The computational time benchmarked on a typical engineering workstation still seems quite reasonable. The proposed new GPU-based platform significantly cuts

the computational time for image-based 3D reconstruction. Nonetheless, significant computation time was observed on the IF#1 experiment where 678 images were used. Through the GPU-based implementation, the building façades with approximately 3,528 S.F. was able to be reconstructed in about 11 hours using a regular engineering workstation (Benchmarked on an Intel i7 960 core with 24GBs RAM and NVIDIA GeForce GTX 400). The results in all cases are promising, though still more studies need to be done to reduce the computational cost.

The accuracy of registering the 3D spatio-thermal models with the site coordinate systems was measured by calculating the registration error, and the results are presented in Table 9.5. As observed, although the method was tested on different cases with varying number of registration points (i.e., more than 3 points which is the minimum numbers of the required points for solving 7 DOF transformation), the registration errors were within a reasonable practical range. Undoubtedly, the accuracy is sensitive to how the control points are selected in a supervised manner. Since more than the minimum numbers of the required control points (three) were selected in experiments, such errors were minimized. This level of accuracy holds promise that high precision comparison tasks between actual and simulated thermal performance can be conducted in EPAR environments later.

Table 9.5 Errors of Registering the 3D Spatio-Thermal Model with the Site Coordinate System

	IF #1	**IF #2**	**IF #3**	**IF #4**	**IF #5**	**RB #1**	**RB #2**	**RB #3**
Number of corresponding points	8	7	8	8	9	6	7	9
Δe_{inch}	0.7747	0.366	0.3379	0.2809	0.2642	0.0344	0.2239	0.2791

The correlation between the number of images per 100 S.F. of visible areas and the density of the point cloud was also studied. Figure 9.7 shows the results of experiments on the exterior of the instructional facility (IF#1). The surface area excluding the roof was 3,528 SF. Seven experiments were conducted with different numbers of images decreasing from 672 to 72. For each case, an image from every pair of image with almost similar contribution to the outcome of the 3D reconstruction was gradually removed. Figure 9.7 presents the relationship between the density of the 3D point cloud and the numbers of images per 100 S.F. In almost all cases, an average number of 10 images per 100 S.F. seems to be a practical number. Given different types of building surface materials, this number is more likely to vary.

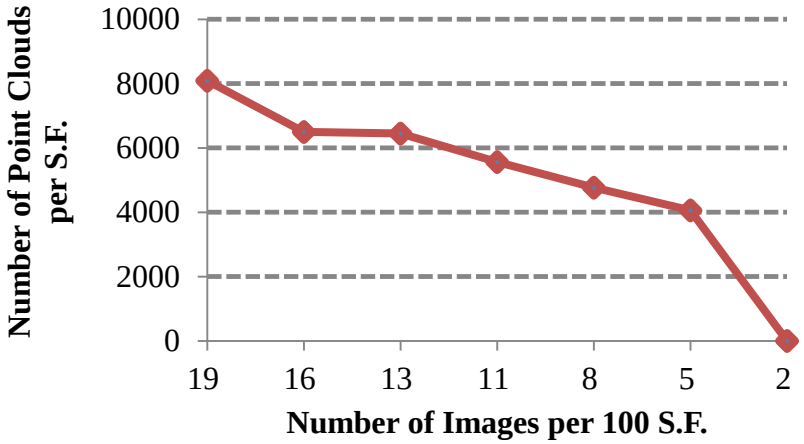

Figure 9.7 Density of Image-based 3D Point Clouds vs. the Number of Images per S.F.

9.3.2 Energy Performance Augmented Reality (EPAR) modeling and inferring potential performance problems based on performance deviations

In order to validate EPAR modeling method, three experiments were conducted: an office room of an instructional facility during winter (IF#2); a bedroom of a residential building during summer (RB#3); and a different office room of the same instructional facility during winter (IF#5). Figure 9.8, 9.9, and 9.10 show actual and simulated 3D spatio-thermal models and the 3D-registered images for the experiments (IF#2, RB#3, and IF#5 respectively). Subfigure (a), (b), and (c) of each figure show the 3D building geometrical, 3D thermal, and 3D spatio-thermal models wherein (c) illustrates the superimposition of (a) and (b). Subfigure (d) shows the expected 3D spatio-thermal model. This model is the outcome of the numerical analysis for which the required 3D building geometry was extracted from the 3D building geometrical point cloud (Subfigure (a)). Users can navigate the 3D models, view the scene from any given camera viewpoint, and study the thermal performance illustrating the underlying as-is building conditions. Subfigure (f), (g), and (h) present the building geometrical and thermal point clouds along with the automatically 3D-registered digital and thermal images. The locations and orientations of each camera registered in the 3D virtual environment (Subfigure (e)) are automatically calculated without a help from dedicated location tracking technologies such as GPS, Ultra Wideband, or RFID tags. In fact, the camera extrinsic parameters required for image-based 3D localization are calculated through the SfM (for digital images) and the relative pose of thermal camera lens with respect to the digital camera lens

(for thermal images). In these figures, the camera location is preserved, and the field of view can be slightly tilted to provide better visualization. With 3D-registered images on the 3D reconstructed scene, the actual thermal performance and geometrical conditions of the building environments can be interactively explored.

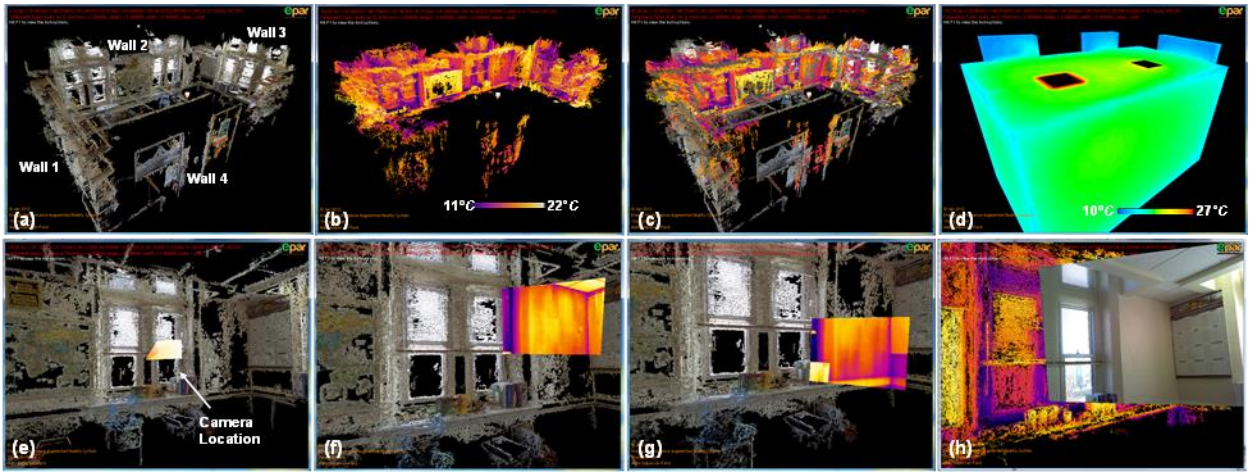

Figure 9.8 Actual and Simulated 3D Spatio-Thermal Models of IF#2 with 3D-registered Images

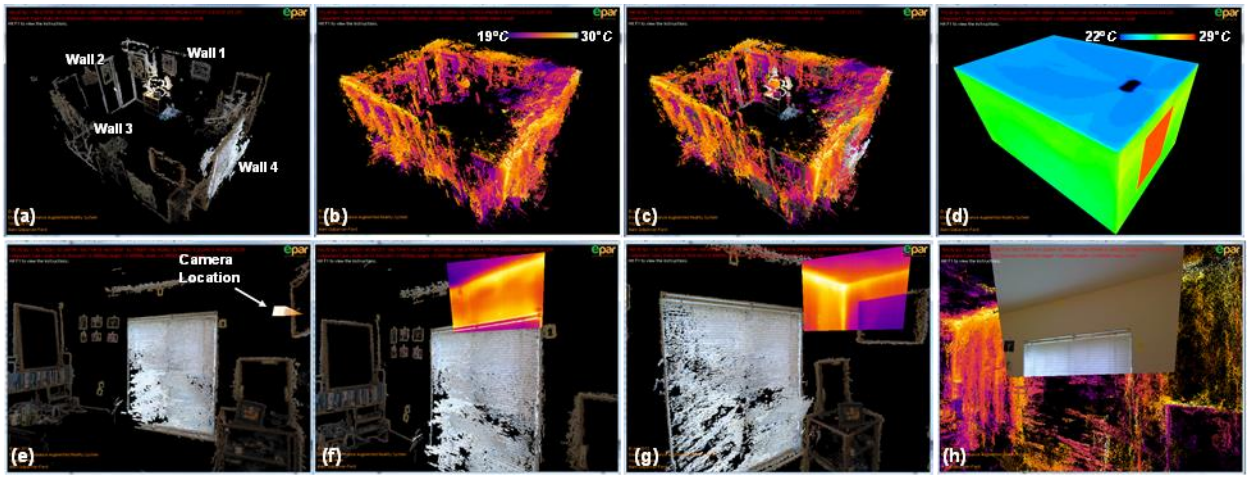

Figure 9.9 Actual and Simulated 3D Spatio-Thermal Models of RB#3 with 3D-registered Images

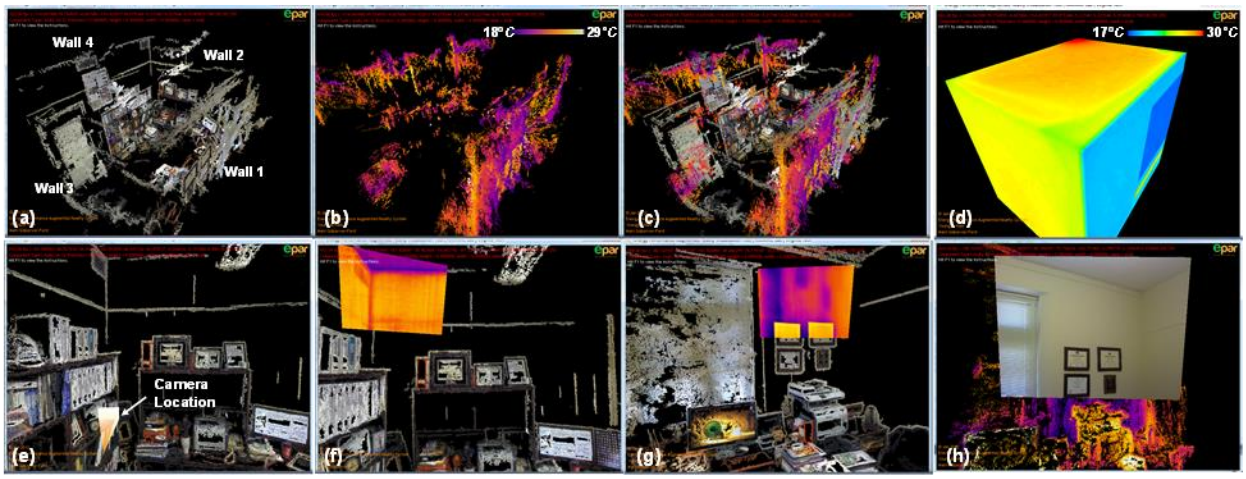

Figure 9.10 Actual and Simulated 3D Spatio-Thermal Models of IF#5 with 3D-registered Images

The EPAR environments are visually illustrated in Figure 9.11, 9.12, and 9.13 wherein the actual thermal performance models are registered with the simulated models. Subfigure (b), (c), and (d) of each figure present the actual and simulated thermal distribution of indoor surface from the same viewpoint. Each 3D point in the EPAR model acts as a temperature sensor which is documenting the as-is thermal profiles at the time the thermal images were captured. Each 3D point has its own RGB color value, and then it is directly converted into absolute temperature value based on given color spectrums for temperature scales. Thus, the actual and expected thermal performance of areas in a given building space can be intuitively compared with each other in the EPAR models, and then the deviations can be calculated.

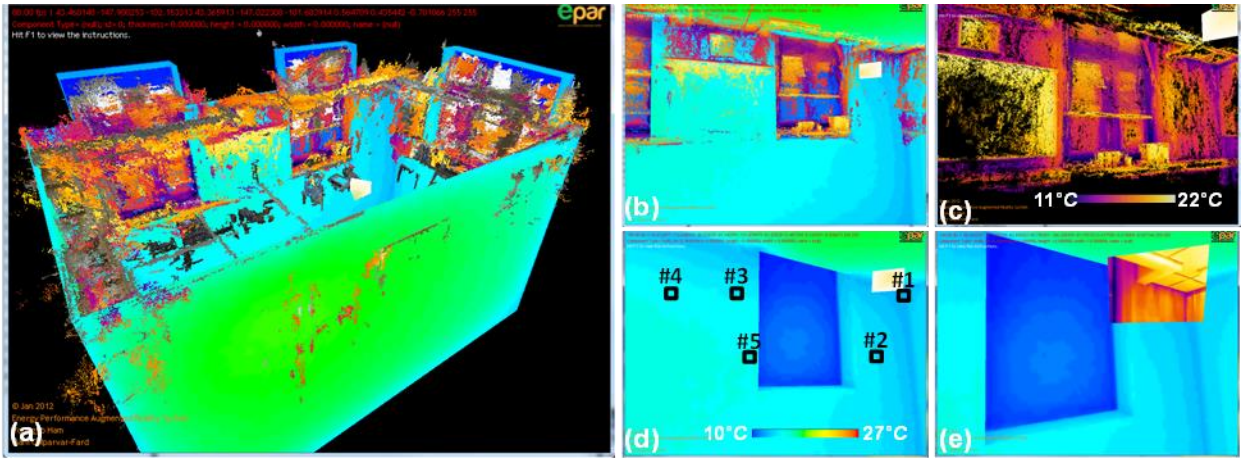

Figure 9.11 (a) EPAR Model of IF#2; (b) Integrated Visualization of Actual and Expected Thermal models of IF#2; (c) Actual 3D Thermal Model from the Same View Point Shown in (b); (d) CFD Model from the Same View Point; (e) CFD Model with a 3D-registered Thermal Image

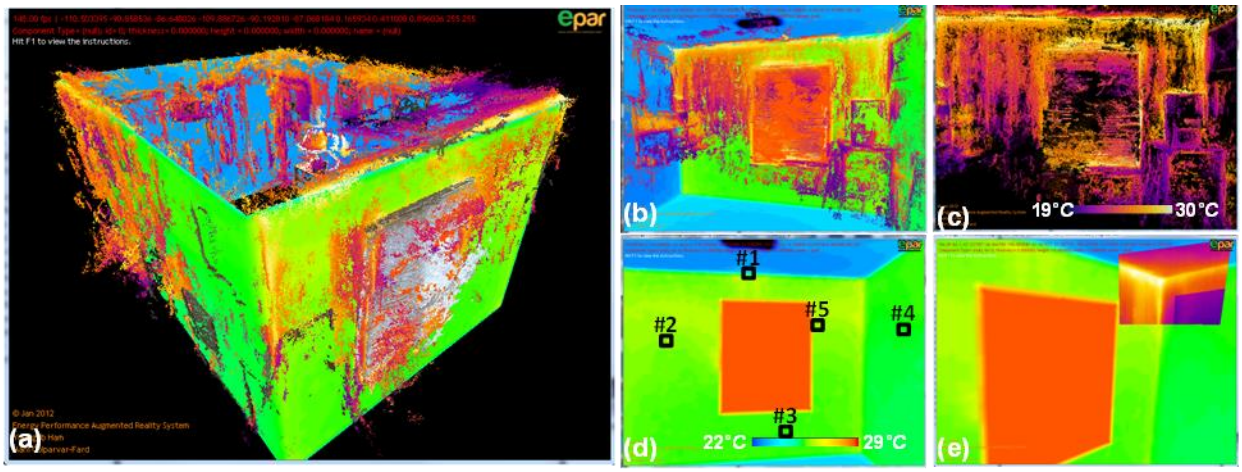

Figure 9.12 (a) EPAR Model of RB#3; (b) Integrated Indoor Visualization of Actual and Expected Thermal Models of RB#3; (c) Actual 3D Thermal Model from the Same View Point Shown in (b); (d) CFD Model from the Same View Point; (e) CFD Model with a 3D-registered Thermal Image

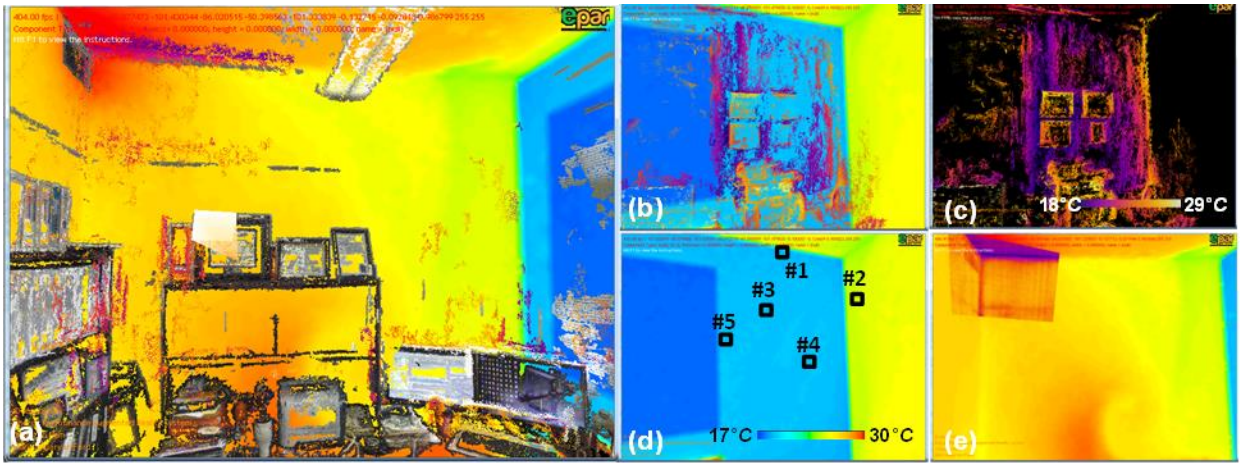

Figure 9.13 (a) EPAR Model of IF#5; (b) Integrated Indoor Visualization of Actual and Expected Thermal Models of IF#5; (c) Actual 3D Thermal Model from the Same View Point Shown in (b); (d) CFD Model from the Same View Point; (e) CFD Model with a 3D-registered Thermal Image

As a proof of concept, five surface areas in the generated EPAR models are selected and their actual and simulated thermal performances are compared between each other: an area in the corner of two intersecting walls, three flat regions on the building surface, and a flat area around a window. The locations of the selected areas are shown in Figure 9.11(d), 9.12(d), and 9.13(d). The temperature value for these areas were measured by averaging temperature values from all the 3D reconstructed points associated with the selected regions.

Table 9.6 Performance Deviations

IF#2	**Area 1**		**Area 2**		**Area 3**		**Area 4**		**Area 5**	
	μ	***σ***	***μ***	***σ***	***μ***	***σ***	***μ***	***σ***	***μ***	***σ***
Actual Measurement (°C)	11.1	0.13	14.6	0.08	14.4	0.05	14.3	0.05	14.5	0.04
Simulated Results (°C)	13.7	0.05	14.8	0.08	15.1	0.07	15.3	0.05	15.4	0.09
Deviations (°C)[+]	(2.26, 3.01)		(0.17, 0.46)		(0.49, 0.98)		(0.83, 1.25)		(0.59, 1.15)	
RB#3	**Area 1**		**Area 2**		**Area 3**		**Area 4**		**Area 5**	
	μ	***σ***	***μ***	***σ***	***μ***	***σ***	***μ***	***σ***	***μ***	***σ***
Actual Measurement (°C)	29.7	0.10	25.9	0.04	25.1	0.05	24.9	0.08	25.9	0.06
Simulated Results (°C)	26.4	0.04	26.3	0.06	25.9	0.06	25.3	0.02	26.1	0.09
Deviations (°C)[+]	(3.00, 3.59)		(0.13, 0.53)		(0.56, 1.00)		(0.21, 0.62)		(0.15, 0.48)	
IF#5	**Area 1**		**Area 2**		**Area 3**		**Area 4**		**Area 5**	
	μ	***σ***	***μ***	***σ***	***μ***	***σ***	***μ***	***σ***	***μ***	***σ***
Actual Measurement (°C)	20.4	0.13	24.7	0.04	21.1	0.18	20.9	0.24	20.3	0.1
Simulated Results (°C)	19.1	0.06	23.9	0.09	19.6	0.04	19.6	0.05	19.1	0.06
Deviations (°C)[+]	(0.88, 1.66)		(0.47, 1.03)		(1.03, 1.95)		(0.71, 1.88)		(0.87, 1.53)	

[+] $\Delta(\mu\text{-}2.05\sigma, \mu\text{+}2.05\sigma)_i$ where i is each section

Table 9.6 shows the results of comparing the measured wall surface temperature with the predicted simulation results. The performance deviations for each area are reported in forms of average temperature (μ) and its standard deviation (σ). The deviations between the actual and simulated values are reported with 96% confidence in measurement accuracy (i.e., μ±2.05σ). In the case of IF#2, a reasonable agreement can be found between the measured and simulated results. For the measurements in the areas 2 to 5, the average temperature deviation was 0.52-0.96°C. Due to typical inaccuracy of measurement and simulation, it is expected to have minor deviations. Hence, it is likely that the outcomes of the numerical analysis for the areas 2 to 5 were acceptable. However, the performance deviation for the area 1 was relatively higher compared to the other regions. For RB#3, for most areas except for the area 1, thermal profiles from the numerical analysis and the field measurements were approximately consistent. As shown in Table 9.6, the deviations for the area 1 was more significant compared to the others. In the case of IF#5, the average surface temperature deviation was 0.79-1.61°C. Overall, the performance of the CFD model on predicting the wall surface temperature was reasonable in the experiments. Although simulated temperatures were slightly over or under-estimated for most areas, several areas in both IF#2 and RB#3 have critical deviations. Such deviations indicate the need for more detailed diagnostics for the associated building areas.

Figure 9.14 presents the results of 3D thermal mesh modeling for automated calculation

of thermal performance deviations in EPAR models. Figure 9.14(a) and 9.14(b) show 3D building geometrical and thermal point cloud models, which enables auditors to better understand how thermal values are spatially distributed in the 3D building environment. Figure 9.14(c) and 9.14(d) present the 3D thermal mesh models that are generated from the actual thermal point cloud and the VRML-based CFD models for two case studies respectively. The mesh modeling improves the model completeness by extrapolating thermal performance for those areas that are sparsely reconstructed. Also, this process creates a uniformly dense point cloud model by sub-sampling from those areas that are densely reconstructed.

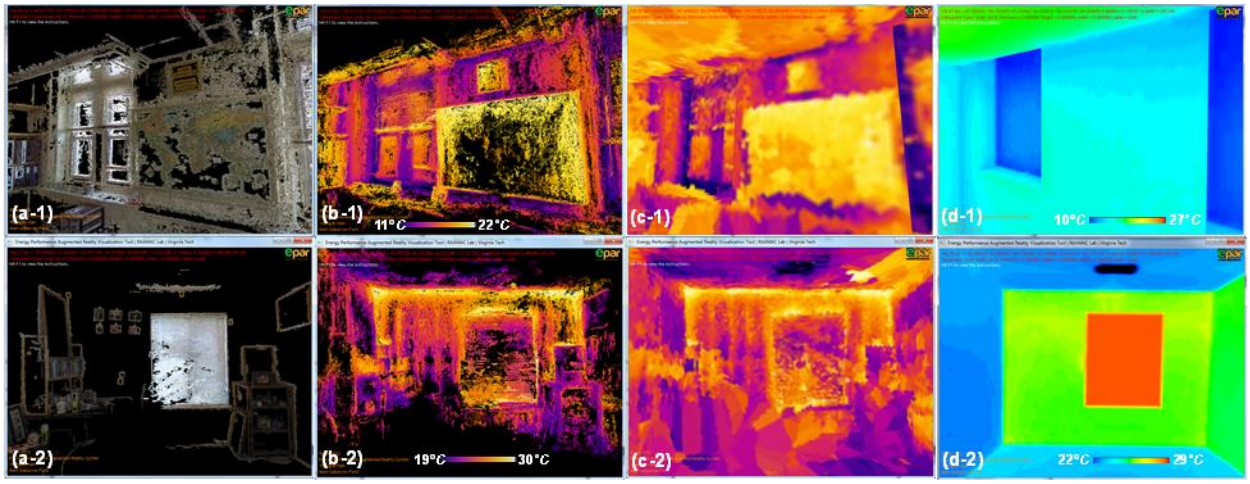

Figure 9.14 (a, b) 3D Building Geometrical and Thermal Point Cloud Models; (c) 3D Thermal Mesh Models; (d) VRML-based CFD Model (Simulated 3D Spatio-Thermal Models) (First Row: an Office Room in an Instructional Facility, Second Row: a Bedroom in a Residential Building)

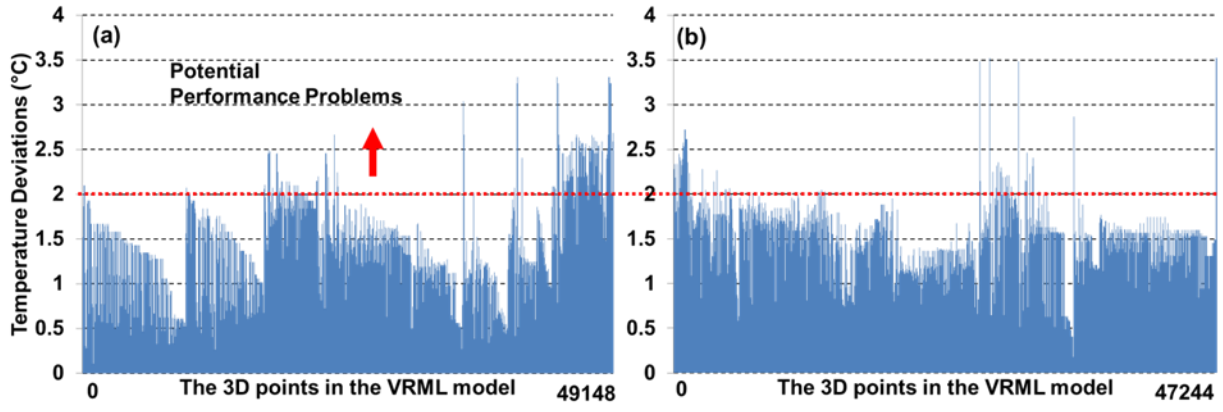

Figure 9.15 Distributions of Temperature Deviations at the Level of 3D Vertex in EPAR Models: (a) IF #2; (b) RB #3

In the camera calibration process, the re-projection errors for the thermal camera in x and

y directions were (0.08923, 0.154174) pixels, and the accuracy of measuring the focal length in x and y was (745.81701±3.85497, 743.10602±3.43616). In principal, due to the spherical shape of the LED light bulbs, the process of identifying the intersecting lines in a thermal calibration field may not be as accurate as the standard calibration process. Nonetheless, the registration errors in the conducted experiments seem negligible. The error in transforming the image-based 3D spatio-thermal models into the corresponding site coordinate systems is also calculated for different areas with different number of benchmarking points. These errors were reported in Table 9.5. In these experiments for solving the 7 DOF transformation between the two coordinate systems, more than three corresponding points are selected. In all cases, it is observed that these registration errors are within a reasonable practical range (<10 mm), which indicate that the proposed EPAR-based method is robust for performance comparison. Figure 9.15 shows the distribution of temperature deviations for both of case studies. As observed in this figure, for several areas, the simulation was slightly over or under-estimated in these experiments. Considering the errors on thermal measurement and the accuracy of the numerical analysis for modeling indoor thermal performance, the deviations between the actual and simulated thermal profiles seem to be negligible except for a few areas in case studies. As a proof of concept, the analysis was based on the assumption that deviations less than 2˚C can be considered negligible. This assumption is based on 1) the measurement accuracy of the FLIR E60 thermal camera; and 2) the recommendations made in (Fan and Ito 2012; Vera et al. 2010).

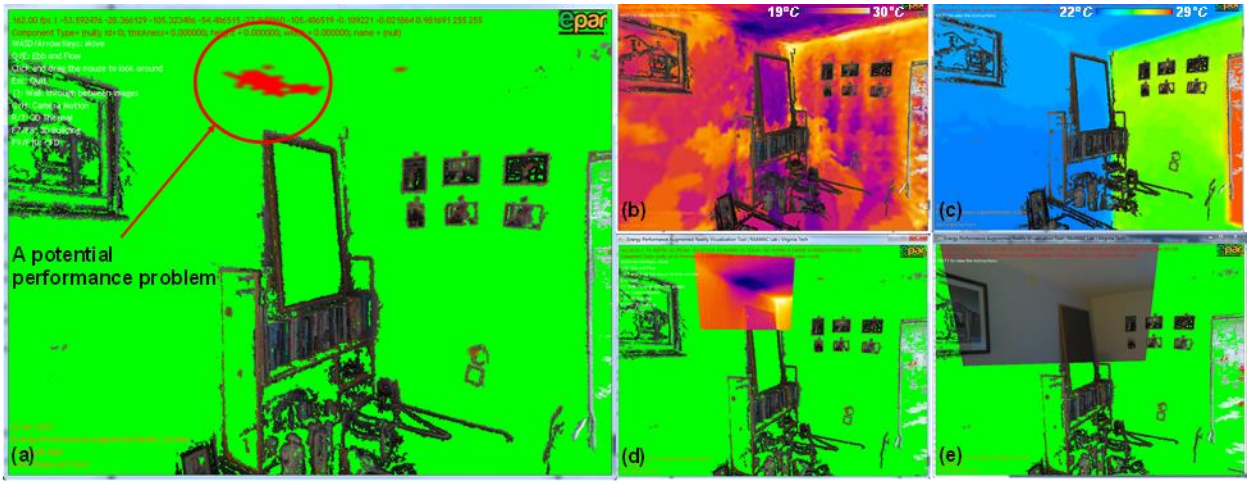

Figure 9.16 (a) Visualization of Potential Performance Problems along with a 3D Building Geometrical Point Cloud; (b) 3D Thermal Mesh Model of the Same Area; (c) VRML-based CFD Model of the Same Area; (d, e) Geo-registered Thermal and Digital Images

Based on such assumptions and the traffic light color metaphor, the areas with or without potential performance problems are color-coded with red and green colors respectively. Figure 9.16 (a) shows an example of the detected areas associated with potential performance problems. In the areas highlighted with the red color, the deviations between the actual temperature measurements (Figure 9.16(b)) and expected simulation (Figure 9.16(c)) are above the threshold. Considering the degradation level of the building in this case study (i.e., built in the beginning of the 1970s), such performance gaps may be caused by thermal performance problems. This may be primarily due to construction defects or degradation since the trends of the simulated and measured temperature profiles of the other areas comply well. Thus, the thermal deviations that are above the pre-defined threshold are able to pinpoint the locations of potential thermal anomalies and further better inform energy auditors about 'what areas require additional detailed diagnostics'. Additional intrusive diagnostics, perhaps partial destructions of these areas, may be required to find the source of irregular thermal performance and better analyze its impact on the energy efficiency of the building under inspection. Figure 9.16(d) shows the 3D-registered thermal image where the potential performance problem was observed. Through thermographic inspection of the 3D-registered thermal images in EPAR models, the detected potential performance problems can be further analyzed in detail. The geo-registered thermal image seen in Figure 9.16(d) further visualizes and qualitatively validates an example of a true positive detection. Here, the detected area is the section between a side wall and a ceiling around a HVAC system. Figure 9.16(e) shows the automatically 3D-registered digital image depicting the associated building geometrical characteristics. This geo-registered digital image represents the building semantics associated with defects captured in the thermal image, which can provide additional context information for potential performance problems in the buildings under inspection.

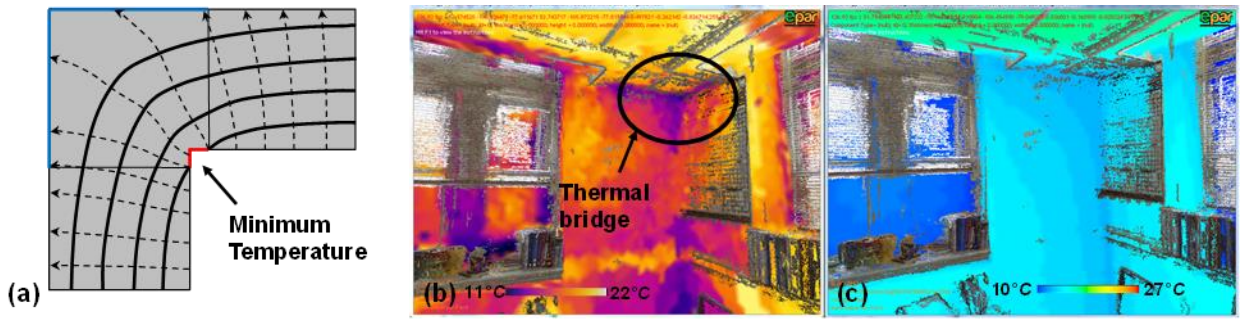

Figure 9.17 (a) Illustration of Geometrical Thermal Bridge in Building Environments; (b) Thermal Bridge Visualized in 3D Thermal Mesh Model; (c) VRML-based CFD Model of the Same Area

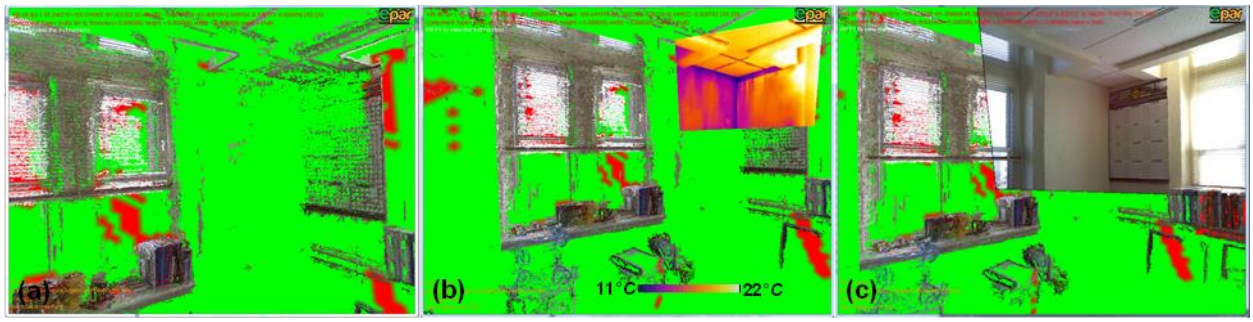

Figure 9.18 (a) 3D Visualization of Performance Deviation of the Area with a Geometrical Thermal Bridge; (b, c) Geo-registered Thermal and Digital Images

The heat transfer in orthogonal corners of a rectangular structure has recently brought more attention to irregular thermal phenomena which is named the thermal bridge (Martin et al. 2012). Figure 9.17(a) shows a graphical representation of the thermal bridge. When the heat flow in corner sections follows curved trajectories (i.e., the heat flux perpendicular to curved temperature contours), the temperature in the inner corners will be minimal. Analyzing thermal bridges is a critical step for building diagnostics since if the temperatures drop below the dew point temperature, the condensation can start along the associated wall surfaces. Such thermal bridges can be attributed to structural defects or the form of geometry itself. Given the heat flow from smaller interior spaces to larger outside areas and vice versa, geometrical thermal bridges can be located in any corner sections of building environments, even if they do not have any performance problems. Consequently during winter, the corner sections in buildings would always have a lower temperature compared to the adjacent flat areas. Thus, these typical and unavoidable thermal bridges should not be detected as potential performance problems if the temperature drops are acceptable. Qualitative analysis of building thermography representing geometrical thermal bridges will more likely result in wrong interpretations for less experienced energy auditors or homeowners in that all thermal bridges would be considered as performance problems. Figure 9.17(b) and 9.17(c) show the example of a thermal bridge detected in an instructional facility during winter and the expected thermal performance of the same area resulted from the numerical analysis respectively. As can be seen in Figure 9.18 (a) that represents the performance deviation, the thermal bridge was not detected as the potential performance problem in experiments. Thus, the thermal bridge in an office room of an instructional facility during winter is most likely a geometrical thermal bridge due to the rectangular geometry, not thermal defects. Figure 9.18(b)

and 9.18(c) show the 3D-registered thermal and digital images representing the same areas. Ultimately, by minimizing 1) the time and efforts to search for specific thermal images associated with potential performance problems and figure out 'where the thermal images are captured from'; and 2) the wrong interpretation of building thermography, the proposed method can facilitate building energy diagnostics. The proposed method can inspect very small surfaces with potential performance problems (i.e., in fact, at the vertex-level of a mesh). This level of granularity, for example, would be helpful when installing a blown-in loose-fill insulation is considered as one of the retrofit alternatives to improve the thermal resistance of the defected areas. However, if the defected areas are too small, retrofitting such problems is not likely to be practically feasible due to technical challenges and long payback period. Thus, it is noted that practical retrofit decisions need to be taken up to a certain minimum size of retroffitable surface. The proposed EPAR-based method choose not to dictate the minimum size of the retrofittable building area. Rather, by presenting the thermal performance deviations at the level of point in 3D, the system let building practitioners set their desired size when exploring the associated energy efficiency retrofit alternatives.

Table 9.7 Comparison with Prior Studies on 3D Thermal Modeling of Building Environments for Energy Saving

	Actual energy performance modeling		**Expected energy performance simulation**	**Identifying potential performance problems**
	Point cloud modeling:	**Mesh modeling:**		
EPAR v2.0	- Image-based method for spatial and thermal point cloud modeling	- Produces 3D thermal "mesh" models	Manual (generating the wireframe model)	Automatic
Wang et al. (2013)	- Laser scanner-based method for spatial modeling - Registers absolute temperature values to 3D point cloud model	N/A	N/A	N/A
Borrmann et al. (2013)	- Laser scanner-based spatial modeling - Maps color value from thermal image to 3D point cloud model	N/A	N/A	N/A
Lagüela et al. (2012)	- Semi-automatic image-based method for spatial and thermal point cloud modeling	N/A	N/A	N/A

Compared to prior works (Table 9.7), the proposed method benefits from a reliable benchmark for building performance analysis, which address the limitations of the current subjective and inconsistent thermographic inspection. Although manual process is required for initializing energy simulation, the proposed automated approach for generating 3D spatio-thermal mesh models and calculating the performance deviations from benchmarked models allows energy auditors to spend less time on finding performance problems from large amount of visual data by providing energy problem candidates; rather spend more time on looking at the performance problems to facilitate the associated energy efficient retrofit actions. The experimental results hold the promise that the proposed method can assist with reliable identification of potential building performance problems. Nonetheless, there are still a few scientific and practical challenges which remain as open research problems:

(1) Identification of a reliable threshold for inferring the presence of potential performance problems: For the purpose of determining if detected performance deviations indicate potential energy problems, the proposed method requires a reliable threshold which set by 2˚C in this research. Since the threshold is a function of errors in temperature measurement and energy simulation, it is not trivial to define a constant threshold that could be universally applied to all experiments. There is a need for further experimental examinations to identify how a reliable threshold can be robustly assigned for different experimental setup.

(2) Minimizing false positives and false negatives from the detected performance problems: Table 9.8 presents the false positive and false negative detections of the proposed method. Here, a false negative refers to an image representing an actual performance problem – detected during the manual inspection process – that the proposed inspection was not able to identify it. False positive indicates a false alarm in building thermography from the proposed inspection.

Table 9.8 False Positive & False Negative Detections of the Proposed Method

Performance metrics	IF #2	RB #3
# of thermal images containing false positive detections to the total number of thermal images	21/429	23/382
# of thermal images containing false negative detections to the total number of thermal images	0/429	9/382

As observed, a few false negatives are detected in the results from the case study of RB #3. These false negatives are due to the high value of the thermal threshold used for identifying potential performance problems. In addition, several false positives were detected in experiments. These false positives are mainly due to the presence of non-related objects in the scene. Figure 9.19 shows examples of these false positive detections. Here, the hanging clothes and the cork board were falsely detected as potential performance problems. More research needs to be conducted on developing computer vision-based techniques for segmenting objects from 3D reconstructed scenes and minimizing false positives in the process of identifying potential performance problems. Also, a more reliable thermal threshold needs to be identified for reducing false negative detections. This is particularly important as the number of false positive detections is more likely to significantly increase if the threshold is too low.

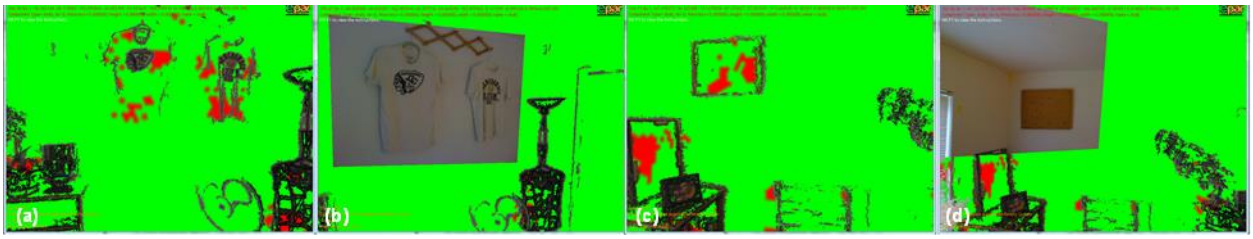

Figure 9.19 Examples of False Positive Detections in the Proposed Method

9.3.3 3D building condition assessment: measuring actual R-values and detecting condensation problems

The first five rows in Table 9.9 present the 3D thermal modeling metrics from the two case studies (RB#4 and IF#2). In both cases, the computational time is benchmarked on a regular engineering workstation (an Intel i7 960 core with 24GBs RAM and NVIDIA GeForce GTX 400), and reasonably detailed 3D mesh models are generated in each case. Table 9.9 also shows the environmental measurements, the range of the R-value measurements based on the average and standard deviation, and their notional values as well. When temperature deviations (e.g., between wall surfaces and crumped foils) used for calculating thermal resistances are too small (for Equation 14), accurate measurement using a consumer-level thermal camera would be challenging. To alleviate this issue, similar to (Madding 2008), a single device was used for measuring temperature differences, and thus the impact of the systematic error on the measurement was minimized in experiments.

Table 9.9 Experimental Results of 3D Thermal Modeling and Experimental Measurements

Item	Metrics	RB #4	IF #2
3D Thermal Modeling	# of 2D Thermal Images Registered	446	429
	# of 3D Thermal Points	3,042,350	2,838,478
	# of Vertices in Baseline Mesh Model (wall)	18,964	13,771
	# of Vertices excluding static occlusions in Mesh Model by using Threshold (wall)	17,297	7,740
	Computational Time for 3D Thermal Modeling	2hr 30min	2hr 21min
Environmental Measurements	Outside Air Temperature (°*C*)	5	3
	Indoor Air Temperature (°*C*)	28	24
	Dew Point Temperature (°*C*)	13.15	11.64
	Relative Humidity (%)	40	46
Calculated Metrics in 3D	Error on registration (mm)	8.69	9.30
	Average (μ) of R-values of Wall (m^2K/W)	0.753	0.833
	Standard Deviation (σ) of R-values of Wall	0.10207	0.14463
	Range of actual R-values by considering 95% confidence (μ-1.96$\sigma/\sqrt{n}$, μ+1.96$\sigma/\sqrt{n}$)	(0.75168, 0.75472)	(0.82986, 0.83631)
	Notional R-value of Wall (m^2K/W)	0.893	0.933
	Average (μ) of R-values of Window (m^2K/W)	0.260	0.274
	Standard Deviation (σ) of R-values of Window	0.00173	0.00211
	Range of actual R-values by considering 95% confidence (μ-1.96$\sigma/\sqrt{n}$, μ+1.96$\sigma/\sqrt{n}$)	(0.26011, 0.26027)	(0.2737, 0.27389)
	Notional R-value of Window (m^2K/W)	0.301	0.301

Figures 9.20, 9.21, 9.23, and 9.24 illustrate the distribution of the surface thermal profiles and the as-is thermal resistance measurements at the level of 3D point for wall assemblies and windows in RB#4 and IF #2 respectively. Compared to prior works (Albatici and Tonelli 2010; Dall'O' et al. 2013; Fokaides and Kalogirou 2011; Madding 2008) that leverage a single measurement of actual thermal resistance for each building assembly using a single or a few temperature data from building thermography, the proposed method can provide more detailed representation of the heat transfer conditions for building assemblies at the level of 3D point. Figure 9.22 and 9.25 show examples of visualizing the distribution of the R-values along with the associated building geometry in 3D. The 3D visualization of thermal resistances using different color gradients can provide an opportunity for building practitioners to easily and quickly understand the distribution of the actual thermal resistance in building environments. Because static occlusions are taken into account, the proposed method has potential for improving the accuracy of measurements. In both cases, the registration errors between 3D thermal point clouds and the geometrical baseline mesh are within a reasonable practical range (Table 9.9). Based on

the calculated registration errors as a geometrical distance threshold, it is observed that 8.8% (RB#4) and 43.8% (IF #2) of the 3D thermal points were related to non-relevant objects around walls (e.g., Figure 9.22 and 9.25 (b) and (c)). Thus, those thermal points are not considered when calculating the as-is thermal resistances in 3D. Although the proposed method attempted to minimize the impact of such static occlusions in building environments, false negatives still happen due to incomplete segmentation. Examples are shown as oval-shaped areas in Figure 9.22 and 9.25 (e), which causes unreliable thermographic inspection for those areas. Here, the proposed method can also be used for the purpose of commissioning new buildings in addition to retrofit purposes during the operational phase. Unlike occupied buildings, there is minimal occlusion during commissioning inspection. Here, the proposed method can inspect if the new building is operating as expected by the design.

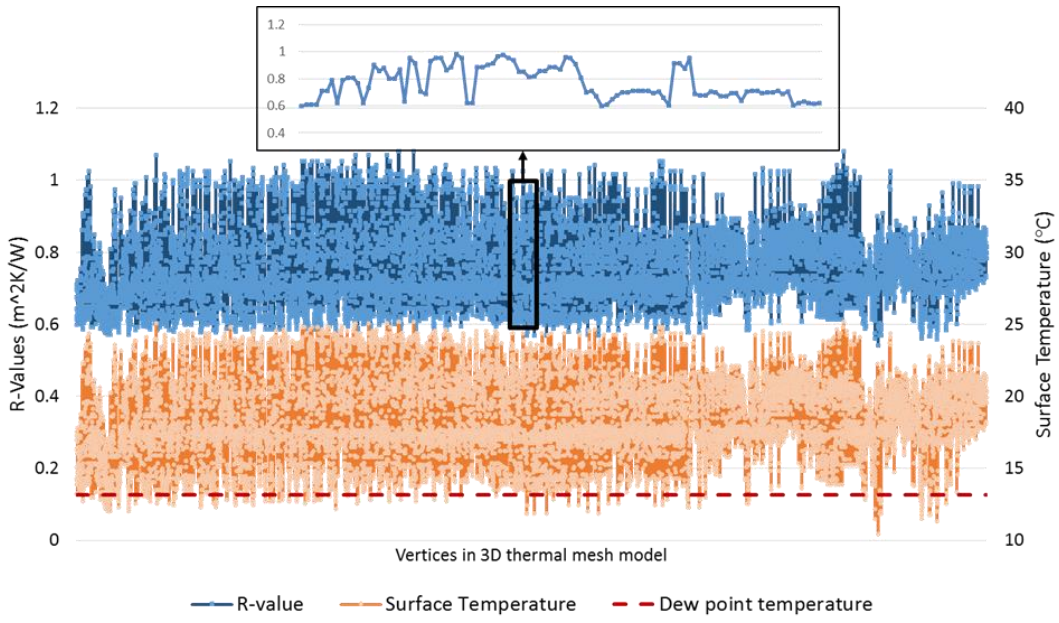

Figure 9.20 Point-level Distribution of Temperature and Actual R-values for the Wood Frame Walls in RB #4

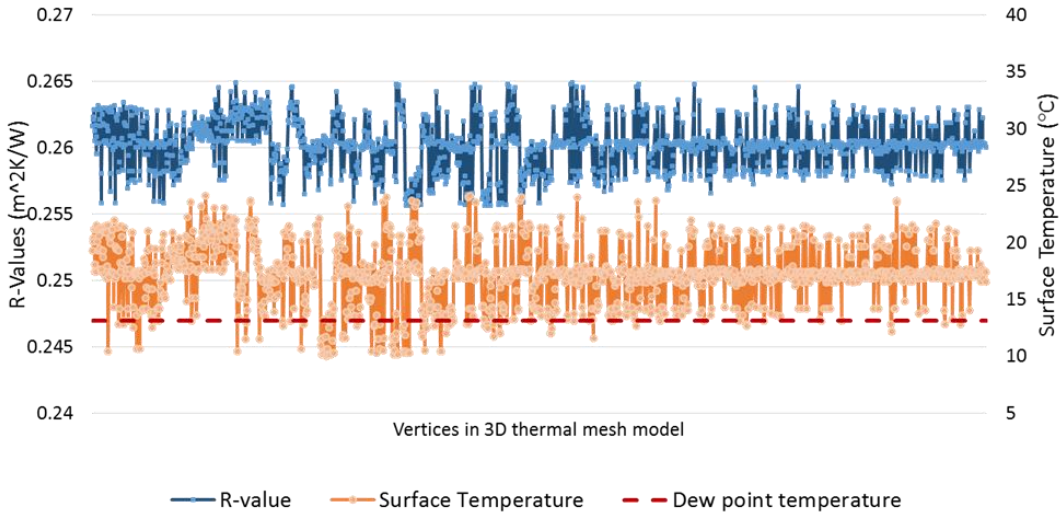

Figure 9.21 Point-level Distribution of Temperature and Actual R-values for the Single-glazed Clear Window in RB #4

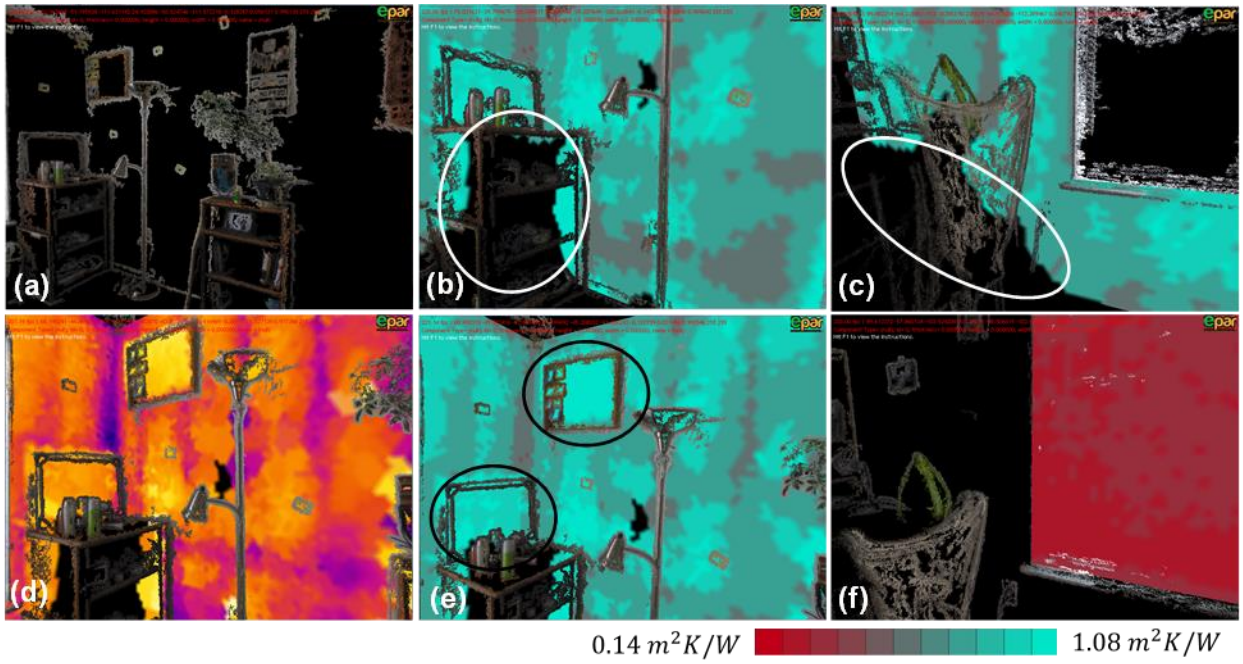

Figure 9.22 3D Visualization of R-value Distribution along with the Associated Building Geometry for RB #4

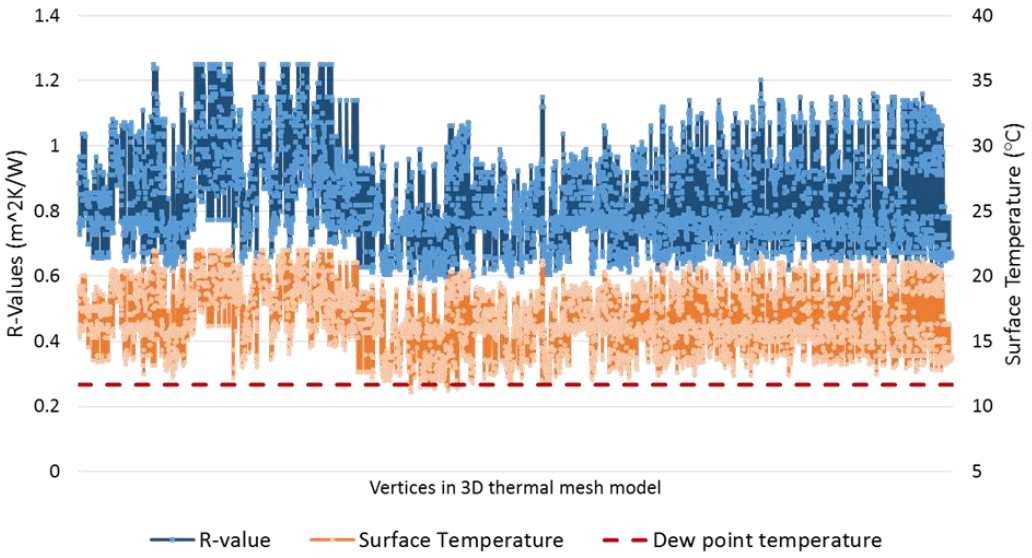

Figure 9.23 Point-level Distribution of Temperature and the Actual R-values for Concrete Masonry Walls in IF #2

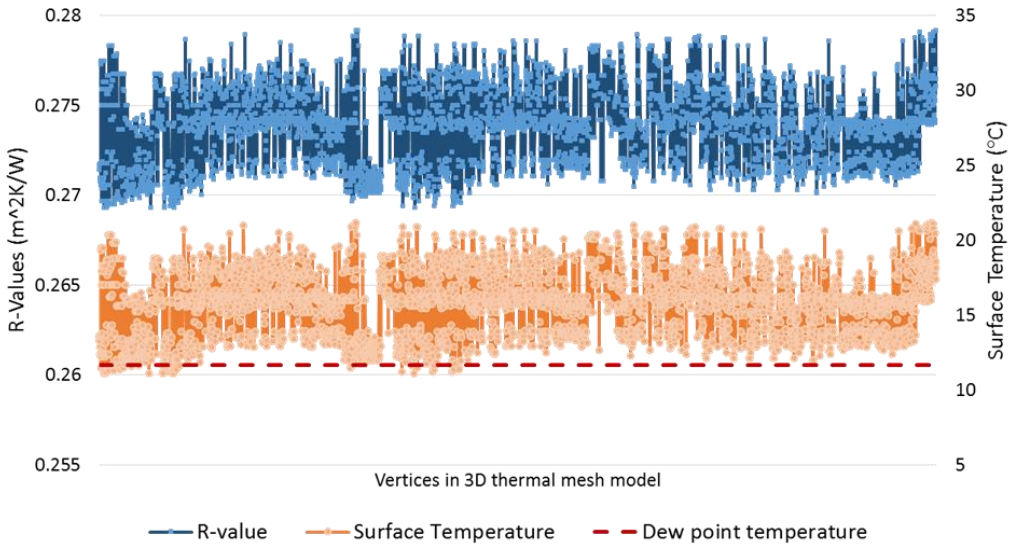

Figure 9.24 Point-level Distribution of Temperature and the Actual R-values for Single-glazed Clear Windows in IF #2

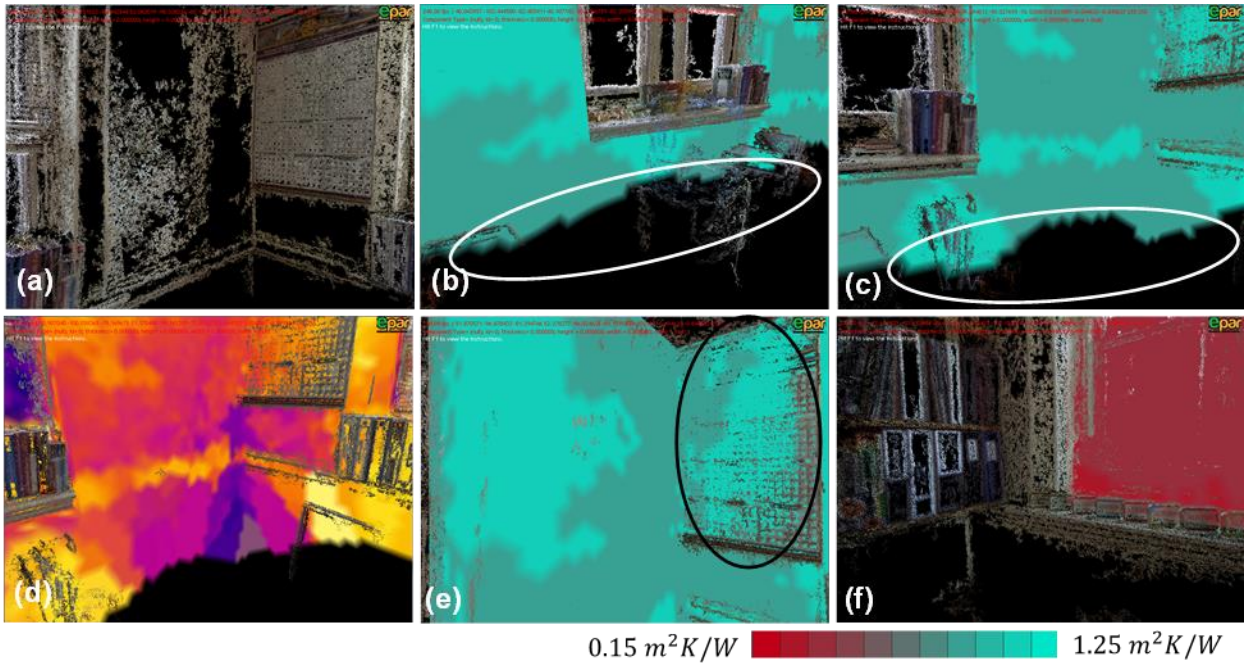

Figure 9.25 3D Visualization of R-value Distribution with the Associated Building Geometry for IF #2

Beyond providing surface thermal profiles in 3D, the proposed method can also improve the quality of interpreting building thermography by detecting and localizing moisture problems on building envelopes and visualizing the outcome in 3D along with the corresponding geometrical characteristics. Figures 9.20, 9.21, 9.23, and 9.24 illustrate the dew point temperature (dotted line) and the distribution of surface temperatures for both case studies. These figures demonstrate noticeable deviations between the two temperatures and further highlight the prominence of the point-based measurements. Compared to the built-in option available in current thermal cameras for detecting condensation problems (Hoff 2011), the proposed method has potential to improve the current practices by estimating the size of the building areas associated with condensation issues in a polygon mesh. In Figure 9.26, building surface areas that are likely to suffer from condensation issues are visualized in 3D ((a) in RB #4 ≅ 0.0046m^2, (b) and (c) in IF #2 ≅ 0.0159m^2). These results are consistent with visual observations conducted at the time of data collection. When thermal images were captured, the surface temperatures of those areas were lower than the dew point. As shown in both cases, the condensation issues typically starts from around windowsills. To minimize the impact of these detected condensation problems, homeowners can 1) reduce the dew point temperature by decreasing the relative humidity or the indoor air temperature; 2) replace or add new insulation layers to increase the surface temperature

on the areas where insulation layers have been missed or degraded; and finally 3) adjust the ventilation fan or better benefit from natural ventilation to increase the wind velocity around the problematic areas.

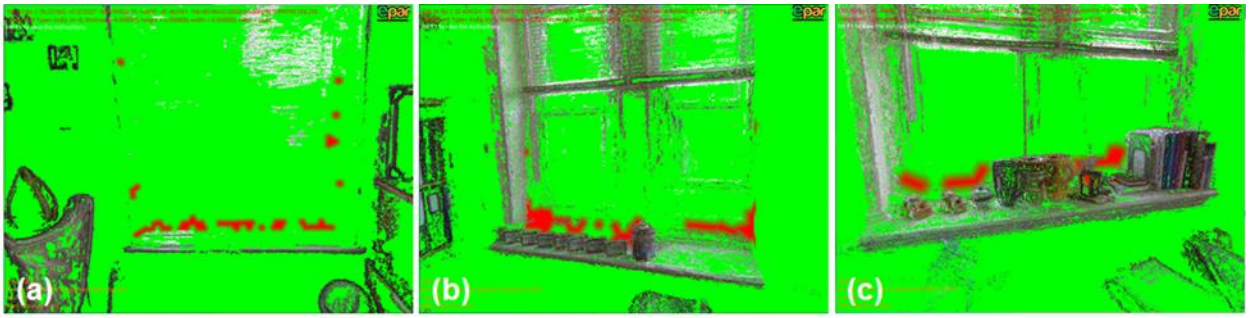

Figure 9.26 3D Visualization of Building Areas Identified with Possible Condensation Issues: (a) RB #4; (b, c) IF #2

The timing of an inspection would impact the capability of detecting condensation issues. To continuously monitor changes in the environmental conditions and study their impacts on condensation problems, one can place environmental sensors on building surfaces and continuously monitor the relative humidity and the surface and inside air temperatures. However, in practice, only a few environmental sensors could be placed per building element. As such, considering the variations of thermal performance over surface areas (e.g., large areas that contain thermal resistance non-uniformity), it is difficult to ensure if the surface condition measured by a few sensors is representative of the entirety of the building assemblies. Here, the proposed method has potential to provide a solution for selecting the proper locations of installing a limited number of environmental sensors. As a complementary step, after detecting any performance problems from the proposed one-time thermography-based method, the environmental sensors can be placed at the detected areas for continuous monitoring. This will allow proper positioning of a limited number of sensors and improve the efficiency of monitoring.

To discuss the perceived benefits of the proposed method, face-to-face and phone interviews were conducted with eleven domain experts. The subjects had 2 to 10 years of practical experiences in energy auditing of existing buildings. They were first asked about the current best practices and bottlenecks in thermographic inspections for energy diagnostics of existing buildings. All subjects responded that today thermography captured from existing buildings is considered the most effective tool for recording and communicating the as-is energy performance conditions to

building owners. However, thermography is primarily used for qualitative documentations in support of leveraging the Home Energy Rating System (HERS) for reporting purposes at a later stage. Most responders used the word "qualitative" to describe the current process. For example, they noted that "Audits can take a long time, up to several hours for large residential houses. IR imaging is done piece-wise through a building. It takes detailed documentation to know where each image was taken and what it is supposed to be showing. This can be confusing, and is often detrimental to the client's understanding, even with a good service provider explaining discoveries.", "Sometimes it is hard to tell where the thermal image is coming from in the building. Often, our audits last about 2-4 hours. In this time, it is hard to note which image was taken where within the building."

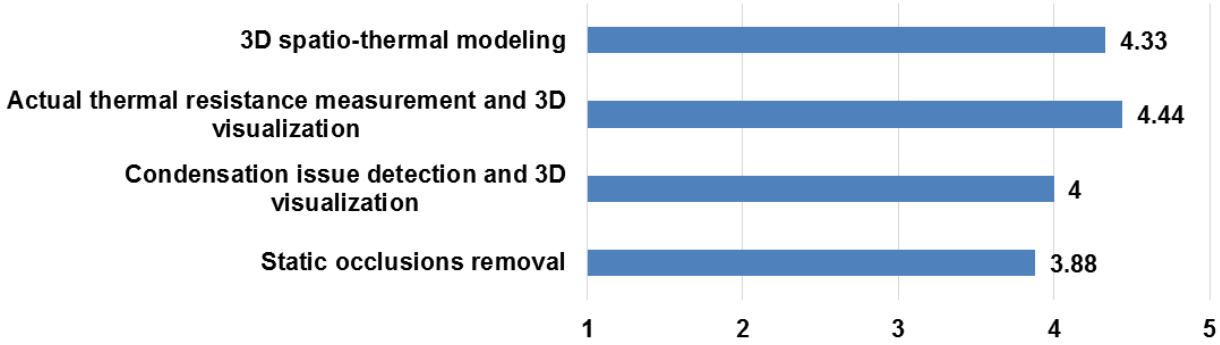

Figure 9.27 Domain Expert Survey Responses from the Likert Scale Questionnaires about the Usefulness of Each Module (1 = Poor, 5 = Excellent)

Figure 9.27 illustrates the summary of the responses from the Likert questionnaires on the usefulness of each module (1 = poor, 5 = excellent). As shown, participants generally felt that each features in the proposed method would be helpful for reducing the bottlenecks in current practices on thermography-based building condition assessment, e.g., "This is a very interesting step in the direction of recalling and identifying locations of leakage. This visualization tool will dramatically increase the potential for accurate assessments of issues.", "This visualization tool can be very efficient in detecting leaks in building insulation.", "In the summary, it would be useful to see an entire room in 3D to capture the proposed visualization tool's differentiating usefulness that cannot be done with 2D imaging."

The survey results show the potential of the proposed EPAR-based method for assessing the as-is building conditions as an intuitive communication tool. Since the main purpose of the

proposed method is to provide guidance for making efficient and effective energy retrofit decisions by diagnosing and visualizing the as-is building conditions, the proposed method only needs to be conducted once per regular building diagnostic process (e.g., annual building inspection) and does not need to be performed frequently. Hence, it does not add significant burden to building practitioners, and allows the proposed method to be repeatable in parallel with the thermographic inspection.

Despite such perceived benefits, several participants noted that there is still room for improvement to alleviate bottlenecks in current practices which are remaining open.

(1) Difficulty in in-situ measurement of as-is thermal properties for building assemblies using thermography: Few participants had concerns about the difficulty in accurate measurement of thermal properties in building environments by using thermography. Here, following prior works (Albatici and Tonelli 2010; Dall'O' et al. 2013; Fokaides and Kalogirou 2011; Madding 2008), the deviation between the measurements and the notional values was examined. Here, window components were selected for experiments. It is not a trivial task to accurately estimate the thermal properties of the old building assemblies such as the case studies of this research. Here, the estimation is based on (ColoradoENERGY 2013; The Engineering Toolbox 2013) which provide recommendations for such thermal resistances and (European Standard (EN) 1997). As a result for single-glazed clear windows, the averaged deviations were 12.81% (= (0.301-0.260)/0.301) for RB #4 and 10.37% (= (0.301-0.274)/0.301) for IF #2. Following the environmental assumptions presented in (Albatici and Tonelli 2010; Dall'O' et al. 2013; Fokaides and Kalogirou 2011; Madding 2008), the findings in the experiments were consistent with what was reported in the prior works. Here, systematic errors on the input variables for calculating the as-is thermal resistance need to be considered. If the thermographic inspection is conducted in outdoor environments, the measurement accuracy would be affected by various external factors such as wind, sun radiation, and shadows. Since the temperatures are measured from inside surfaces and crumpled aluminum foils located at indoor environments, the accuracy of measuring those input variables is typically the same as it is claimed in the technical specification of the thermal camera. As can be seen in Table 9.1, the measurement accuracy of the thermal camera used is 2°C or ±2% of reading. Here, another prevalent challenge for accurate measurement in thermal resistances in a non-destructive manner is that the measurement needs to be conducted under steady-state conditions. Despite significant efforts to form a steady-state heat transfer

condition during thermographic inspection (e.g., the timing of data collection and experimental setups prior to image data collection), in practice, it is not trivial to maintain a perfect steady-state condition during thermogaphic inspection. More research needs to be conducted on how a steady state condition of heat transfer can be maintained during thermographic inspection and how the measurement errors caused by non-steady-state conditions can be accounted for more accurate analysis.

(2) Continuous measurement to form time-series of thermal resistances: Besides the measurement accuracy issues, a few responders described '4D visualization' as a desired feature, e.g. "Maybe a 4D visualization done with the presence of all the objects that exist in the building.", "A time series IR webcam of a building over the course of a year." In prior work on measuring actual U-values (Fokaides and Kalogirou 2011), the results were validated based on different sources of information: instantaneous surface temperature data samples of 10 measurements obtained from building thermography and continuous time-series heat flux data collected from HFMs over a period of 168 hours. According to their experimental results, it is shown that the outcomes of the two methods were very close to each other in terms of their accuracy. However, if surface temperature data can be collected continuously, the as-is thermal resistances can be modeled and explored in 4D (3D+time) as opposed to static representation. Visualizing dynamic energy performance metrics in form of 3D animation can significantly improve the understanding of time-varying heat transfer phenomena for practitioners. More research on 4D visualization of energy performance metrics inspired by 3D thermography need to be conducted.

9.3.4 3D thermography-based method for cost analysis of energy efficiency building envelope retrofits

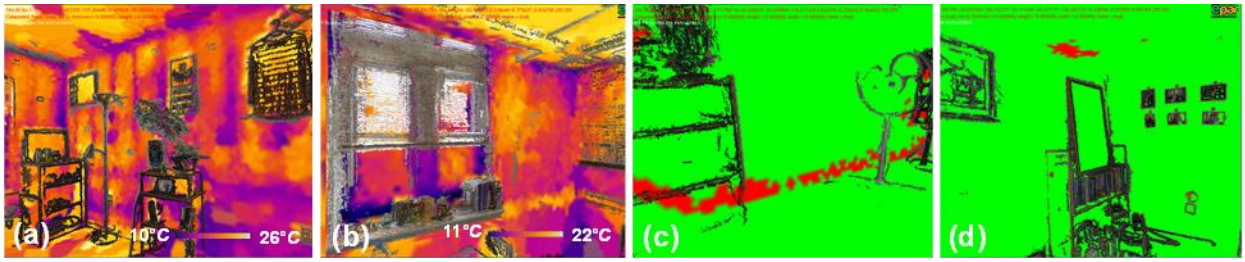

Figure 9.28 (a) 3D Thermal Mesh Model along with the Building Geometrical Point Cloud in RB #4; (b) Same Metrics in IF #2; (c, d) Potential Thermal Defects (red-colored) Detected in EPAR Models

Figure 9.28 illustrates 3D thermal mesh models for two real-world cases and examples of

the building areas associated with potential thermal anomalies inferred from thermal performance deviation in EPAR models. Given the temperature measurement errors of a consumer-level thermal camera and the accuracy of simulating building thermal performance using the numerical analysis method, slight deviations between actual and expected surface temperatures are expected. Considering the measurement error of a FLIR E60 thermal camera, and the acceptable error of simulating indoor building environments (Fan and Ito 2012; Vera et al. 2010), it is assumed that building areas associated with < 2˚C of thermal deviations is considered as a false alarm and can be neglected to infer the presence of potential performance problems. The building areas associated with potential thermal performance problems were calculated in the EPAR models as 0.94m^2 and 0.83m^2 for RB #4 and IF #2 respectively. For IF #6, a hypothetical scenario is applied that the thermal resistance of the entirety of the wall assembly needs to be improved to the recommended value. Here, the detected areas represent examples of typical candidates relevant to thermal performance issues such as surface areas between a side wall and a floor adjacent to the exterior (Figure 9.28(c)) and between a side wall and ceilings around the heating system (Figure 9.28(d)) in old buildings.

Here, installing blown-in loose-fill insulations is considered as an example of insulation retrofit alternatives for the finished walls. Because the bid cost for installing insulations varies on a contractor-by-contractor basis, according to (Bynum 2000; U.S. DOE 2012), a range for the expected cost of installing loose-fill insulations is estimated (Ham and Golparvar-Fard 2014). Table 9.10 shows the range of the direct costs estimated for installing the loose-fill insulations for RB #4. To estimate the material cost, the expected waste of loose-fill insulation materials during the installation process is considered as well. Given the small scope of the insulation installation required for the case studies, the overhead and profit cost were not considered in estimations.

Table 9.10 Estimated Cost for Installing Blown-in Loose-fill Insulation (RB #4)

Items	Cost Estimation	
	lower bound	upper bound
Mid-grade loose-fill insulation material (e.g., cellulose, fiberglass, or Rockwool) for 1.11 m^2	$2.35	$3.46
Labor to install loose-fill insulation for 2 hours	$88.93	$88.93
Special equipment used for blowing in material for 2 hours	$30.00	$48.75
Supplies (e.g., vent flow baffles, fasteners, and sealing tape) for installing and finishing loose-fill insulation for 0.92 m^2	$0.48	$20.00
Total direct cost	$121.75	$161.13

In order to study the impact of different climates on the expected energy cost savings, several additional locations are hypothesized for the two real-buildings located in Virginia: 1) Case #4: assuming RB #4 is located in Minnesota; 2) Case #5: assuming RB #4 is located in Florida; 3) Case #6: assuming IF #2 is located in Minnesota; and finally 4) Case #7: assuming IF #2 is located in Florida. In these experiments, the retail price for electricity and natural gas and 'heating and cooling degree days' statistics at each building location are obtained from (U.S. Energy Information Administration 2013; U.S. Energy Information Administration 2013) and (The National Oceanic and Atmospheric Administration (NOAA) 2013) respectively.

Table 9.11 Quantifying Energy Saving Cost from Building Envelope Insulation Retrofit under Different Environmental Conditions

	Type of Space Conditioning	Source of Energy	Retail Price of Energy[+] (per kWh)	Degree Days[++]	Expected Saving Cost (per year)	Total Saving Cost (per year)
RB #4	Heating	Natural gas	$0.069	3734	$21.0	$33.34
	Cooling	Electricity	$0.116	1326	$12.34	
IF #2	Heating	Electricity	$0.081	3734	$14.27	$18.72
	Cooling			1326	$4.45	
IF #6	Heating	Electricity	$0.081	3734	$32.13	$40.17
	Cooling			1326	$8.04	
Case#4	Heating	Natural gas	$0.038	7220	$23.94	$31.96
	Cooling	Electricity	$0.127	713	$8.02	
Case#5	Heating	Natural gas	$0.076	533	$3.2	$36.38
	Cooling	Electricity	$0.113	3579	$33.18	
Case#6	Heating	Electricity	$0.101	7220	$36.0	$39.29
	Cooling			713	$3.29	
Case#7	Heating	Electricity	$0.093	533	$2.26	$16.99
	Cooling			3579	$14.73	

[+] The retail prices of natural gas and electricity obtained from the U.S. Energy Information Administration (2013)

[++] Degree days statistics in 2012 obtained from the National Oceanic and Atmospheric Administration (2013)

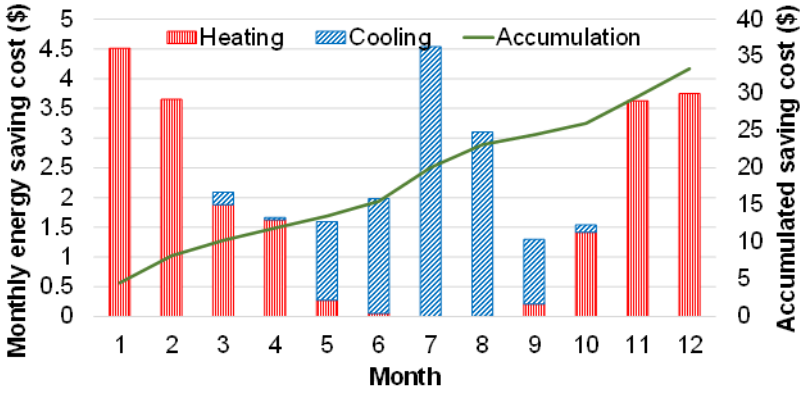

Figure 9.29 Monthly and Accumulated Cost for Expected Energy Saving by Installing Blown-in Loose-fill Insulation in RB #4. Target R-value: 2.64m^2K/W

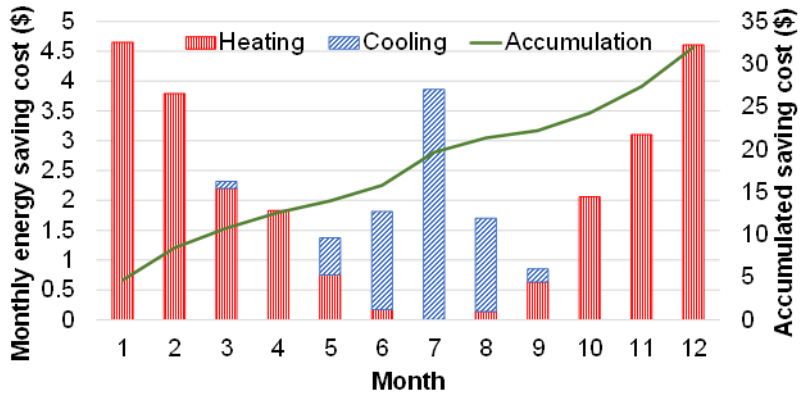

Figure 9.30 Monthly and Accumulated Cost for Expected Energy Saving by Installing Blown-in Loose-fill Insulation in RB #4 Located in Minnesota (Case #4). Target R-value: 3.7m^2K/W

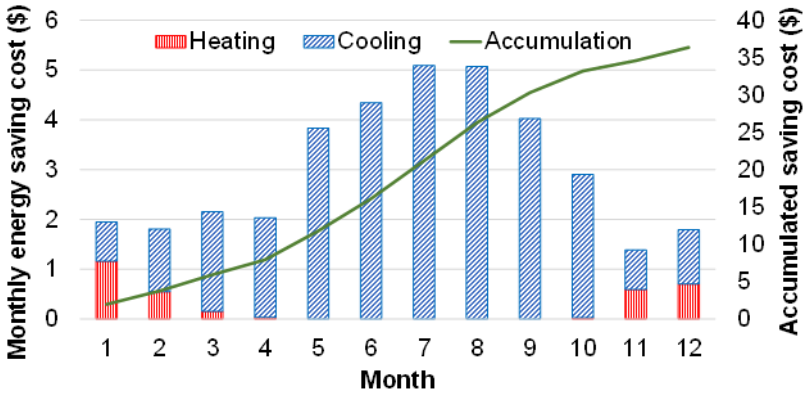

Figure 9.31 Monthly and Accumulated Cost for Expected Energy Saving by Installing Blown-in Loose-fill Insulation in RB #4 Located in Florida (Case #5). Target R-value: 2.29m^2K/W

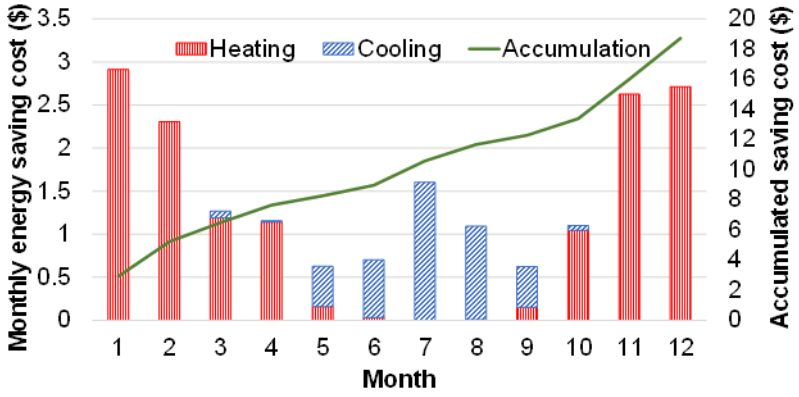

Figure 9.32 Monthly and Accumulated Cost for Expected Energy Saving by Installing Blown-in Loose-fill Insulation in IF #2. Target R-value: 2.64m^2K/W

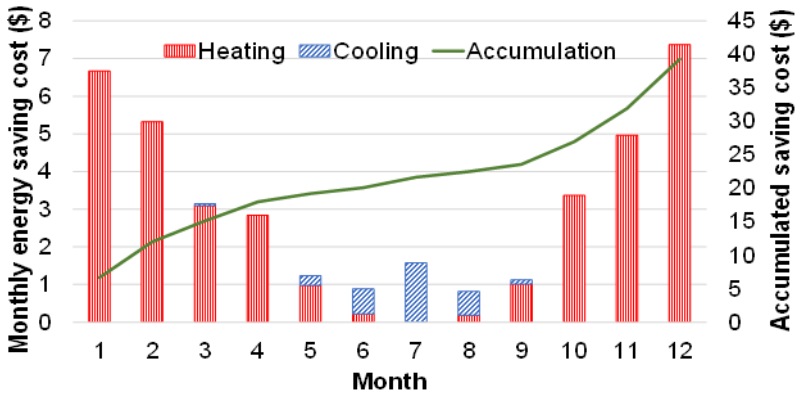

Figure 9.33 Monthly and Accumulated Cost for Expected Energy Saving by Installing Blown-in Loose-fill Insulation in IF #2 Located in Minnesota (Case #6). Target R-value: 3.7m^2K/W

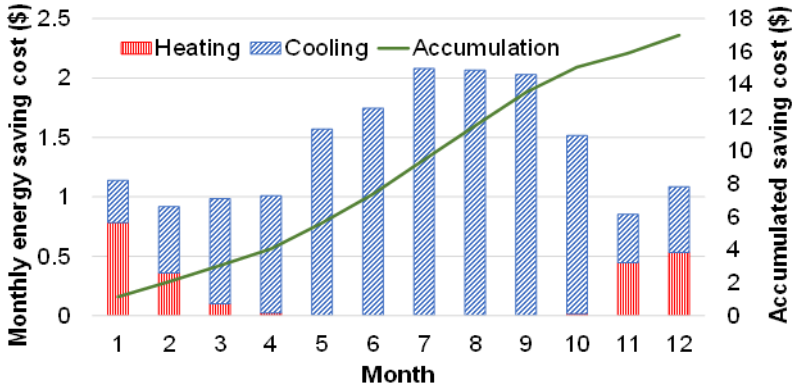

Figure 9.34 Monthly and Accumulated Cost for Expected Energy Saving by Installing Blown-in Loose-fill Insulation in IF #2 Located in Florida (Case #7). Target R-value: 2.29m^2K/W

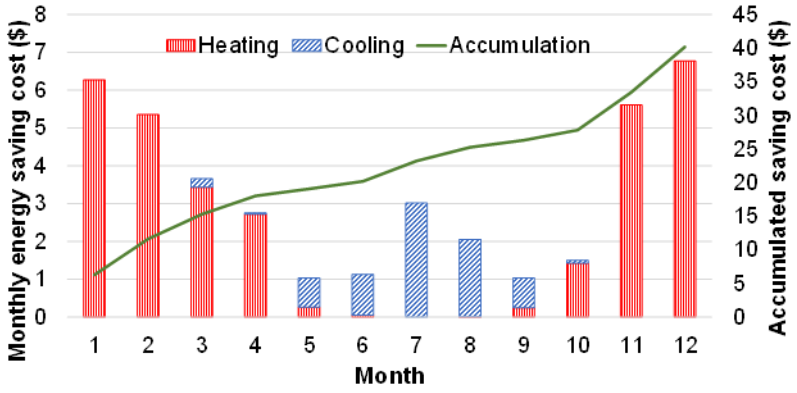

Figure 9.35 Monthly and Accumulated Cost for Expected Energy Saving by Installing Blown-in Loose-fill Insulation in IF #6. Target R-value: 2.64m^2K/W

Figure 9.29 to 9.35 illustrate monthly (bar) and accumulated (line) energy saving cost from installing loose-fill insulations in the building assemblies where potential thermal performance problems exist. These energy costs represent the difference in the amounts of heat transfer between inside and outside of the buildings under the following two different conditions: 1) when the buildings suffer from potential thermal performance problems; and 2) when the insulation level of the building areas associated with the defects is improved to those recommendations by the U.S DOE and the IECC. Due to the different level of the R-value recommendation for exterior walls: Minnesota: 2.29~3.7m^{2}K/W, Virginia: 2.29~2.64m^{2}K/W, Florida: 2.29~2.64m^{2}K/W, and the different 'heating and cooling degree days' statistics depending on the climate, noticeable variations are observed in the trends of the expected energy cost saving from installing insulations. As can be seen in Table 9.11 and Figures 9.31 and 9.34, due to a mild climate of Florida – low heating degree days and high cooling degree days – in contrast with Virginia or Minnesota, it is observed that the buildings in Florida (Case #5 and #7) are anticipated to save more energy for space cooling by improving the thermal resistances of building enclosures. Unlike electricity, the retail price for natural gas is typically calibrated based on the different climate of the region, and as a result, the retail price for natural gas in Minnesota tends to be cheaper than that of Virginia or Florida (Table 9.11). Moreover, the retail price of natural gas is generally less expensive than that of electricity. Accordingly, in the case of the buildings that utilize natural gas for heating purposes (RB #4, Case #4, and Case #5), the difference between the expected energy savings at different locations is trivial (RB #4: $33.34/year, Case #4: $31.96/year, Case #5: $36.38/year) even though the buildings located in Minnesota have much higher heating

degree days due to the colder climate during the winter season. As can be seen in Table 9.11 and Figures 9.32 to 9.34, if the building utilizes the electricity for both heating and cooling purposes, it is quantitatively verified that the expected energy cost savings from insulation retrofit are generally higher when the buildings located in the cold climates where higher R-value are expected (IF #2: $18.72/year, Case #6: $39.29/year, Case #7: $16.99/year). Ultimately, balancing the expected benefits from the various retrofit scenarios against the estimated cost for installing insulations (e.g., Table 9.10) provides building practitioners with thermography-based guidance for a better standing point to analyze energy efficiency building envelope retrofit alternatives. Based on the results of three real-world diagnostic cases and additional four hypothetical cases in different locations within the U.S., how the proposed method can analyze the impact of different environmental conditions such as climate on energy cost savings is discussed. In contrast to prior works for cost analysis, the proposed method leverages 1) the automated identification of potential performance problems based on performance deviations and the inclusive measurement of as-is heat transfer conditions for the associated building assemblies at the level of vertex in EPAR models; and 2) the R-value recommendations and 'degree days' statistics reflecting historical energy load required for space conditioning.

Yet, there are still a few research challenges that remain open including the issue on uncertainty in estimating the expected future monetary benefit. If the estimated monetary benefits from retrofitting the energy problems outweigh the costs incurred for retrofits, homeowners are more likely to invest in energy efficient retrofits. However, there are several uncertainties in predicting the future monetary benefits from retrofit investment, which include the propensity of building occupants for energy saving, fluctuations in energy prices or tax incentives, and the unexpected building performance after retrofits. For instance, if building occupants have negative propensity for energy saving, no matter how energy-efficient buildings are after retrofits, the monetary benefit from the retrofits could be smaller than the initial estimations. In addition, the extreme weather conditions beyond the recorded 'degree days' statistics can directly impact on the amount of heat transfer through building envelopes and in turn cause an increase or decrease in the actual energy cost saving compared to the predicted values. The lack of guarantees in monetary benefits may make homeowners reluctant in considering building retrofits. Although few uncertainties still exist in the proposed method, yet compared to auditors' qualitative and subjective recommendations or offhand calculations based on historical cost data of potential energy cost

savings for different upgrade measures, the proposed method has potential to provide a better standing point for sustainable retrofit decision-makings. Beyond estimating the cost associated with retrofitting energy problems based on the retrofit scenarios, more experiments on real retrofit cases need to be conducted for understanding and modeling various uncertainties in financial feasibility analysis of energy efficiency building envelope retrofits alternatives

9.3.5 Mapping the as-is thermal property measurements to BIM elements for reliable BIM-based energy analysis of existing buildings

The baseline gbXML files for case studies in this research were generated directly from pre-existing BIM files that were modeled in Autodesk Revit. The assumption is that the underlying BIM is modeled at the desired level of abstraction (LOD: Level of Development) for energy modeling and analysis purposes. When exporting gbXML file from BIM, due to the restrictions of the current building energy performance simulation tools in terms of the type of their input parameters, simplifications are applied to building information such as geometric design through limited approximations. Figure 9.36 shows the relevant parts of BIM for case studies together with the material layer set information for exterior building wall assemblies.

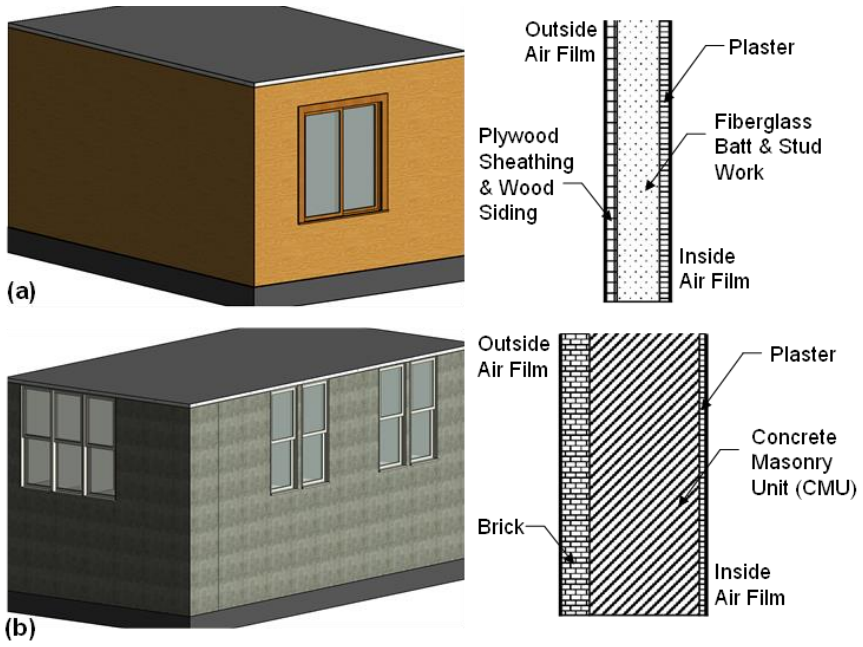

Figure 9.36 Building Information Models (BIM) and Material Layer Sets of Wall Assemblies adjacent to Exteriors: (a) RB #4; (b) IF #2

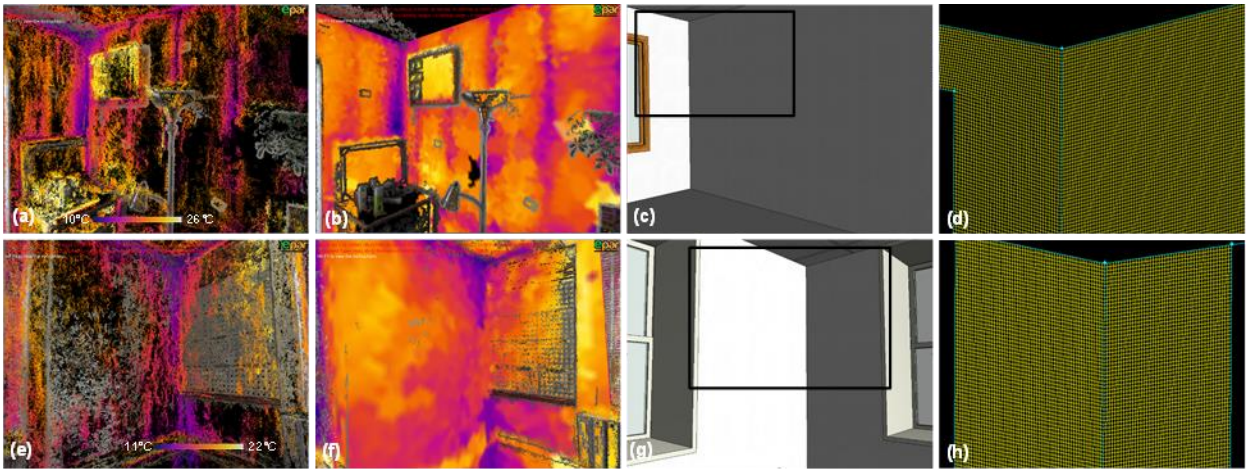

Figure 9.37 3D Thermal Modeling of Building Environments and BIM from the Same Viewpoint: (a) 3D Spatio-Thermal Point Cloud Models; (b) 3D Spatio-Thermal Mesh Models; (c) Building Information Models (BIM); (d) the Associated Building Areas in Meshed BIM (Top and Bottom Rows: RB #4 and IF #2 Respectively)

Figure 9.37 illustrates the 3D spatio-thermal models and BIMs for two different existing building environments. The resulting 3D thermal profiles are fed into the step for measuring actual thermal resistances of the associated building assemblies at the level of 3D point.

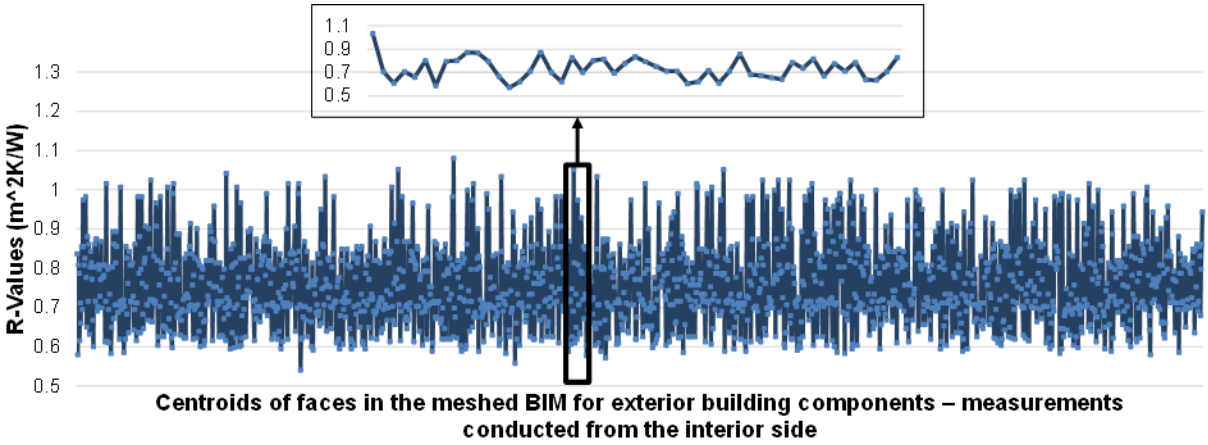

Figure 9.38 Distribution of Thermal Resistances Measurements for Exterior Walls in Meshed BIM for RB #4

Figure 9.38 shows the distribution of the actual thermal resistance measurement of wall assemblies at the level of vertex in meshed BIM. As shown, the as-is thermal resistance measurements are lower than the recommended level for newly constructed buildings (ENERGY STAR 2013) since these measurements reflect the as-is condition of the existing residential

building. To be more specific, this building constructed in early 1970's has not been strongly insulated, and the thermal resistance of the exterior building elements has also been degraded over time. Using different color gradients and with the corresponding building geometry in form of 3D point cloud, Figures 9.39(b) and 9.40(b) visualize the vertex-level distribution of the as-is thermal resistance measurements for the exterior wall assemblies in RB #4 and IF #2 respectively. The 3D visualization allows building practitioners to understand the heat transfer condition of building envelopes reflecting the as-is building condition in detail. When insulating techniques for small areas such as injecting loose-fill insulation in the cavities of a part of an existing building's façade are considered, the benefits of the 3D visualization will be magnified because determining where to improve thermal resistances can be a more complex decision than homeowners realize.

Once the as-is thermal resistance of building assemblies are calculated at the level of 3D vertex, a single R-value is derived for the corresponding BIM elements, which is in form of an input of current building energy performance analysis tools. Figure 9.39 and 9.40 visually illustrate the changes in the thermal resistances of the building assemblies in both cases. Figure 9.41 shows the relevant part (i.e., the element 'Construction') of the gbXML file that is automatically updated by using the proposed method. Through BIM-based energy performance analysis using the updated BIM as an input, building practitioners are more likely to reliably model and analyze the energy performance and thermal loads and predict the associated energy consumption and energy cost savings from different retrofit alternatives.

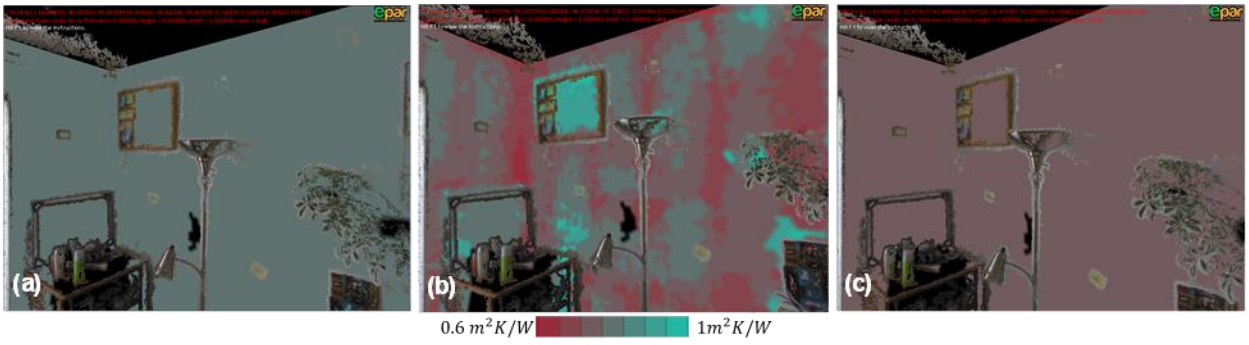

Figure 9.39 Visualization of Changes in Thermal Resistances with the Corresponding Building Geometry for RB #4: (a) Notional Value; (b) Distribution of Actual Thermal Resistances in Meshed BIM; (c) Weighted Average of Thermal Resistances

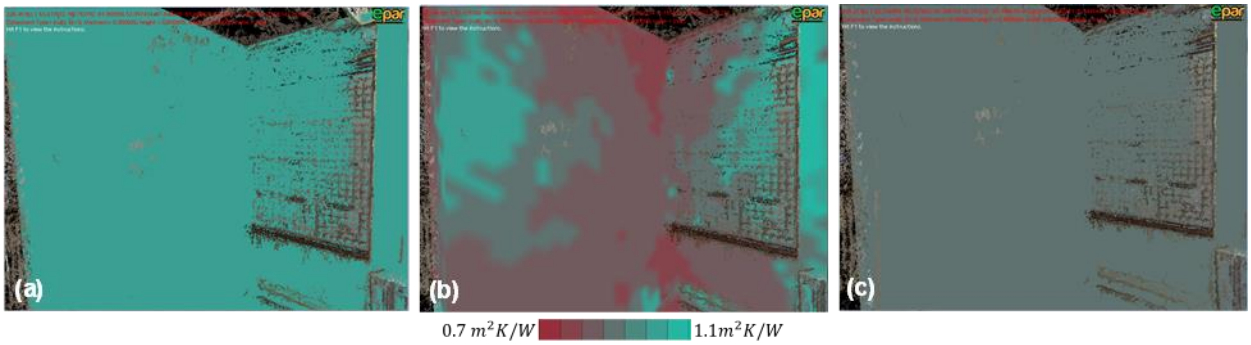

Figure 9.40 Visualization of Changes in Thermal Resistances with the Corresponding Building Geometry for IF #2: (a) Notional Value; (b) Distribution of Actual Thermal Resistances in Meshed BIM; (c) Weighted Average of Thermal Resistances

```
<Construction id="cons-1">
    <Name>Basic Wall: Generic - 6"</Name>
    <U-value unit="WPerSquareMeterK">1.120062</U-value>
    <Absorptance unit="Fraction" type="ExtIR">0.700000</Absorptance>
    <Roughness value="Rough">
    </Roughness>
    <LayerId layerIdRef="lay-cons-1">
    </LayerId>
</Construction>
```

(a)

```
<Construction id="cons-1">
    <Name>Basic Wall: Generic - 6"</Name>
    <U-value unit="WPerSquareMeterK">1.3277</U-value>
    <Absorptance unit="Fraction" type="ExtIR">0.700000</Absorptance>
    <Roughness value="Rough">
    </Roughness>
    <LayerId layerIdRef="lay-cons-1">
    </LayerId>
</Construction>
```

(b)

Figure 9.41 The Element 'Construction' in the (a) Pre-existing and (b) Updated gbXML-based BIM for RB #4

As illustrated, the proposed method enables an energy simulation engine for thermal load calculations to use actual thermal properties of BIM elements reflecting the as-is building conditions, rather than using the notional properties typically declared in the material specifications or industry standard databases (e.g. ASHRAE data) available in current BIM-authoring tools. This allows the BIM-based energy analysis for existing buildings to be conducted with greater granularity of input parameters relevant to thermal properties, which ultimately has potential for improving the reliability of BIM-based energy modeling and simulation.

By using the proposed method, the gbXML model does not need to be manually modified. Hence, it reduces energy modelers' time and efforts for model calibration. The proposed method has potential to be used for newly constructed building environments as well. In contrary to occupied buildings, these buildings are typically empty from furniture and other installments. As

an intensive quality assurance process during building commissioning, the proposed method can be used to check if the new building is operating as the owner initially intended without any faulty constructions such as improper installations. Second, when a building is initially commissioned, the proposed method can help estimate the thermal properties of unique building materials or customized construction types. Due to the unavailability or lack of knowledge about the thermal properties for such building materials or construction types, BIM elements do not always contain their thermal property information as a priori. In this case, the proposed method can help define the thermal properties of those BIM elements by mapping the as-is thermal property measurements to the relevant BIM elements.

While the experimental results show the perceived benefits of the applications, the following open research challenges still remain including: (1) Interoperability issues: Transferring BIM information into the current building energy performance analysis software still has a few limitations. To fully support the building information exchange for BIM-based energy analysis, BIM software should export BIM to the gbXML file, and the energy modeling and simulation tools should import from the gbXML file. However, few BIM software currently can export the building data in form of gbXML schema, and several building energy modeling and simulation software do not import from gbXML files (Sokolov and Crosby 2011). Thus, for those software, energy modelers need to manually check and modify the models (U.S. General Services Administration 2012); and (2) Limitations in the current gbXML schema: Current gbXML schema is incapable of representing non-planar surfaces (e.g., curved walls). The current gbXML schema supports only two types of building geometry: 3D planar polygon and 2D rectangular polygon. Thus, due to such limited representations and exporting functionalities related to building geometric data, the gbXML-based BIM may not always embody the as-built conditions. More research need to be conducted for investigating how to transfer the measured thermal properties of non-planar building elements (e.g., curved walls) into the associated BIM elements.

CHAPTER 10. CONCLUSIONS

10.1 Summary

To address the needs for energy diagnostics of existing buildings for improving energy efficiency and facilitating the associated retrofit decision-makings, this dissertation presented a new multi-modal visual sensing and analytics for building energy diagnostics and retrofit analyses using infrared thermography and BIM. Based on various validation metrics, these methods were validated on ten case studies from interior and exterior of existing residential and instructional buildings in IL and VA. This dissertation presented the following:

(1) A computer vision-based method for automated 3D spatio-thermal modeling of building environments without any space limitation using digital and thermal images captured by a consumer-level thermal camera: First, using an image-based 3D reconstruction pipeline which consists of Graphic Processing Unit (GPU)-based Structure-from-Motion (SfM) and Multi-View Stereo (MVS) algorithms, geometrical conditions of existing buildings are reconstructed in 3D. Next, 3D thermal point cloud models of the building environments are generated by using a new 3D thermal modeling pipeline. This pipeline involves a one-time thermal camera calibration, deriving the relative transformation by forming the Epipolar geometry between thermal and digital images, and the MVS algorithm for dense reconstruction. By automatically superimposing 3D building geometrical and thermal point clouds, 3D spatio-thermal models are formed, which allows practitioners to understand building thermal profiles at the level of point in 3D. The experimental results show that inexpensive digital and thermal images can be converted into ubiquitous reporters of the actual energy performance of existing buildings. The proposed method can be used as a great tool to effectively illustrate the as-is building condition to practitioners for building energy diagnostics.

(2) A method for automated analysis and visualization of deviations between buildings' actual and simulated thermal performances: The proposed method is based on Energy Performance Augmented Reality (EPAR) environments. In the EPAR modeling method, actual and expected 3D spatio-thermal models are generated and superimposed in a common 3D virtual environment. The method leverages unordered collections of thermal and digital images for actual thermal performance modeling, in addition to the numerical analysis for expected thermal performance simulation. Based on the EPAR models which store the as-is building condition and the

corresponding benchmark performance based on as-designed building information in form of 3D point cloud, 3D thermal mesh models are generated using *k-d* tree structures and nearest neighbor searching, which automates calculation of performance deviations to facilitate the identification of potential performance problems. The outcomes are visualized using a metaphor based on traffic light colors in EPAR models. Empirical observations show that automated analysis using EPAR models enables performance deviations to be measured and further used for inferring potential performance problems. In addition, the 3D visualization of performance deviations allows auditors to easily identify potential performance problems.

(3) A thermography-based method to quantify the as-is building conditions by exploring the as-is thermal resistances at the level of 3D point across geometrical forms of building assemblies and detecting condensation problems, and visualize the outcomes in an intuitive 3D form while taking into account building occlusions: First, digital and thermal images are collected from the building areas under inspection. Using a computer vision method – consisting of image-based 3D point cloud and mesh modeling algorithms – actual 3D spatio-thermal models are generated where surface temperature can be queried at the level of 3D point. Based on the resulting 3D spatio-thermal models and by measuring the reflected and dew point temperatures, the actual R-values of building assemblies are calculated at the level of 3D point, and the condensation issues are detected in building environments. Taking into account building occlusions, the distribution of the actual thermal resistance over each building assembly, the building areas associated with condensation problems, and the corresponding geometrical and thermal characteristics are jointly visualized in a 3D environment. The experimental results and the feedback received from the professionals show the promise of the proposed method in facilitating examination of building deteriorations and supporting the associated retrofit decision making.

(4) A model-based method for cost analysis of energy efficiency building envelope retrofits: This method builds on Energy Performance Augmented Reality (EPAR) modeling which generates and fuses actual and expected 3D spatio-thermal models. In the resulting EPAR models, the building areas associated with potential thermal degradations are first detected and calculated, and then the as-is thermal conditions of the associated building assemblies are also calculated at the level of point in 3D. Next, using the historical climatic data and the recommended R-values, the amount of the unnecessary heat transfer through the defective areas and the monetary benefits from retrofitting them (i.e., by improving the as-is thermal resistance of the defective areas to the

recommended level) are quantified. Finally, the expected energy cost savings are balanced against the cost of implementing insulation retrofit alternatives. Experimental results on three real-world buildings and four hypothetical cases with different weather conditions show the potential of the proposed method in reliably quantifying energy saving cost from retrofitting thermal performance problems, which improves the quality of current thermographic inspection relying on visual detection and qualitative interpretation of thermal irregularities.

(5) A method for automated mapping actual thermal property measurements at the level of 3D point to the associated BIM elements and updating their corresponding thermal properties in gbXML schema to improve the reliability of BIM-based energy modeling: By leveraging collections of digital and thermal images and based on environmental measurements, the proposed system first produces a 3D thermal model for the building under inspection and then derives the actual thermal resistances of the building assemblies at the level of 3D vertex in meshed BIM. By associating these measurements with their corresponding BIM elements in gbXML schema, thermal properties of the BIM elements are automatically updated by leveraging XML Document Object Model (DOM). Experimental results in real-world residential and instructional buildings show how actual thermal property measurement can be automatically associated with BIM elements and update the gbXML-based BIM. The proposed method shortens the gap between architectural information in BIM and the actual data needed for energy performance simulation, and thus enables reliable BIM-based energy analysis for retro–commissioning, continuous commissioning, and retrofit purposes. By using the as-is building condition (i.e., the updated gbXML-based BIM) as an input of energy simulation engines as opposed to using the notional value declared in the material specification or industry standard databases (i.e., as-designed BIM), practitioners can more accurately model the current energy performance of existing buildings. This has potential to improve the decision-making process for choosing the most appropriate retrofit alternatives.

Beyond the technical evaluation, for validating the practical significance of this research, the structured survey with domain experts with 2 to 10 years of practical experiences in energy auditing of existing buildings were conducted. As a result, several practical significances were documented. First, this research enables remote visual diagnostics. As a powerful communication tool to effectively illustrate the as-is building condition to practitioners, the proposed method enables energy auditors to virtually walk-through in buildings and explore the as-is conditions of

building geometry and the associated thermal conditions. This will increase auditors' inspection time in 3D virtual environments, as opposed to on-site inspection in real-world buildings. In addition, when diagnosing small-scale energy problems which are typically prevalent in real-world building environments, this research complements current building energy performance modeling and analysis software. The current tools typically require a single thermal property to be input for each building element. Because they assume that each building element has a constant surface-wide thermal property, they cannot model small-scale and non-uniform energy problems. This research address current inefficiencies by providing reasonable guidance for quantifying expected energy cost savings from retrofitting such small-scale energy problems. Lastly, by reflecting the as-is building conditions in the BIM-based building energy modeling process, this research decreases the gaps between the architectural information in the as-designed BIM and the as-is building conditions. This will complement current BIM-based energy analysis tools such as AUTODESK Green Building Studio by better characterizing the as-is building condition in the modeling process. In addition, in the case of historic building façades that are their thermal performance is typically non-uniform and use materials that are not available in today's standard material databases, this research defines the associated thermal property information as opposed to using substitutions in existing literatures. This further enables auditors to conduct more reliable energy analysis.

10.2 Open Gap-in-Knowledge

This dissertation presented several steps towards multi-modal visual sensing and analytics for building energy analyses for the purpose of improving energy efficiency. There are still several open research challenges and areas which need to be explored including:

(1) *Minimizing the impact of building occlusions on the reliability of thermographic inspection*: In order to accurately detect potential performance problems, any objects around building assemblies need to be removed prior to thermographic inspection. However, in practice, due to the space and time limitations, it may be impossible to remove all objects prior to inspection. One survey participant noted that "Accounting for furniture and other obstructions seems like a challenging task". The proposed method of setting a geometrical distance threshold has potential to ignore those building areas associated with static occlusions. Nonetheless, as discussed in Section 6, false negatives can still occur due to incomplete segmentations. In the experiments,

those happen around thin objects on walls such as frames (e.g., Figures 9.22 and 9.55 (e)) or tiny objects around windows (e.g., Figure 9.26 (b) and (c)). This is because the distance between thermal points associated with such objects in 3D point clouds and the nearest vertex in a geometrical baseline mesh is most likely to be within the geometrical distance threshold based on the registration error. As a result, the thermal resistance of the occluded building assemblies was not accurately calculated. More research needs to be conducted to better segment non-relevant objects from 3D reconstructed scenes.

(2) *Automated extraction of building geometry from 3D reconstructed scenes for energy simulation*: To acquire geometrical boundary conditions for energy simulation, the proposed method involves manual extraction of boundary points from 3D geometrical point clouds. The proposed method can facilitate the data collection process including manual surveying of building environments in the current practices. Also, this requires less manual tasks compared to existing photogrammetry software such as Autodesk ImageModeler (ImageModeler 2012) that involves several supervised processes for selecting corresponding points between image pairs for image stitching as well as boundary points of building environments in the stitched images. Toward fully automated process for converting 2D images into the geometrical boundary condition for energy simulation, additional research needs to be conducted on automated extraction of boundary elements (i.e., points and lines) from 3D reconstructed scenes.

(3) *Heat transfer by air infiltration and exfiltration through cracks*: The proposed method mainly considers thermal degradations that exist in building assemblies adjacent to the exterior. In addition to degradation of building materials and the resulting declining thermal resistances, the air leaks due to cracks can also cause energy loss through air exfiltration and infiltration in hot and cold seasons. The amount of heat transfer associated with air infiltration and exfiltration can be calculated using Equation (23) and the following values proposed in (Ham and Golparvar-Fard 2013): 1) the heat capacity of air (1205.8 J/m^3) that is derived from multiplying the density of air (1.2 Kg/m^3) by its specific heat (1004.83 J/Kg); 2) the volume of the closed space under inspection (V); 3) the number of 'air change per hour' (ACH) caused by air leaks; and 4) 'degree days' statistics ($\Delta T \times t$).

$$Q_{AirLeak} = 1205.8 \times V \times ACH \times \Delta T \times t \quad (23)$$

For calculating $Q_{AirLeak}$ using Equation (23), the main challenge is to determine ACH which is subject to the air tightness of the as-is construction. This value can be estimated by using a blower door test. Thermographic inspection is commonly used with a blower door test. For a blower door test, auditors first install fans in the exterior door. Then, by lowering the inside air pressure using the fan, the outside air with higher pressure flows in through building cracks. Lastly, the auditors detect air leaks by using a smoke pencil. Because the blower door test typically exaggerate air leaks, infrared imaging with a blower door test is a powerful tool for determining air leaks. Such integrated experiments need to be conducted for more comprehensive calculation of unnecessary heat transfer through building envelopes.

(4) *Improving the 3D thermal modeling of building environments*: The proposed image-based 3D thermal modeling method generate 3D thermal profiles of confined and complex indoor environments by using a thermal camera with a built-in digital camera. Here, 3D point cloud models would have some parts that remain incomplete for featureless areas such as drywall or plastered surfaces. Hence, it is not trivial to select the point pairs between two models for performance comparison. Although 3D thermal mesh modeling is introduced to overcome such challenges in this research, there is another significant potential to improve 3D thermal modeling by leveraging additional visual sensors. In the past few years, new imaging systems such as the Microsoft Kinect or the Asus Xtion sensor that provide both color and depth images have become readily available. There are great expectations among both researchers and practitioners that such systems will lead to a boost of new applications in the field of 3D reality capture in structured and unstructured environments. Beyond providing geometrical information through depth images, these systems also have potential to produce point cloud models that are needed for 3D spatio-thermal modeling. Through joint calibration with a thermal camera, they also enable mapping of surface temperature distribution into the resulting point cloud models.

(5) *Generating 4D thermal profile (3D + time) at the level of building*: The proposed method is capable of generating 3D spatio-thermal models by using thermal images taken in a rather short period of time. Modeling and visualizing the time-series of dynamic energy performance metrics provide a better understanding of time-varying heat transfer conditions. Integrating several 3D thermal models from different time periods also will provide an opportunity to understand the impact of building energy efficiency retrofit actions. For example, energy auditors can conduct a before/after analysis on thermal resistances when additional insulation

layers are being installed. Such analyses would support implementation of periodic building maintenance programs. In addition, more research needs to be done to investigate how separated 3D thermal models – each representing a separate space in a building – can be integrated to understand the as-is energy performance at building scale.

REFERENCES

Aelenei, D., and Henriques, F. M. A. (2008). "Analysis of the condensation risk on exterior surface of building envelopes." *Energy and Buildings*, 40(10), 1866-1871.

Ahmad, M., and Culp, C. H. (2006). "Uncalibrated Building Energy Simulation Modeling Results." *HVAC&R Research*, 12(4), 1141-1155.

AIA (2012). "Energy modeling." <http://wiki.aia.org/wiki%20pages/energy%20modeling.aspx>. (Jan 28, 2012).

Aksenov, A. G., Milgrom, M., and Usov, V. V. (2003). "Radiation from hot, bare, strange stars." *Monthly Notices of the Royal Astronomical Society*, 343(3), L69-L72.

Albatici, R., and Tonelli, A. M. (2010). "Infrared thermovision technique for the assessment of thermal transmittance value of opaque building elements on site." *Energy and Buildings*, 42(11), 2177-2183.

Architecture2030 (2011). "Problem: The Building Sector." <http://www.architecture 2030.org/>. (Nov 23, 2011).

Asfour, O. S., and Gadi, M. B. (2007). "A comparison between CFD and Network models for predicting wind-driven ventilation in buildings." *Building and Environment*, 42(12), 4079-4085.

Autodesk (2011). "Streamlining Energy Analysis of Existing Buildings with Rapid Energy Modeling." *2011 Autodesk White Paper*, Autodesk.

Azar, E., and Menassa, C. (2012). "Agent-Based Modeling of Occupants and Their Impact on Energy Use in Commercial Buildings." *Journal of Computing in Civil Engineering*, 26(4), 506-518.

Balaras, C. A., and Argiriou, A. A. (2002). "Infrared thermography for building diagnostics." *Energy and Buildings*, 34(2), 171-183.

Barker, E., Maldague, X., and Laurendeau, D. (1995). "Shape reconstruction from a single thermal image." *Optical Engineering* 34(1), 154-159.

Bellia, L., and Minichiello, F. (2003). "A simple evaluator of building envelope moisture condensation according to an European Standard." *Building and Environment*, 38(3), 457-468.

Borrmann, D., Elseberg, J., and Nüchter, A. (2013). "Thermal 3D Mapping of Building Façades." *Intelligent Autonomous Systems 12*, S. Lee, H. Cho, K.-J. Yoon, and J. Lee, eds., Springer Berlin Heidelberg, 173-182.

Bouguet, J.-Y. (2010). "Camera Clibration Toolbox." <http://www.vision.caltech.edu/bouguetj/calib_doc/>. (Feb 2, 2012).

Bynum, R. T. (2000). *Insulation Handbook*, McGraw-Hill.

California Energy Commission (2012). "Comprehensive Energy Efficiency Program For Existing Buildings Scoping Report." California Energy Commission

Carrilho da Graça, G., Martins, N. R., and Horta, C. S. "Thermal and airflow simulation of a naturally ventilated shopping mall." *Energy and Buildings*, 50, 177 - 188.

Cerdeira, F., Vázquez, M. E., Collazo, J., and Granada, E. (2011). "Applicability of infrared thermography to the study of the behaviour of stone panels as building envelopes." *Energy and Buildings*, 43(8), 1845-1851.

Chen, Q. (1995). "COMPARISON OF DIFFERENT k-ε MODELS FOR INDOOR AIR FLOW COMPUTATIONS." *Numerical Heat Transfer, Part B: Fundamentals*, 28(3), 353-369.

Chidiac, S. E., Catania, E. J. C., Morofsky, E., and Foo, S. (2011). "A screening methodology for implementing cost effective energy retrofit measures in Canadian office buildings." *Energy and Buildings*, 43(2–3), 614-620.

Cho, Y. K., Ham, Y., and Golparvar-Fard, M. (2015). "3D As-is Building Energy Modeling and Diagnostics: A Review of the State-of-the-Art." *Advanced Engineering Informatics*, 29(2), 184-195.

ColoradoENERGY (2013). "R-Value Table: Insulation Values For Selected Materials." <http://www.coloradoenergy.org/procorner/stuff/r-values.htm>.

Dall'O', G., Sarto, L., and Panza, A. (2013). "Infrared Screening of Residential Buildings for Energy Audit Purposes: Results of a Field Test." *Energies*, 6(8), 3859-3878.

de Berg, M., Cheong, O., van Kreveld, M., and Overmars, M. (2008). *Computational Geometry: Algorithms and Applications*, Springer.

Desogus, G., Mura, S., and Ricciu, R. (2011). "Comparing different approaches to in situ measurement of building components thermal resistance." *Energy and Buildings*, 43(10), 2613-2620.

Eads, L. G. (2000). "Thermography." *ASHRAE journal*, 42(3), 51.

EIA (2010). "Annual Energy Review 2010." U.S. Energy Information Administration.

ENERGY STAR (2013). "Recommended Levels of Insulation." <http://www.energystar.gov/?c=home_sealing.hm_improvement_insulation_table>.

Entrop, A. G., Brouwers, H. J. H., and Reinders, A. H. M. E. (2010). "Evaluation of energy performance indicators and financial aspects of energy saving techniques in residential real estate." *Energy and Buildings*, 42(5), 618-629.

Essess. Inc (2014). "essess." <http://www.essess.com/>.

European Standard (EN) (1997). "Glass in building - determination of thermal transmittance (U-value) - calculation method." *EN 673*.

Evola, G., and Popov, V. (2006). "Computational analysis of wind driven natural ventilation in buildings." *Energy and Buildings*, 38(5), 491-501.

Fan, Y., and Ito, K. (2012). "Energy consumption analysis intended for real office space with energy recovery ventilator by integrating BES and CFD approaches." *Building and Environment*, 52(0), 57-67.

Fischler, M., and Bolles, R. (1981). "Random Sample Consensus." *Communications of the ACM*, 24(6).

FLIR system (2010). "Thermographhic measurement techniques." *FLIR Reporter Professional, Professional Edition*, 133-137.

FLIR system (2012). "Thermal Imaging Guidebook for Building and Renewable Energy Applications."

Fokaides, P. A., and Kalogirou, S. A. (2011). "Application of infrared thermography for the determination of the overall heat transfer coefficient (U-Value) in building envelopes." *Applied Energy*, 88(12), 4358-4365.

Fox, M., Coley, D., Goodhew, S., and de Wilde, P. (2014). "Thermography methodologies for detecting energy related building defects." *Renewable and Sustainable Energy Reviews*, 40(0), 296-310.

Furukawa, Y., and Ponce, J. (2008). "Accurate, Dense, and Robust Multiview Stereopsis." *Pattern Analysis and Machine Intelligence, IEEE Transactions on*, 32(8), 1362-1376.

gbXML (2013). "Open Green Building XML Schema: a Building Information Modeling Solution for Our Green World." <http://www.gbxml.org/aboutgbxml.php>.

Golparvar-Fard, M., Bohn, J., Teizer, J., Savarese, S., and Peña-Mora, F. (2011). "Evaluation of image-based modeling and laser scanning accuracy for emerging automated performance monitoring techniques." *Automation in Construction*, 20(8), 1143-1155.

Golparvar-Fard, M., and Ham, Y. (2014). "Automated Diagnostics and Visualization of Potential Energy Performance Problems in Existing Buildings Using Energy Performance Augmented Reality Models." *Journal of Computing in Civil Engineering*, 28(1), 17-29.

González-Aguilera, D., Lagüela, S., Rodríguez-Gonzálvez, P., and Hernández-López, D. (2013). "Image-based thermographic modeling for assessing energy efficiency of buildings façades." *Energy and Buildings*, 65(0), 29-36.

Gonzalez-Aguilera, D., Rodriguez-Gonzalvez, P., and Gomez-Lahoz, J. (2010). "Camera and Laser Robust Integration in Engineering and Architecture Applications." *Sensor Fusion and its Applications*, C. Thomas, ed., Sciyo, August, 2010.

Gould, K., and Hosey, L. (2006). "Ecology & Design: Ecological Literacy in Architecture Education ", American Institute of Architects (AIA).

Ham, Y., and Golparvar-Fard, M. "Identification of Potential Areas for Building Retrofit using Thermal and Digital Imagery, plus CFD Models." *Proc., International Workshop on Computing in Civil Engineering*, ASCE, 642-649.

Ham, Y., and Golparvar-Fard, M. "Rapid 3D Energy Performance Modeling of Existing Buildings using Thermal and Digital Imagery." *Proc., 2012 Construction Research Congress*, 991-1000.

Ham, Y., and Golparvar-Fard, M. "Automated Cost Analysis of Energy Loss in Existing Buildings through Thermographic Inspections and CFD Analysis." *Proc., The 30th International Symposium on Automation and Robotics in Construction (ISARC) 2013*.

Ham, Y., and Golparvar-Fard, M. (2013). "An automated vision-based method for rapid 3D energy performance modeling of existing buildings using thermal and digital imagery." *Advanced Engineering Informatics*, 27(3), 395-409.

Ham, Y., and Golparvar-Fard, M. "Calculating the Cost of Heating and Cooling Loss for Building Diagnostics Using EPAR (Energy Performance Augmented Reality Models)." *Proc., Computing in Civil Engineering (2013)*, 242-249.

Ham, Y., and Golparvar-Fard, M. (2013). "EPAR: Energy Performance Augmented Reality models for identification of building energy performance deviations between actual measurements and simulation results." *Energy and Buildings*, 63(0), 15-28.

Ham, Y., and Golparvar-Fard, M. (2014). "3D Visualization of Thermal Resistance and Condensation Problems in Infrared Thermography for Building Energy Diagnostics." *Visualization in Engineering*, 2(1), 1-15.

Ham, Y., and Golparvar-Fard, M. "Evaluating the Value of Investment in Building Insulation Retrofits Based on EPAR (Energy Performance Augmented Reality) Models." *Proc., Construction Research Congress 2014*, 2234-2243.

Ham, Y., and Golparvar-Fard, M. (2015). "Three-Dimensional Thermography-Based Method for Cost-Benefit Analysis of Energy Efficiency Building Envelope Retrofits." *Journal of Computing in Civil Engineering*, 29(4), B4014009.

Ham, Y., and Golparvar-Fard, M. "Updating R-Values of BIM Elements using 3D Thermography for Accurate Building Energy Performance Simulation." *Proc., Computing in Civil and Building Engineering (2014)*, 113-120.

Ham, Y., and Golparvar-Fard, M. (2015). "Mapping actual thermal properties to building elements in gbXML-based BIM for reliable building energy performance modeling." *Automation in Construction*, 49, Part B(0), 214-224.

Hartley, R., and Zisserman, A. (2004). *Multiple view geometry*, Cambridge University Press.

Heo, Y., Choudhary, R., and Augenbroe, G. A. (2012). "Calibration of building energy models for retrofit analysis under uncertainty." *Energy and Buildings*, 47(0), 550-560.

Hoff, R. (2011). "Water condensation – a temperature related phenomenon." <http://www.moistureview.com/blog-034>.

HomeInspex (2011). "Thermal Imaging to Identify Air Leaks, Sample Report." HomeInspex.

Horn, B. (1987). "Closed-form Solution of Absolute Orientation using Unit Quaternions." *Journal of the Optical Society*, 4(4), 629-642.

ImageModeler (2012). "Create Photorealistic 3D Objects from Photographs." <http://usa.autodesk.com/adsk/servlet/pc/index?id=11390028&siteID=123112>. (Oct 2, 2012).

InfraredConceptsCorporation (2012). "Thermal Mapping & Surveying." <http://www.infrared2k.com/>. (Jan 31, 2012).

ISO 6946 "Building components and building elements-Thermal resistance and thermal transmittance-Calculation method."

ISO 9869 "Thermal insulation - Building elements - In-situ measurement of thermal resistance and thermal transmittance."

Juan, Y.-K., Gao, P., and Wang, J. (2010). "A hybrid decision support system for sustainable office building renovation and energy performance improvement." *Energy and Buildings*, 42(3), 290-297.

Kiziltas, S., Akinci, B., Ergen, E., and Tang, P. (2008). "Technological assessment and process implications of field data capture technologies for construction and facility/infrastructure management." *ITcon*, 13(Special Issue Sensors in Construction and Infrastructure Management), 134-154.

Kunz, J., Maile, T., and Bazjanac, V. (2009). "Summary of the energy analysis of the first year of the Stanford Jerry Yang & Akiko Yamazaki Environment & Energy (Y2E2) Building."Stanford, CA: Center for Integrated Facility Engineering, Stanford University.

Kylili, A., Fokaides, P. A., Christou, P., and Kalogirou, S. A. (2014). "Infrared thermography (IRT) applications for building diagnostics: A review." *Applied Energy*, 134(0), 531-549.

Lagüela, S., Armesto, J., Arias, P., and Herráez, J. (2012). "Automation of thermographic 3D modelling through image fusion and image matching techniques." *Automation in Construction*, 27(0), 24-31.

Lagüela, S., Díaz-Vilariño, L., Armesto, J., and Arias, P. (2014). "Non-destructive approach for the generation and thermal characterization of an as-built BIM." *Construction and Building Materials*, 51(0), 55-61.

Lagüela, S., Díaz-Vilariño, L., Martínez, J., and Armesto, J. (2013). "Automatic thermographic and RGB texture of as-built BIM for energy rehabilitation purposes." *Automation in Construction*, 31(0), 230-240.

Lagüela, S., Martínez, J., Armesto, J., and Arias, P. (2011). "Energy efficiency studies through 3D laser scanning and thermographic technologies." *Energy and Buildings*, 43(6), 1216-1221.

Lakaemper, R., and Malkawi, A. M. (2009). "Integrating Robot Mapping and Augmented Building Simulation." *Journal of Computing in Civil Engineering*, 23(6), 384-390.

Li, Q., Yoshino, H., Mochida, A., Lei, B., Meng, Q., Zhao, L., and Lun, Y. (2009). "CFD study of the thermal environment in an air-conditioned train station building." *Building and Environment*, 44(7), 1452-1465.

Lowe, D. (2004). "Distinctive image features from scale-invariant keypoints." *International Journal of Computer Vision*, 60(2), 91-110.

Madding, R. "Finding R-Values of Stud Frame Constructed Houses with IR Thermography." *Proc., InfraMation 2008*, 261-277.

Maile, T. (2010). "Comparing measured and simulated building energy performance data." PhD dissertation, Stanford University.

Malkawi, A. M., and Srinivasan, R. S. (2005). "A new paradigm for Human-Building Interaction: the use of CFD and Augmented Reality." *Automation in Construction*, 14(1), 71-84.

Martin, K., Campos-Celador, A., Escudero, C., Gómez, I., and Sala, J. M. (2012). "Analysis of a thermal bridge in a guarded hot box testing facility." *Energy and Buildings*, 50(0), 139-149.

Martín Ocaña, S., Cañas Guerrero, I., and González Requena, I. (2004). "Thermographic survey of two rural buildings in Spain." *Energy and Buildings*, 36(6), 515-523.

Mass Saves (2013). "Home Energy Assessment." <http://www.masssave.com/residential/home-energy-assessments>.

Menassa, C. C. (2011). "Evaluating sustainable retrofits in existing buildings under uncertainty." *Energy and Buildings*, 43(12), 3576-3583.

Mikron Instrument Company (2012). "Table of Emissivity of Various Surface."

Molin, A., Rohdin, P., and Moshfegh, B. (2011). "Investigation of energy performance of newly built low-energy buildings in Sweden." *Energy and Buildings*, 43(10), 2822-2831.

NIST (2010). "Measurement Science Roadmap for Net-Zero Energy Buildings." National Institute of Standards and Technology (NIST) Technical Note 1660.

Nister, D. (2004). "An efficient solution to the five-point relative pose problem." *Pattern Analysis and Machine Intelligence, IEEE Transactions on*, 26(6), 756-770.

Papadopoulos, A. M., Theodosiou, T. G., and Karatzas, K. D. (2002). "Feasibility of energy saving renovation measures in urban buildings: The impact of energy prices and the acceptable pay back time criterion." *Energy and Buildings*, 34(5), 455-466.

Pelagottia, A., Del Mastio, A., Uccheddu, F., and Remondino, F. "Automated multispectral texture mapping of 3D models." *Proc., 17th European Signal Processing Conference (EUSIPCO 2009)*.

Pelletier, J.-F., and Maldague, X. (1997). "Shape from heating: a two-dimensional approach for shape extraction in infrared images " *Optical Engineering*, 36(2).

PhotoModeler (2012). "PhotoModeler Scanner." <http://www.photomodeler.com/products/pm-scanner.htm>.

Poel, B., van Cruchten, G., and Balaras, C. A. (2007). "Energy performance assessment of existing dwellings." *Energy and Buildings*, 39(4), 393-403.

Prakash, S., Lee, P., and Robles-Kelly, A. (2007). "Stereo techniques for 3D mapping of object surface temperatures." *The Quantitative InfraRed Thermography (QIRT) Journal*, 4(1), 63-84.

Reddy, A. (2006). "Literature review on calibration of building energy simulation programs: uses, problems, procedures, uncertainty, and tools." *Enviornmental Engineering*, 112(1), 226-240.

Rohdin, P., and Moshfegh, B. (2007). "Numerical predictions of indoor climate in large industrial premises. A comparison between different k–ε models supported by field measurements." *Building and Environment*, 42(11), 3872-3882.

Singham, J. R. (1962). "Tables of emissivity of surfaces." *International Journal of Heat and Mass Transfer*, 5(1–2), 67-76.

Snavely, N., Seitz, S., and Szeliski, R. (2008). "Modeling the World from Internet Photo Collections." *International Journal of Computer Vision*, 80(2), 189-210.

Sokolov, I., and Crosby, J. (2011). "Utilizing gbXML with AECOsim Building Designer and speedikon."Bentley.

Somarathne, S., Seymour, M., and Kolokotroni, M. (2005). "Dynamic thermal CFD simulation of a typical office by efficient transient solution methods." *Building and Environment*, 40(7), 887-896.

Spengler, J. D., and Chen, Q. (2000). "INDOOR AIR QUALITY FACTORS IN DESIGNING A HEALTHY BUILDING." *Annual Review of Energy and the Environment*, 25(1), 567-600.

Stockton, G. "Using thermal mapping at the data center." *Proc., InfraMation 2010 Proceedings*.

The Engineering Toolbox (2013). "Heat Loss through Building Elements due to Transmission." <http://www.engineeringtoolbox.com/heat-loss-transmission-d_748.html>.

The National Oceanic and Atmospheric Administration (NOAA) (2013). "Heating & Cooling Degree Day Data." <http://www.ncdc.noaa.gov/oa/documentlibrary/hcs/hcs.html>.

TheGeoInformationGroup. (2007). "Cities Revealed's thermal mapping." <http:// www.geoinformationgroup.co.uk/products/thermal-mapping>. (Dec 31, 2011).

Trčka, M., and Hensen, J. L. M. (2010). "Overview of HVAC system simulation." *Automation in Construction*, 19(2), 93-99.

Triggs, B., McLauchlan, P., Hartley, R., and Fitzgibbon, A. "Bundle adjustment -- a modern synthesis." *Proc., International Workshop on Vision Algorithms*, 153-177.

Tupper, K. (2011). "Collaborate and Capitalize: Post-Report from the BEM Innovation Summit." Rocky Mountain Institute.

Tupper, K., Franconi, E., Chan, C., Hodgin, S., Buys, A., and Jenkins, M. "Building Energy Modeling: Industry-Wide Issues And Potential Solutions." *Proc., 12th Conference of International Building Performance Simulation Association*.

Turner, C., and Frankel, M. (2008). "Energy Performance of LEED for New Construction Buildings." New Buildings Institute, Vancouver, WA.

Turner Construction (2008). "Credit Market Condition Not Likely to Affect Plans to Build Green Buildings." <http://www.prnewswire.com/news-releases/credit-market-condition-not-likely-to-affect-plans-to-build-green-buildings-say-75-of-commercial-real-estate-executives-surveyed-by-turner-construction-company-65466157.html>.

U.S. DOE (2010). "2010 U.S. DOE buildings energy databook." U.S. Department of Energy.

U.S. DOE (2012). "Insulation." <http://energy.gov/energysaver/articles/insulation>.

U.S. DOE (2012). "Thermographic Inspection." <http://www.energysavers.gov/your_home/energy_audits/index.cfm/mytopic=11200>. (Feb 3, 2012).

U.S. DOE (2012). "Types of Insulation." <http://energy.gov/energysaver/articles/types-insulation>.

U.S. Energy Information Administration (2013). "Average Retail Price of Electricity to Ultimate Customers by End-Use Sector." <http://www.eia.gov/electricity/data.cfm#sales>.

U.S. Energy Information Administration (2013). "Natural Gas Prices." <http://www.eia.gov/dnav/ng/ng_pri_sum_a_epg0_prs_dmcf_m.htm>.

U.S. General Services Administration (2012). "GSA BIM Guide for Energy Performance."

van Hooff, T., Blocken, B., Aanen, L., and Bronsema, B. (2011). "A venturi-shaped roof for wind-induced natural ventilation of buildings: Wind tunnel and CFD evaluation of different design configurations." *Building and Environment*, 46(9), 1797-1807.

Vera, S., Fazio, P., and Rao, J. (2010). "Interzonal air and moisture transport through large horizontal openings in a full-scale two-story test-hut: Part 2 – CFD study." *Building and Environment*, 45(3), 622-631.

W3C (2013). "W3C Document Object Model (DOM)." <http://www.w3.org/TR/dom/>.

Walker, C., Tan, G., and Glicksman, L. (2011). "Reduced-scale building model and numerical investigations to buoyancy-driven natural ventilation." *Energy and Buildings*, 43(9), 2404-2413.

Wang, C., Cho, Y., and Gai, M. (2013). "As-Is 3D Thermal Modeling for Existing Building Envelopes Using a Hybrid LIDAR System." *Journal of Computing in Civil Engineering*, 27(6), 645-656.

Wanielista, M., Kersten, R., and Ron;, E. (1997). *Hydrology Water Quantity and Quality Control*, John Wiley & Sons.

Wu, C. (2007). "SiftGPU: A GPU implementation of Scale Invaraint Feature Transform (SIFT)." <http://cs.unc.edu/~ccwu/siftgpu>.

Wu, C., Agarwal, S., Curless, B., and Seitz, S. M. "Multicore bundle adjustment." *Proc., Computer Vision and Pattern Recognition (CVPR), 2011 IEEE Conference on*, 3057-3064.

Yakhot, V., and Orszag, S. A. (1986). "Renormalization group analysis of turbulence. I. Basic theory." *Journal of Scientific Computing*, 1(1), 3-51.

Yudelson, J. (2010). *Greening Existing Buildings (McGraw-Hill's Greensource)*, McGraw-Hill, New York, NY.

Zhai, Z., and Chen, Q. (2003). "Solution characters of iterative coupling between energy simulation and CFD programs." *Energy and Buildings*, 35(5), 493-505.

Zhai, Z., Chen, Q., Haves, P., and Klems, J. H. (2002). "On approaches to couple energy simulation and computational fluid dynamics programs." *Building and Environment*, 37(8–9), 857-864.

Zhai, Z. J., and Chen, Q. Y. (2005). "Performance of coupled building energy and CFD simulations." *Energy and Buildings*, 37(4), 333-344.